UNIVERSITÀ DEGLI STUDI DI MILANO

Scuola di Dottorato in Fisica, Astrofisica e Fisica Applicata
Dipartimento di Fisica

Corso di Dottorato in Fisica, Astrofisica e Fisica Applicata
Ciclo XXX

Electron positron pair flow and current composition in the pulsar magnetosphere: steps toward self-consistency

Settore Scientifico Disciplinare FIS/05

Supervisore: Professor Pierre M. PIZZOCHERO

Supervisore Esterno: Dottor Alice K. HARDING

Tesi di Dottorato di:
Gabriele BRAMBILLA

Anno Accademico 2017/2018

Commission of the final examination:

External Member:
Prof. Roberto Turolla - Universià degli Studi di Padova

External Member:
Dr. Benoît Cerutti - Université Grenoble Alpes

External Member:
Prof. David Smith - Université de Bordeaux

Final examination:

Date 23rd January 2018

Università degli Studi di Milano, Dipartimento di Fisica, Milano, Italy

The same thrill, the same awe and mystery, come again and again
when we look at any problem deeply enough.
With more knowledge comes deeper, more wonderful mystery.

Richard P. Feynmann, "The Value of Science,"
in Frontiers in Science: A Survey, ed. Edward Hutchings Jr.
(New York: Basic Books, 1958), 262-63

I dedicate this thesis to all the friends that I met in the US.

As I told to many of you, I am sure that we will find each other again.

MIUR subjects:

FIS/05

PACS:

97.60.Gb, 95.30.Qd, 52.65.Rr

Contents

List of Figures **vii**

List of Tables **xv**

Introduction **xv**

1 Pulsar Science Background **1**
- 1.1 Neutron stars basics 1
- 1.2 High Energy Emission Processes and Relativistic Effects 14

2 The pulsar magnetosphere problem: Theory **21**
- 2.1 Introduction 21
- 2.2 The Deutsch solution 21
- 2.3 The force-free magnetosphere 25
- 2.4 Plasma supply and pair production 28
- 2.5 Estimating the conditions of the plasma in the pulsar magnetosphere 32

3 A PIC code for the pulsar magnetosphere **37**
- 3.1 Introduction and PIC code basics 37
- 3.2 A PIC code for the pulsar magnetosphere 49

4 PIC simulations of the pulsar magnetosphere **63**
- 4.1 Force-free simulations for comparison 63
- 4.2 Magnetospheres with particles supplied everywhere 63
- 4.3 Magnetosphere with particles supplied only at the surface 71
- 4.4 Discussion 88

Conclusions and outlooks **91**

Bibliography **93**

List of Publications **99**

List of Figures

1.1 $P-\dot{P}$ diagram for rotation-powered pulsars, Isolated Neutron Stars (INS), Compact Central Objects (CCO), Rotating Radio Transients (RRATs) and magnetars. Lines of constant characteristic age, τ, and spin-down luminosity, $\dot{E}$, are superposed. Picture taken from Harding (2013). 2

1.2 On the left, a sketch of the hollow cone geometry, on the right the averaged wave forms that would be viewed by four observers with different inclinations from the rotation axis. Figure taken by Backer (1976). 3

1.3 In this figure are shown some very good RVM data and the model used to fit them (Everett & Weisberg 2001). 4

1.4 This Chandra image (in the X-band) shows clearly the SNR, the PWN and the pulsar jet of PSR J1104-6103, also called the lighthouse nebula. This picture has been published like Astronomy Picture Of the Day `http://apod.nasa.gov/apod/archivepix.html` (Accessed: 08/10/2017) on 21/02/2014. The same image (without labels) is available on `http://chandra.harvard.edu/` (Accessed: 08/10/2017). 5

1.5 In this figure are shown the SNR and the Central Compact Object (CCO, the white point source) of Cassiopea A imaged by Chandra. The color are coded with respect to the photon energies: Red $0.5 \div 1.5$ keV, Green $1.5 \div 2.5$ keV and Blue $4.0 \div 6.0$ keV. The picture is taken from `http://chandra.harvard.edu/` (Accessed: 08/10/2017). 6

1.6 In this figure are shown two examples of bowshocks, and two artist impressions that helps in interpreting the image. Here the original capiton: *Images captured by NASA's Chandra X-ray Observatory (top) with artist representations (below) that provided a better look at pulsars and their associated wind nebulae. Geminga, left, is approximately 800 light years from earth. Geminga's tail can stretch more than half a light year longer than 1,000 times the distance between the Sun and Pluto. BO355+54, right, is approximately 3,300 light years from Earth. The narrow, double tail extends almost five light years away from the star. Top Left X-ray: NASA/CXC/PSU/B.Posselt et al; Infrared (BACKGROUND): NASA/JPL-Caltech Top Right X-ray: NASA/CXC/GWU/N.Klinger et al; Infrared (BACKGROUND): NASA/JPL-Caltech Bottom illustrations by Nahks Tr'Ehnl.* Picture taken from `http://news.psu.edu/` (Accessed: 20/10/2017). 7

1.7 In this figure are shown three different examples of PWNe pictured by Chandra in the X-rays: on the left there is a pulsar with a clear toroidal shape (J0205+6449), the central one present a clear bowshock-tail (the Mouse nebula, J1747-2958) and on the right there is one intermediate case (the Vela nebula, J0835-4510). Pictures taken from Kargaltsev & Pavlov (2008). 7

1.8 This picture shows an X-image of the Crab nebula. The distinguishable parts are the point like object inside the nebula, the two jets departing from it and the wind termination shock where the torus starts inside the nebula. This picture is taken from `http://chandra.harvard.edu/` (Accessed: 08/10/2017). 8

1.9 *Fermi* five-year map of the sky showing the positions of the 117 pulsars listed in the 2PC. Image from NASA/DOE/Fermi LAT Collaboration `http://svs.gsfc.nasa.gov/` (Accessed: 08/10/2017). 11

1.10 $P - \dot{P}$ distribution of the 117 *Fermi* pulsars (radio-loud pulsars shown as green circles, radio-quiet as blue squares, and MSPs as red triangles) plotted together with the entire radio pulsar sample known today (black dots, 710 in all, represent timed pulsars that were phase folded, but not detected, whereas 1337 gray dots represent pulsars without timing solution). Lines of constant rotational energy loss $\dot{E}$, characteristic age τ, and surface B field B_s are also shown. Recently discovered MSPs, for which no $\dot{P}$ has been measured, are plotted at $\dot{P} = 5 \cdot 10^{22}$. All the *Fermi* LAT pulsars lie above $\dot{E} = 10^{33} erg\ s^{-1}$. This picture is taken from the 2PC (Abdo et al. 2013a). 12

1.11 These pictures are taken from 2PC Abdo et al. (2013a), from the top to the bottom and from left to right there are shown: J1907+0602 (example of bridge emission), J1813-1246 (example of off-peak emission), J0633+0632 (no bridge, no off-peak emission), J1509-5850, J1741-2054, J0357+3205. The black line is the the γ-ray light curve, the red line is the radio light curve, the horizontal lines are the noise levels (the emission is surely present only when it is higher than the noise levels). On the y axis there are the photon weighted counts (weighted in the sense that they are selected in a maximum likelihood process that use weights), on the x axis there is the phase where 1.0 is a period. 13

1.12 Normalized spectra of CR $(1/I)(dI/dy) = (9\sqrt{3}/8\pi)y \int_y^\infty K_{\frac{5}{3}}(x)\,\mathrm{d}x$, where $y = \omega/\omega_c$ and $I = 4\pi e^2\gamma^4/3\rho$. *(a)* y axis with a linear scale, *(b)* y axis with a logarithmic scale. Picture taken from Jackson (1998a). 16

1.13 This picture show the time of flight for different particles on the field lines. The yellow line is $\mathbf{r_A} \cdot \mathbf{v_A}/(v_A \cdot R_{LC})$ where $\mathbf{r_A}$ is the particle position vector and $\mathbf{v_A}$ is the velocity position vector. 19

2.1 In this Figure there are shown the open and closed magnetic field lines for the Deutsch solution of a 45° inclined rotator. The axes are in $R_{\rm LC}$ units. This picture has been obtained using the software VisIt (Childs et al. 2012). 22

2.2 This figure shows the structure of a magnetic dipole on two different scales. The dipole is 90° inclined with respect to the rotational axis. The open magnetic field lines outside the LC are swept back and become parallel wavefronts. The circle indicates the LC. This picture is taken from Yadigaroglu (1997). 23

2.3 In this Figure there are shown the open and closed magnetic field lines for the force-free magnetosphere of a $45°$ inclined rotator. The axes are in R_{LC} units. This picture has been obtained using the software VisIt (Childs et al. 2012). 29

2.4 This figure shows the magnetic field lines of the first force-free solutions of the pulsar magnetosphere. a) is from Spitkovsky (2006), and it is for a $60°$ inclined rotator. The color scale represents the in plane component of the magnetic field. b) is the aligned rotator solution from Contopoulos et al. (1999). The dashed-dotted lines on the outer edge represent the asymptotic solution, the region between the dashed line and the thick line represents the current region that flows in the opposite direction of the one flowing from the polar cap. The dotted line is the null line, where the charge density changes sign. 30

2.5 Electrosphere solution from Krause-Polstorff & Michel (1985). The dashed lines are the magnetic field lines, the solid lines are equipotential lines, the dots are the particles. 31

3.1 The scheme of a PIC code. The figure is taken from Birdsall & Langdon (1991). 38

3.2 First orders of the particle shape function. Figure taken from Birdsall & Langdon (1991). 39

3.3 At long distances particles do not overlap, at short distances part of their charge could be neutralized if the other particle has opposite sign. Figure taken from Lapenta (checked on: 2017-03-03). 41

3.4 In this figure the force between two macro particles (F - y axes) is plot against their distance (r - x axis). The three curves represent a point particle, a particle with radius a of a half the Debye length (λ_D) and another with a radius of one λ_D. As you can see the force changes at small distances, but it does not at larger distances. All the lengths are expressed in λ_D units. Figure taken from Lapenta (checked on: 2017-03-03). 41

3.5 Time centering of $\mathbf{F}$, $\mathbf{v}$ and $\mathbf{x}$ in a *leap-frog* scheme. Figure taken from Birdsall & Langdon (1991). 42

3.6 Dispersion relation for a 1D electromagnetic FDTD PIC scheme. On the y axis we have the adimensional frequency ω of the wave, while on the x axis the adimensional wavenumber k. The different lines correspond to different Courant conditions. Figure taken from Birdsall & Langdon (1991). 45

3.7 In the simplest, most common type of move, motion of the charge will only create a current across four cell boundaries. A move as shown will create the four fluxes J_{x1}, J_{x2}, J_{y1} and J_{y2} as given in eqs. 3.18-3.21. The coordinates (x, y) describing the location of the charge center at the start of the move are measured relative to the "local origin". Figure taken from Villasenor & Buneman (1992). 46

3.8 Electromagnetic component positions on a Yee mesh. Figure taken from Johnson (checked on: 2017-05-01). 48

3.9 A representation of the non-uniform distribution of the computational domains implemented in the C-3PA code (16x16x16). The structure shown in takes care the load balance issue by taking into account the fact that the central regions have much higher particle number densities. The implementation keeps the original simple cartesian communication between the various sub-domains. Even though this implementation is still not optimum it can reduce the total computational times, relatively to the uniform domains, by ~ 1 order of magnitude. 53

3.10 Blue line: Measure of the growth rate of the two stream instability vs time. On the y-axis we plot E_x, the average amplitude of the electric field component in arbitrary units. On the x-axis we have the time in the simulation in seconds. Black line: the expected growth rate from theory (Birdsall & Langdon 1991). The two vertical red lines indicate where we evaluated the growth rate of the instability, the beginning and the end of the linear phase of the instability. 55

3.11 Initial stage of the simulation of the two stream instability simulation. The plot on the top shows the phase space of the particles on the direction of the streams with v_x and x. The colors distinguish the two streams of the particles. The plot on the bottom shows a sample of the particles in 3D. The vectors indicate the velocity vector $\mathbf{v}$ of the particles sampled, while the color and the dimension of the vectors indicate the magnitude of the velocity $|\mathbf{v}|$. 56

3.12 Linear phase of the two stream instability simulation. The plot on the top shows the phase space of the particles on the direction of the streams with v_x and x. The colors distinguish the two streams of the particles at the initial stage of the simulation. The plot on the bottom shows a sample of the particles in 3D. The vectors indicate the velocity vector $\mathbf{v}$ of the particles sampled, while the color and the dimension of the vectors indicate the magnitude of the velocity $|\mathbf{v}|$. 57

3.13 Linear phase of the two stream instability simulation. The plot on the top shows the phase space of the particles on the direction of the streams with v_x and x. The colors distinguish the two streams of the particles at the initial stage of the simulation. The plot on the bottom shows a sample of the particles in 3D. The vectors indicate the velocity vector $\mathbf{v}$ of the particles sampled, while the color and the dimension of the vectors indicate the magnitude of the velocity $|\mathbf{v}|$. 58

3.14 End of the linear phase/beginning of the non linear phase of the two stream instability simulation. The plot on the top shows the phase space of the particles on the direction of the streams with v_x and x. The colors distinguish the two streams of the particles at the initial stage of the simulation. The plot on the bottom shows a sample of the particles in 3D. The vectors indicate the velocity vector $\mathbf{v}$ of the particles sampled, while the color and the dimension of the vectors indicate the magnitude of the velocity $|\mathbf{v}|$. 59

3.15 Non linear phase of the two stream instability simulation. The plot on the top shows the phase space of the particles on the direction of the streams with v_x and x. The colors distinguish the two streams of the particles at the initial stage of the simulation. The plot on the bottom shows a sample of the particles in 3D. The vectors indicate the velocity vector $\mathbf{v}$ of the particles sampled, while the color and the dimension of the vectors indicate the magnitude of the velocity $|\mathbf{v}|$. 60

3.16 Non linear phase of the two stream instability simulation. The plot on the top shows the phase space of the particles on the direction of the streams with v_x and x. The colors distinguish the two streams of the particles at the initial stage of the simulation. The plot on the bottom shows a sample of the particles in 3D. The vectors indicate the velocity vector $\mathbf{v}$ of the particles sampled, while the color and the dimension of the vectors indicate the magnitude of the velocity $|\mathbf{v}|$. 61

3.17 Non linear phase of the two stream instability simulation. The plot on the top shows the phase space of the particles on the direction of the streams with v_x and x. The colors distinguish the two streams of the particles at the initial stage of the simulation. The plot on the bottom shows a sample of the particles in 3D. The vectors indicate the velocity vector $\mathbf{v}$ of the particles sampled, while the color and the dimension of the vectors indicate the magnitude of the velocity $|\mathbf{v}|$. 62

4.1 The divergence of the electric field, the absolute value of the current density and the projection of the current density on the magnetic field lines for magnetospheres close to the force-free limit for $\alpha = 0°, 45°, 90°$. 64

4.2 Average electromagnetic and magnetic energy density as a function of injection rate, for simulations with injection everywhere and $\alpha = 45°$. The solid lines are the expected values from force-free electrodynamics. According to this quantity the saturation to the force-free value happens at $\mathcal{F} \sim 25\mathcal{F}_{\mathrm{GJ}}$. 66

4.3 The divergence of the electric field and the magnetic field lines in the background. This magnetosphere close to the force-free limit is obtained with particles injected everywhere in the domain with $\mathcal{F} = 25\mathcal{F}_{\mathrm{GJ}}$. 67

4.4 The current density and the magnetic field lines in the background. This magnetosphere close to the force-free limit is obtained with particles injected everywhere in the domain with $\mathcal{F} = 25\mathcal{F}_{\mathrm{GJ}}$. 68

4.5 $\mathbf{J} \cdot \mathbf{B}/B$ and the magnetic field lines in the background. This magnetosphere close to the force-free limit is obtained with particles injected everywhere in the domain with $\mathcal{F} = 25\mathcal{F}_{\mathrm{GJ}}$. 68

4.6 $\langle\gamma\rangle$ and the magnetic field lines in the background. This magnetosphere close to the force-free limit is obtained with particles injected everywhere in the domain with $\mathcal{F} = 25\mathcal{F}_{\mathrm{GJ}}$. 69

4.7 Effect on the particle energy distribution of the different resolution of λ_{sd} in two PIC simulations approaching the force-free limit ($\alpha = 45°$, $\mathcal{F} \sim 25\mathcal{F}_{\mathrm{GJ}}$). We show the particle energy distribution. The selected domain is a spherical shell between $0.36R_{\mathrm{LC}}$ and $2.5R_{\mathrm{LC}}$. In the lower resolution simulation, we have a larger portion of particles between $\gamma \sim 10$ and $\gamma \sim 80$. These particles are heated by not resolving the λ_{sd} and by the aliases introduced with the coarser macro particles. 69

4.8 Effect on E_0 of the different resolution of λ_{sd} in two PIC simulations approaching the force-free limit ($\alpha = 45°$, $\mathcal{F} \sim 25\mathcal{F}_{\mathrm{GJ}}$). We show the distribution of E_0 inside the simulation. The selected domain is a spherical shell between $0.36R_{\mathrm{LC}}$ and $2.5R_{\mathrm{LC}}$. We can see that the noise peak shifts to the right in a lower resolution simulation. 70

4.9 The distribution, in log-log scale, of the E_0/E values calculated at points randomly selected within the spherical shell that is defined by the stellar surface and the sphere with $r = 2.0R_{\mathrm{LC}}$. The point density corresponds to ~ 1 point per computational cell. The plotted results correspond to simulations of $\alpha = 45°$. The different colors correspond to different $\mathcal{F}$ values. $\mathcal{F}$ increases as the color changes gradually from blue to red. The vertical dashed line marks the value to the right of which we consider that the actual acceleration takes place. This Figure is taken from Kalapotharakos et al. (2017a). 71

4.10 Average electromagnetic and magnetic energy density as a function of injection rate, for simulations with injection from the surface and $\alpha = 45°$. The solid lines are the expected values from force-free electrodynamics. According to this quantity the saturation to the force-free value happens at $\mathcal{F} \sim 12.5\mathcal{F}_{\mathrm{GJ}}$. 73

4.11 In this figure we show the close to force-free simulations obtained injecting particles from the surface. We show cases that cover the whole range of inclination angles α. The color is the divergence of the electric field, while the field lines are the magnetic field lines projected onto the poloidal plane. The $0°$ case is obtained with $\mathcal{F} = 5\mathcal{F}_{\mathrm{GJ}} = 5\mathcal{F}^0_{\mathrm{GJ}}$, the $45°$ case with $\mathcal{F} = 12.5\mathcal{F}_{\mathrm{GJ}} = 8.84\mathcal{F}^0_{\mathrm{GJ}}$ and the $85°$ with $\mathcal{F} = 125\mathcal{F}_{\mathrm{GJ}} = 10.89\mathcal{F}^0_{\mathrm{GJ}}$. 73

4.12 Electron and positron energy distribution for near-force-free magnetospheres with different α: when the current sheet is completely positively charged (aligned case) positrons are accelerated at higher energies than electrons, when the current sheet approaches a symmetry of opposite charges ($\alpha \sim 90°$) this difference disappears. 74

4.13 Variation of the Poynting flux and of the dissipation with the radial distance for different injection rates. This plot is for the $\alpha = 45°$ case. 75

4.14 This Figure shows how J and E_0 (this last one defined in Equations 4.8 and 4.9) varies with the injection rate $\mathcal{F}$. The field lines in the background are the magnetic field lines. The gradual screening of E_0 and the formation of the force-free current structure are shown. 76

4.15 Total particle energy distribution for different $\mathcal{F}$. This plot is obtained for solutions with $\alpha = 45°$. 77

4.16 The divergence of the electric field, the absolute value of the current density and the projection of the current density on the magnetic field lines for magnetospheres close to the force-free limit obtained with three different kinds of techniques: force-free electrodynamics, PIC with particles injected everywhere in the domain, PIC with particles supplied only at the surface. As it can be seen, these plots are very similar. 78

4.17 Multiplicity profile for PIC simulations close to the force-free limit: on the right particles are supplied only at the stellar surface, on the left particles are injected everywhere. When particles are injected only at the surface the multiplicity is higher out to a radius of $1R_{\mathrm{LC}}$, similar up to $2R_{\mathrm{LC}}$ and lower up to $3R_{\mathrm{LC}}$. The color scale is logarithmic. 79

4.18 Electronic and positronic modulus of the current densities for PIC simulations close to the force-free limit: one is with particles supplied only at the star's surface, the other is with particles injected everywhere. 80

4.19 Electronic and positronic projection of the current density on the magnetic field lines for PIC simulations close to the force-free limit: one is with particles supplied only at the star's surface, the other is with particles injected everywhere. 81

4.20 Most common particle trajectories in the simulation approaching force-free with particles supplied close to the surface. The color on the trajectories represents the Lorentz factor (γ). A) is a "not so highly" accelerated positron. B) is a positron flowing out from the polar cap flow at low energy. C) is an electron flowing out from the polar cap flow at low energy. D) is a "highly accelerated" positron. E) is an intermediate energy electron flowing out from the polar cap. In the picture on the bottom, we have a volume rendering of E_0 (Equation 4.8, 4.9) that identifies the current sheet: we can see that the difference in acceleration between A) and D) is due to the strength of E_0 on the trajectory. This non uniformity in E_0 is found only through PIC simulations and it can be useful to model the γ-ray emission. All the trajectories are in the corotating frame. 83

4.21 Electron trajectories falling back on the star from different heights. The Lorentz factor γ is the color on the trajectory. We added a red arrow representing the magnetic moment, because the zoomed region could be difficult to identify. Note that the color scale has a different range with respect to all the others shown in this paper for trajectories. This is because of the low energy of these particles. The trajectories are in the corotating frame. 84

4.22 Electron trajectories circling around the Y-point and the light cylinder. Identifying the light cylinder might be difficult, however looking at where the last closed magnetic field lines are is a good approximation 85

4.23 Positron trajectories flowing from the polar cap into the current sheet. The star with the magnetic field lines is plotted on the background. The yellow opaque surface is the pulsar current sheet. We use an opaque profile instead of a volume rendering profile (as in Figure 4.20) in order to facilitate seeing that the trajectories shown are initially outside the current sheet. We select the current sheet according to Equation 4.13. On the left panel the color on the trajectories is the normalized projection of $\mathbf{p}$ on $\mathbf{E}$, as defined in Equation 4.12. We can see that the value is larger than 0.5 in many parts of the trajectories. On the right panel the color is the divergence of the electric field along the trajectories. We can see that these positrons are transitioning from a negatively charged region, to a positively charged region. The trajectories are in the corotating frame. 86

4.24 The particle trajectories that we presented above, but for the aligned rotator. For clarity, we remove the azimuthal component of their trajectory. The magnitude of the azimuthal components were similar to the trajectories shown in the Figures 4.21, 4.22, 4.23, for the 45° case. The red dot indicates where the particle is injected. All these trajectories have large azimuthal components. The color is a label to help distinguish their intricate trajectories. A) is one of the electrons that starts from the polar cap outflow and get turned back into the separatrix and the returning current. B) is one of the electrons that reaches the Y-point, circles for a while and then flies out following another field line. C) is one of the electrons that reaches the Y-point, circles with huge azimuthal components, and then falls back to the star losing energy. D) is one of the positrons that starts in the polar cap flow, close to the separatrix, crosses field lines and then enters the current sheet. 87

List of Tables

2.1 Plasma estimated conditions in the radial direction. 36

Thesis Overview

This thesis is the result of my research conducted between the University of Milan (Milan, Italy) and the NASA Goddard Space Flight Center (Greenbelt, MD-USA). The working group at NASA Goddard is composed by Dr. Alice K. Harding, Dr. Constantinos Kalapotharakos, Dr. Andrey N. Timokhin and Dr. Demosthenes Kazanas. The research project is about understanding the pulsar magnetosphere. The main reasons for which this topic is interesting are the exploration of a very extreme environment for plasma physics and understanding the extensive phenomenology of pulsars. For many years, the theoretical understanding of these magnetospheres advanced only with the classic "paper and pencil" method. It is actually impressive to see how close the ideas of these theorists were to reality. Then, researcher thoughts started to be supported by simulations. Two very important steps are the first force-free simulation for an aligned rotator (Contopoulos et al. 1999) and the first force-free simulation for an inclined rotator (Spitkovsky 2006). Contopoulos et al. (1999) is the first simulation in which the pulsar magnetosphere can be simulated outside the neutron star light cylinder (see later for a definition). This new result showed the potential of simulations for this problem. Spitkovsky (2006) has the merit to have simulated for the first time the pulsar magnetosphere for an inclined rotator, the most relevant case for pulsars. This opened the road to the comparison of these plasma physics models with the observations. Before these works, scientists were using the so called "gap models" that are built on vacuum magnetic field models. The advent of Fermi (Abdo et al. 2013a) boosted the efforts in this field, because it provided a statistically solid population of γ-ray pulsars to investigate. After the force-free simulations, scientists tried to reproduce the emission seen by Fermi roughly modeling the dissipation in the ideal plasma inside the so called dissipative models. Besides some very good results, that approach did not allow us to understand the underlying dissipative mechanism of the magnetosphere. I did my master thesis with Dr. Harding and our work described very well the Fermi observations (Brambilla et al. 2015). However, we decided to take a step back into theory and try to use the technique of Particle-In-Cell (PIC) to allow a study of how this non ideal dissipation arises. I started using a publicly available PIC code, EPOCH (Arber et al. 2015), but then Dr. Kalapotharakos wrote from scratch a PIC code (Kalapotharakos et al. 2017a) and we decided to concentrate our efforts on this code. I helped in developing and testing the code. All the visualizations obtained in this thesis are done through the software VisIt (Childs et al. 2012) and the file formats SILO (https://wci.llnl.gov/simulation/computer codes/silo Accessed: 20/10/2017) and VTK (https://www.vtk.org/ Accessed: 20/10/2017) that I implemented in the code. Here we report the results of our research.

This thesis is structured in four chapters:

- In Chapter 1 I give a background of the science related to pulsars.
- In Chapter 2 I give a background of the plasma physics and the other theories that are necessary to understand the pulsar magnetosphere.
- In Chapter 3 I describe how PIC codes work and how they are used to simulate the pulsar magnetosphere.
- In Chapter 4 I describe our PIC simulations of the pulsar magnetosphere and what we understood. Part of this work, is contained in two papers that we submitted in October (Brambilla et al. 2017; Kalapotharakos et al. 2017a).

At the end I conclude summarizing the results and giving some outlooks.

CHAPTER 1

Pulsar Science Background

Neutron stars (NSs) are the remnants of massive stars whose cores collapse during the supernova explosions at the end of their nuclear fusion lifetimes. Conservation of both the angular momentum and the magnetic flux of the progenitor star during the collapse gives the neutron star a high spin rate and magnetic field. The collapse ends when the degeneracy pressure of neutrons balances the gravitational forces of the matter. NSs typically have detectable pulsations, since they are rapidly spinning and their emission patterns are highly anisotropic, for this reason they are also called pulsars. In this chapter we give a brief background about science involving pulsars, focusing on the young γ-ray pulsars seen by the Fermi Gamma-ray Space Telescope, that are often the paradigm for magnetosphere studies.

1.1 Neutron stars basics

The idea that an atomic nucleus squeezed in a gigantic nucleus[1] can exist in the form of a star was first proposed by Landau (1932) even before the discovery of the neutron (Yakovlev et al. 2013). The idea that such a star, composed by neutrons, can be formed after a supernova explosion was first proposed by Baade & Zwicky (1934). J. Bell during an observing run in 1967 marked the birth of observational pulsar astronomy: what initially appeared as oscillating noise in her radio-frequency observations turned out to be, upon further inspection, a periodic signal with period of 1.3 s (Hewish et al. 1968). More discoveries of narrowly pulsed radio signals with extremely stable periods of order $0.03 \div 1$ s followed implying an astrophysical origin. It was soon proposed that these objects were rapidly rotating NSs (Gold 1968; Pacini 1968) .

The basic idea that emerged was of a magnetic rotating dipole, inclined with respect to the axis of rotation, emitting and losing rotational energy. Assuming this simple model and measuring P and $\dot{P}$ it is possible to calculate (usually assuming a $R_{NS} = 10$ km, $I_0 = 10^{45} g\ cm^{-2}$ and that magnetic moment and the axis of rotation are perpendicular) the magnetic field at the stellar surface,

$$B_s = \frac{\sqrt{1.5 I_0 c^3 P \dot{P}}}{2\pi R_{NS}^3} \tag{1.1}$$

the rate of the rotational energy loss,

$$\dot{E} = \frac{4\pi^2 I_0 \dot{P}}{P^3} \tag{1.2}$$

---

[1] "We expect that this must occur when the density of matter becomes so great that atomic nuclei come in close contact, forming one gigantic nucleus". (Landau 1932)

and the age considering the spin-down as a linear function of time,

$$\tau = \frac{P}{2\dot{P}} \tag{1.3}$$

Thus, looking at the pulsar population on a plot with P and $\dot{P}$ gives immediately a lot of information about the objects. This plot is commonly called $P - \dot{P}$ diagram. We will use the $P - \dot{P}$ diagram shown in Figure 1.1 in the next sections.

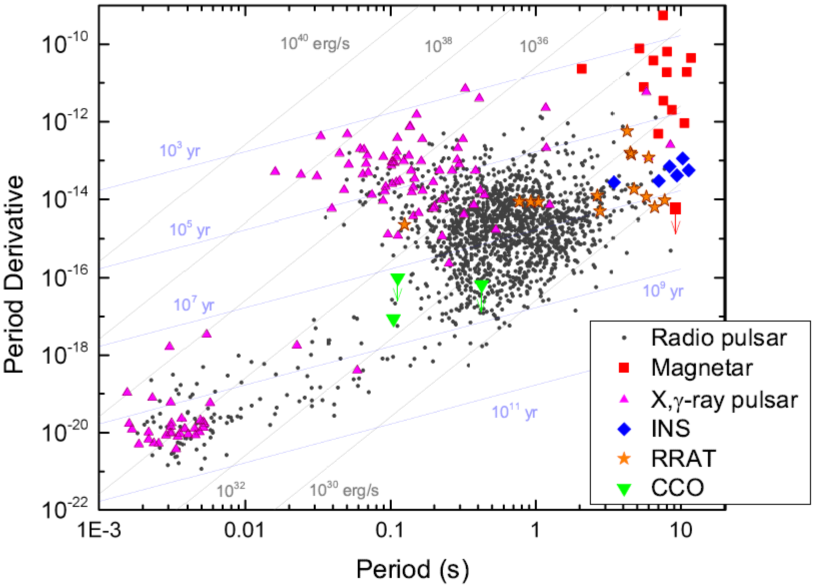

Figure 1.1: $P - \dot{P}$ diagram for rotation-powered pulsars, Isolated Neutron Stars (INS), Compact Central Objects (CCO), Rotating Radio Transients (RRATs) and magnetars. Lines of constant characteristic age, τ, and spin-down luminosity, $\dot{E}$, are superposed. Picture taken from Harding (2013).

1.1.1 The Squeezed Nucleons

The properties of the matter inside the NS are difficult to investigate. The gravitational force is balanced by the nuclear interactions because when the nucleons are closer than 1 fm the strong-interaction becomes repulsive (Shapiro & Teukolsky 1983). This is the only place in which the nuclear physics can be investigated at so high density. Usually a NS has a mass between $1.5 \div 2.5 M_{\odot}$, a radius of $\backsim 10$ km and so a density of $\backsim 10^{15} g$ cm^{-3}. One of the aims of pulsar astronomy is to contribute to the understanding of the equation of state (EoS) of this matter. The strategies are measuring the maximum mass of a NS (Antoniadis et al. 2013; Demorest et al. 2010), performing high precision measures of the radius of NSs with a known mass (Miller & Lamb 2017, 2015; Gendreau et al. 2012), modeling neutron star oscillations and from there inferring the mass (Mahmoodifar & Strohmayer 2017) or through the study of glitches[2] (Pizzochero et al. 2017).

---

[2] A glitch is a sudden increase of the pulsar period.

1.1.2 The Radio Emission

Pulsars were detected first in the radio and there is a lot of science that can be done at these wavelengths. The radio emission is thought to be located very close to the poles, but its origin is unknown. The radio emission power is too high to be emitted thermally and so it should be caused by a coherent mechanism. The two main hypotheses involves population inversion (e.g. laser and maser) or bunching of particles (Michel 1991a). The geometry of the radio emission has been modeled with a core beam surrounded by concentric hollow cones (see for example Rankin (1983, 1990) and Figure 1.2). The width of the core and the cones is proportional to $P^{-1/2}$, except for a category of old pulsars with periods of a few milliseconds (millisecond pulsars, MSPs). The width of the cones present a dependence on the frequency too (Gonthier et al. 2004). An important feature of the radio emission is that it is polarized, usually linearly but sometimes with important amounts of circular polarization as well. Many pulsars display a swing in the position angle of the linear polarization with phase. This variation is S-shaped (see Figure 1.3). This peculiar shape can be used, with the so called Rotating Vector Model (RVM, first proposed in Radhakrishnan & Cooke (1969)), to calculate the inclination angle α of the magnetic axis with respect to the rotation axis and the angle between the magnetic axis and the line of sight of the observer β. A change in the sense of circular polarization is frequently observed in the middle of a pulse too (Michel 1991a).

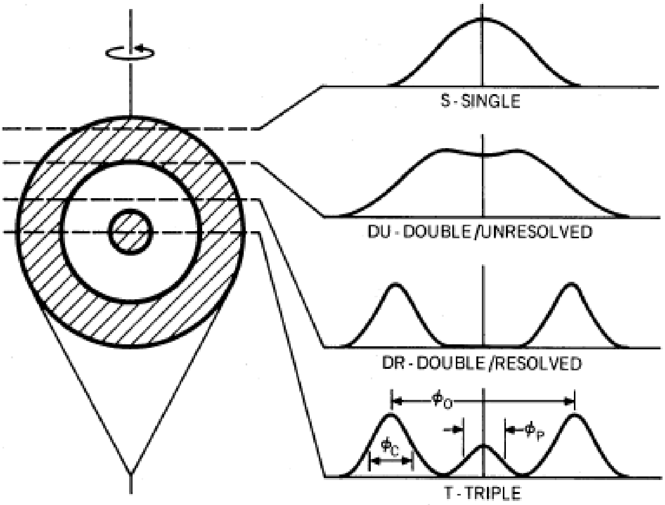

Figure 1.2: On the left, a sketch of the hollow cone geometry, on the right the averaged wave forms that would be viewed by four observers with different inclinations from the rotation axis. Figure taken by Backer (1976).

Pulsars are considered like clocks[3] for their precision in spinning and slowing down. There is a type of study, called *pulsar timing*, dedicated to extract information from this extraordinary behavior. *Pulsar timing* refers to the process by which one calculates the precise arrival time of each pulse of emission from a given pulsar. A timing solution is

---

[3] Their clock properties were used in the famous Voyager Golden Record to indicate the date in which the spacecraft left the Earth (Showstack 2013).

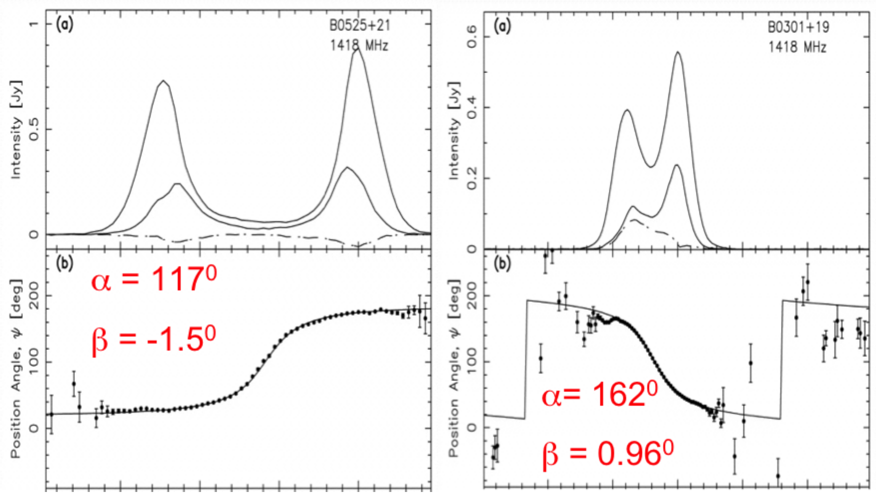

Figure 1.3: In this figure are shown some very good RVM data and the model used to fit them (Everett & Weisberg 2001).

achieved by fitting measured pulse arrival times (TOA) to arrival times predicted from a model of the pulsar rotation and orbital motion, if in a binary system. The precision of this technique opened unexpected possibilities, especially in the theory of gravitation. The first indirect detection of gravitational waves was achieved through pulsar timing of a binary system by Hulse & Taylor (1975). Pulsar binary systems can also test general relativity against alternative theories (Shao et al. 2015). Normal pulsars are usually less stable clocks than MSPs. Correlations between MSP timing residuals[4] can be used to detect gravitational waves: this project is called Pulsar Timing Array (Lommen 2012).

1.1.3 Pulsar Wind Nebulae and the Surroundings

Pulsars form after a SN explosion and they are usually surrounded by some particular structures. Figure 1.4 shows the supernova remnants (SNR), the pulsar wind nebulae (PWN) and a pulsar jet (there can be two jets, see Figure 1.8). The SNR are the expanding debris produced by the shock-wave of the SN explosion (see Figure 1.5 for a SNR and its central object). The SNR are thought to be able to accelerate particles inside their shock-waves up to TeV energies (Aharonian et al. 2004). The PWN is where particle winds from the pulsar magnetosphere are confined. Usually they do not present spherical symmetry but they have a toroidal shape with respect to the rotation axis, identified by the pulsar jets. If the pulsar kick velocity[5] is supersonic, the PWN is deformed creating the shape called bowshock, like the one in Figure 1.6. In Figure 1.7 are shown three different examples of PWNe: one has a clear toroidal shape, one has a clear bowshock-tail and one is an intermediate case. The most studied PWN is the Crab nebula. In Figure 1.8 the central object, the termination shock that is where the pulsar wind pressure balances the nebular pressure (Rees & Gunn 1974), and the jets on the rotational axis are distinguished. Particle acceleration and energy dissipation in PWNe are object of research (Porth et al. 2017).

---

[4] The differences between the timing solutions and the observations.

[5] This velocity is given by a *kick* received in the SN explosion.

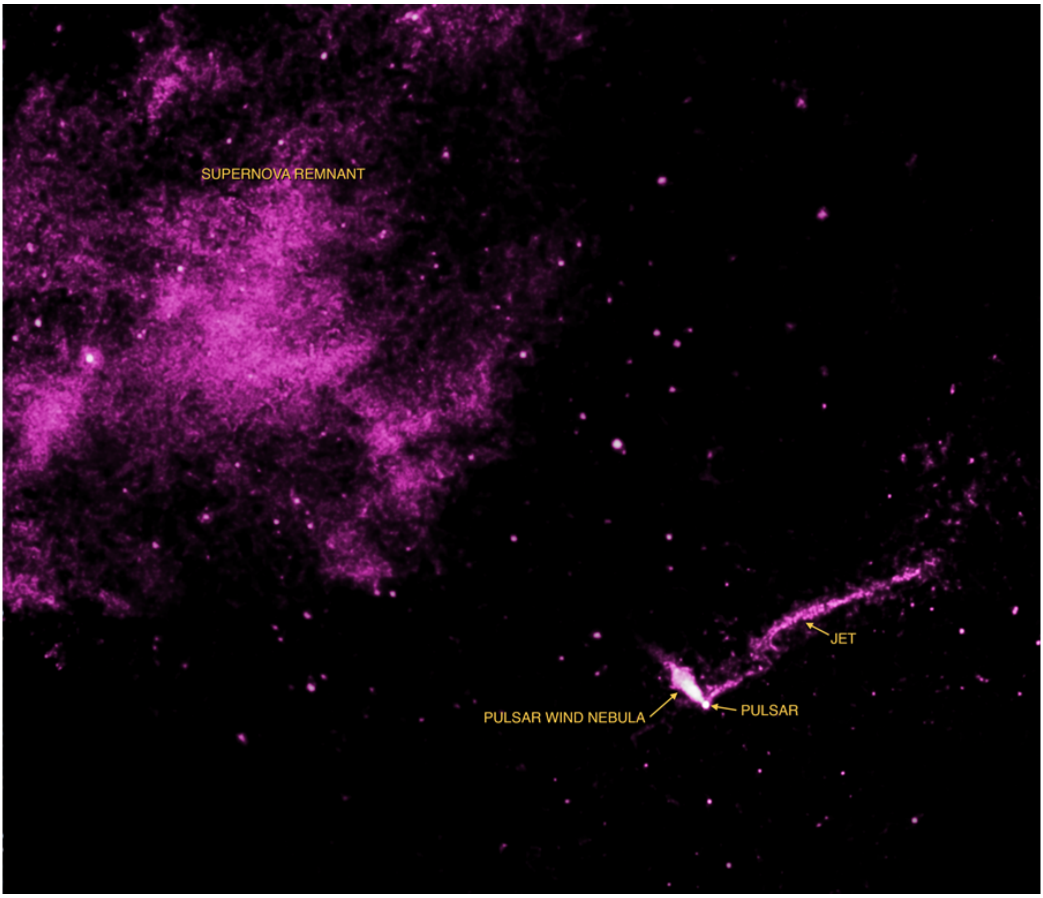
SUPERNOVA REMNANT
JET
PULSAR WIND NEBULA
PULSAR

Figure 1.4: This Chandra image (in the X-band) shows clearly the SNR, the PWN and the pulsar jet of PSR J1104-6103, also called the lighthouse nebula. This picture has been published like Astronomy Picture Of the Day `http://apod.nasa.gov/apod/archivepix.html` (Accessed: 08/10/2017) on 21/02/2014. The same image (without labels) is available on `http://chandra.harvard.edu/` (Accessed: 08/10/2017).

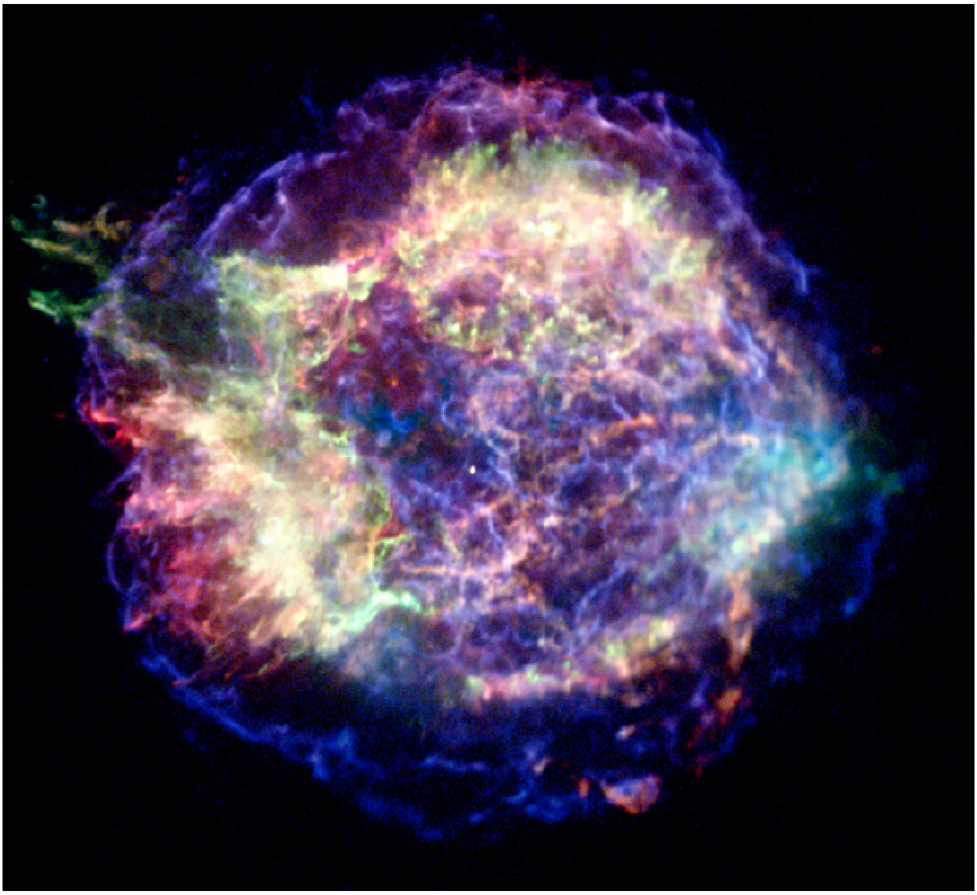

Figure 1.5: In this figure are shown the SNR and the Central Compact Object (CCO, the white point source) of Cassiopea A imaged by Chandra. The color are coded with respect to the photon energies: Red $0.5 \div 1.5$ keV, Green $1.5 \div 2.5$ keV and Blue $4.0 \div 6.0$ keV. The picture is taken from `http://chandra.harvard.edu/` (Accessed: 08/10/2017).

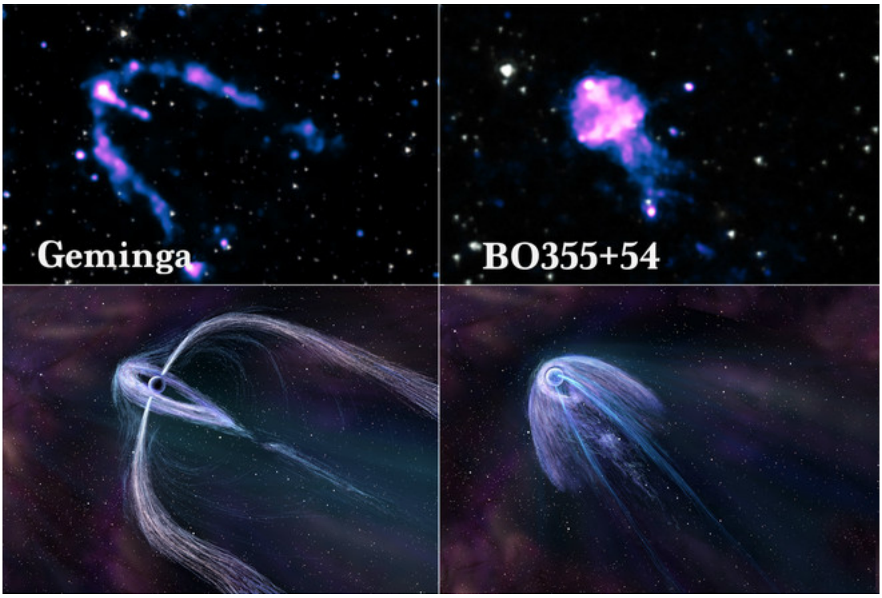

Figure 1.6: In this figure are shown two examples of bowshocks, and two artist impressions that helps in interpreting the image. Here the original capiton: *Images captured by NASA's Chandra X-ray Observatory (top) with artist representations (below) that provided a better look at pulsars and their associated wind nebulae. Geminga, left, is approximately 800 light years from earth. Geminga's tail can stretch more than half a light year longer than 1,000 times the distance between the Sun and Pluto. BO355+54, right, is approximately 3,300 light years from Earth. The narrow, double tail extends almost five light years away from the star. Top Left X-ray: NASA/CXC/PSU/B.Posselt et al; Infrared (BACKGROUND): NASA/JPL-Caltech Top Right X-ray: NASA/CXC/GWU/N.Klinger et al; Infrared (BACKGROUND): NASA/JPL-Caltech Bottom illustrations by Nahks Tr'Ehnl*. Picture taken from `http://news.psu.edu/` (Accessed: 20/10/2017).

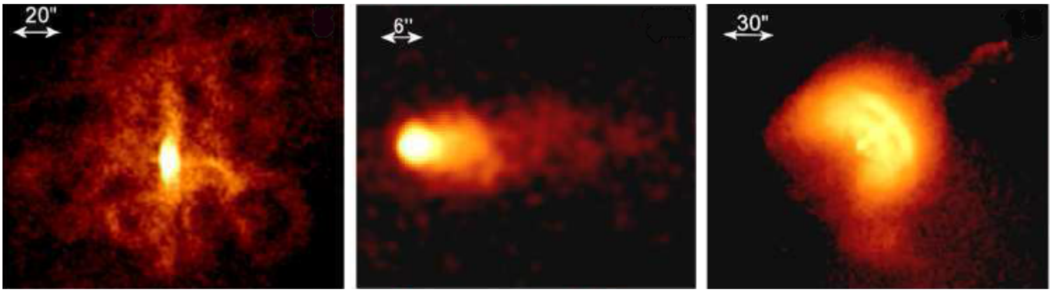

Figure 1.7: In this figure are shown three different examples of PWNe pictured by Chandra in the X-rays: on the left there is a pulsar with a clear toroidal shape (J0205+6449), the central one present a clear bowshock-tail (the Mouse nebula, J1747-2958) and on the right there is one intermediate case (the Vela nebula, J0835-4510). Pictures taken from Kargaltsev & Pavlov (2008).

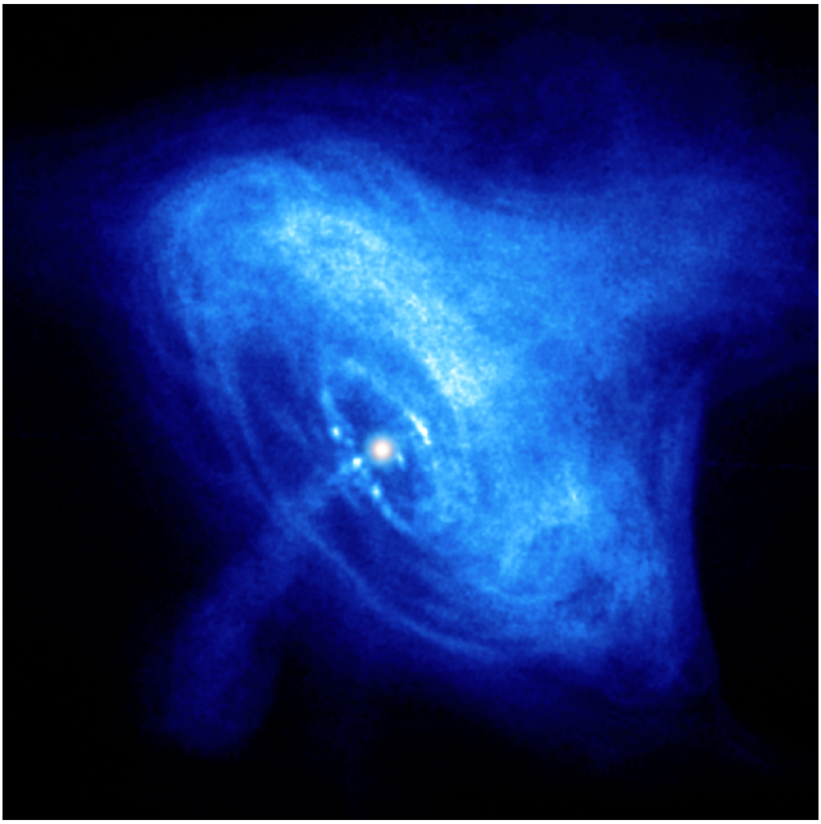

Figure 1.8: This picture shows an X-image of the Crab nebula. The distinguishable parts are the point like object inside the nebula, the two jets departing from it and the wind termination shock where the torus starts inside the nebula. This picture is taken from `http://chandra.harvard.edu/` (Accessed: 08/10/2017).

1.1.4 The Neutron Star Family

There are a lot of different types of NSs. For the class of NSs called rotation-powered pulsars, the first division we can make is based on the spin period between normal pulsars and MSPs. In the γ-ray the distribution is bimodal, with normal pulsars having a period of hundreds of milliseconds and MSPs having a period of a few milliseconds. However, this strict division disappears when we consider the pulsars detected outside of this band. In fact, some objects indicate a smooth transition. It is thought that MSPs are older pulsars that highly increase their period accreting material from a companion star. Another division that can be done is between γ-ray pulsars and the ones that do not emit in the γ-ray band. This division seems to rely on a minimum value of $\dot{E} = 10^{33} erg$ s^{-1} for the γ-ray pulsars, but the physical motivation could be different for normal and MSPs. We will focus on γ-ray pulsars later in Subsection 1.1.5. All these pulsars are spinning down as a result of torques from magnetic dipole radiation and they are known as rotation-powered pulsars (RPP).

The hypothesis that MSPs originate from binaries is supported by the fact that they have the same P and B_s of the Low Mass X-ray Binaries (LMXBs). Moreover, the transition between these two categories has been observed (Papitto et al. 2013). LMXBs are binary systems in which one member is a NS or black hole (BH) and the other star is a low-mass main sequence star, white dwarf or red giant that transfers matter onto the compact object through an accretion disk. Almost all of the radiation is emitted as X-rays and there can be present kHz quasiperiodic oscillations (QPOs, Strohmayer et al. (1996)). In most models of QPOs the oscillation frequencies are the orbital frequencies of accreting matter. Binary systems with a high-mass O or B star as companion are known as High-Mass X-Ray Binaries (HMXB), in a large subset of them the NS orbits a Be star in a very eccentric orbit, accreting material only occasionally in outbursts when the NS crosses a disk of material surrounding the Be star. Another subclass of accreting X-ray binaries are called microquasars since they display properties similar to those of quasars, including rapid variability of their X-ray emission, repeated and sometimes periodic radio, optical and X-ray flaring with associated formation of relativistic jets. Like LMXBs, both HMXBs and microquasars can host either a NS or a BH. Obviously these pulsars cannot be RPPs because their energetics are dominated by the accretion.

Another class of NSs are the magnetars (Kaspi & Beloborodov 2017). Their inferred steady X-ray luminosities are about one hundred times higher than their spin-down luminosities, requiring a source of power way beyond the magnetic dipole spin-down. Thus, magnetars are not RPPs. The source of their luminosity is the conversion of their huge magnetic ($10^{14} \div 10^{16} G$) field into luminous energy (Thompson & Duncan 1995). There are two sub-classes of magnetars, Anomalous X-Ray Pulsars (AXPs) and Soft γ-Ray Repeaters (SGRs), that were thought to be unrelated objects for many years. Now we know that they both show steady X-ray pulsations as well as soft γ-ray bursts. Magnetars do not present a steady emission in the γ-rays.

Other interesting class of objects are the central compact objects (CCO), the isolated NSs (INS) and the rotating radio transients (RRATS). CCOs are X-ray point-like sources detected close to the centers of young SNRs that have no apparent emission in other bands and no binary companions. They have soft, exclusively thermal spectra (but some of them have multiple blackbody components) in the keV range. A CCO can be seen in Figure 1.5 inside its SNR. INSs are NSs that appear to be thermally cooling with no emission outside the soft X-ray band, except for faint optical/UV counterparts. Although these properties are similar to those of CCOs, they are a distinct class because they lack any observable associated SNR or nebula. There are presently seven confirmed INSs, sometimes referred to as *The Magnificent Seven*. It is thought that they are old magnetars in which the magnetic field decayed (Turolla et al. 2015). INSs are interesting to study the cooling of the surface temperature because they present only thermal emission (Turolla 2009). RRATS were discovered only very recently through detections of their single, isolated radio pulses. They show a variety of transient radio behavior, they could stop to emit for long time periods (at least 10^4s) and later return to steady pulsations that are highly modulated. The causes of such radio transient behavior is unknown, but global changes in the currents of the pulsar magnetosphere has been suggested as the possible cause. It is not clear how RRATS fit into the normal RPP population. They share some similar properties with INS, but if they are a separate evolutionary group they would significantly raise the birthrate of NSs in the Galaxy.

The $P - \dot{P}$ diagram reported in Figure 1.1 shows the various characteristics of the classes of pulsars exposed in this subsection. To find more information and more specific references about these families the reader can consult Harding (2013).

1.1.5 γ-ray Pulsars

The launch of the Fermi γ-ray Space Telescope (Atwood et al. 2009a) led to the detection of 205 γ-ray pulsars[6] in the 100 MeV - 10 GeV band by the Large Area Telescope (LAT) (Atwood et al. 2009b). This increased the number of the known γ-ray pulsars by one order of magnitude[7], allowing a systematic study of this population (Abdo et al. 2013a). The strong dependence of the Point Spread Function (PSF) on the energy of the photons make the LAT unable to focus the incident radiation causing some background contamination, so during the observation process is needed to identify the sources from which photons are arriving. In order to do this researchers cannot look only at a point in the sky seen by the LAT but they have to look inside a region of interest (ROI) and to have a good model of the background.

A pulsar can be identified looking for a periodic signal of a point-like source. This search of periodicity is performed with a maximum likelihood statistical analysis (Kerr 2011). This method considers the weights: the time of arrival of the photons, their direction and their energy. If a signal is found, it returns the position, the period and the spectral parameters of the object. Actually, the spectrum of the pulsar is not really needed to detect pulsations, but it can aid in background elimination through weighting the photons with the pulsar spectrum. There are three methods to discover a γ-ray pulsar: the first is using independently determined pulsar timing ephemerides, the second are blind searches of the γ-ray pulsation in the *Fermi* data (pointing mainly toward unassociated sources) and the third is the discovery of the γ pulsations just after the radio or X-ray pulsation discovery at the position of a γ-ray point source. The second one is the most challenging because the set of parameter is larger than the other methods (there is no hint for the period), but it is the only one available to discover radio-quiet γ-ray pulsar. In general the γ-ray pulsation are difficult to detect for the paucity of the γ-ray photons: often there are less than one photon detected in tens of thousands of pulsar rotations (millions for the MSPs). In the 2^{nd} *Fermi* Pulsar catalog (2PC, Abdo et al. (2013a)) the energy range of photons is 100 MeV $\div$ 100 GeV. The photons were collected for 3 years and used a 2° Region Of Interest (ROI) for the search of pulsations and a 15° ROI for the spectral analysis.

The *Fermi* satellite has brought a great contribution to pulsar astronomy. At the moment

---

[6] updated to 2016 February 22

[7] 7 from EGRET (Thompson 2008) and 15 from AGILE (Pittori 2013).

(2017/10/7) *Fermi* detected γ pulsations from 112 young pulsars and from 93 MSPs[8]. The term *young* is used to distinguish these pulsars from the old *recycled* MSPs. Young pulsar are divided in radio loud and radio quiet pulsar. The division is based on a minimum radio flux to which telescopes are sensitive - about 20 μJy. One theory is that radio quiet pulsars are the exactly like radio loud pulsar, but observed from a different line of sight that does not intersect the radio beam. This would make these pulsars to appear as radio quiet (Abdo et al. 2013a). The young pulsars appear distributed on the galactic disc while the MSPs appear spherically distributed around the galactic center (Caraveo 2014). The detected pulsars are highlighted with circles on the γ-ray sky in Figure 1.9. The γ-ray pulsar population is plotted on a $P - \dot{P}$ diagram shown in Figure 1.10.

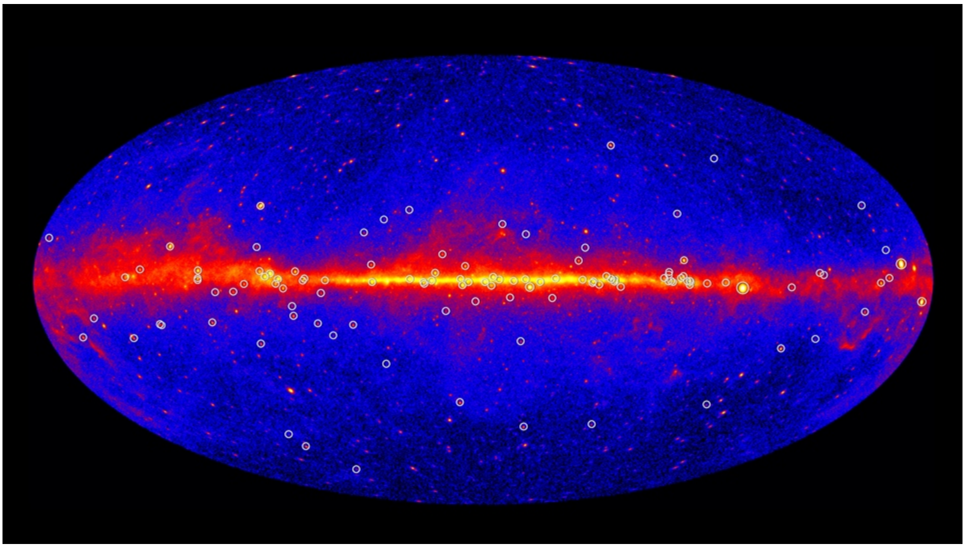

Figure 1.9: *Fermi* five-year map of the sky showing the positions of the 117 pulsars listed in the 2PC. Image from NASA/DOE/Fermi LAT Collaboration `http://svs.gsfc.nasa.gov/` (Accessed: 08/10/2017).

The light curves seen in the 2PC for the young pulsars can be double or single peaked. The shapes of the peaks are various. The emission can either be concentrated only in the peaks or have lower intensity regions outside of them. This lower intensity emission outside the two peaks can be present everywhere around the peaks (off-peak emission) or only between the two peaks (bridge emission). A sample of the 2PC light curves is shown in Figure 1.11. The pulsar spectra are usually modeled in this way:

$$\frac{dN}{dE} = K \left(\frac{E}{E_0}\right)^{-\Gamma} exp\left(-\frac{E}{E_{cut}}\right)^{b} \tag{1.4}$$

This shape is characteristic of processes such as curvature or synchrotron radiation (Jackson 1998a). b helps to describe the overlapping emission of particles with different energies. The b parameter is usually set equal to 1, but there are some pulsar in which the fit works better leaving b free (Abdo et al. 2013a). One of the most important results from the Fermi observations is measuring $b \leqslant 1$. This measure disfavors models

---

[8] `https://confluence.slac.stanford.edu/display/GLAMCOG/Public+List+of+LAT-Detected+Gamma-Ray+Pulsars` (Accessed: 10/10/2017)

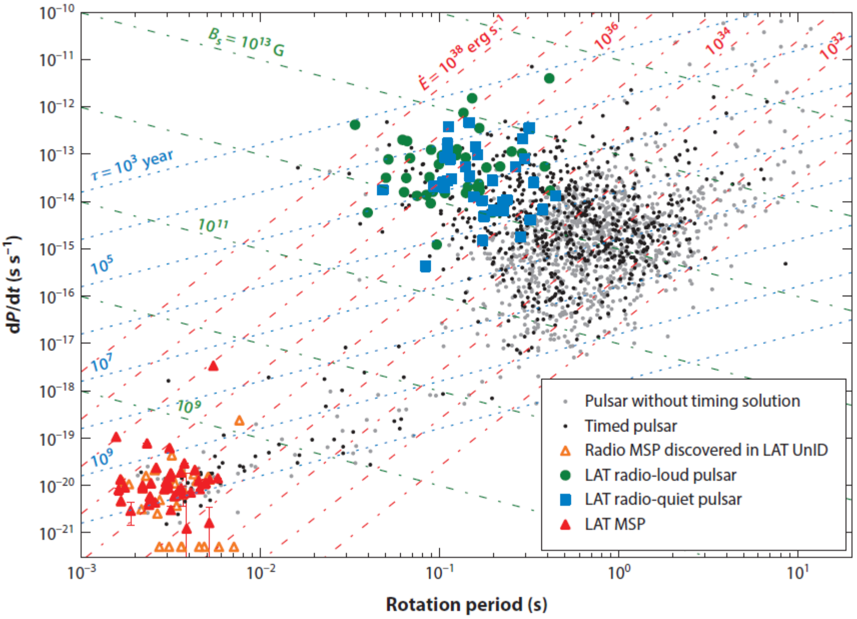

Figure 1.10: $P - \dot{P}$ distribution of the 117 *Fermi* pulsars (radio-loud pulsars shown as green circles, radio-quiet as blue squares, and MSPs as red triangles) plotted together with the entire radio pulsar sample known today (black dots, 710 in all, represent timed pulsars that were phase folded, but not detected, whereas 1337 gray dots represent pulsars without timing solution). Lines of constant rotational energy loss $\dot{E}$, characteristic age τ, and surface B field B_s are also shown. Recently discovered MSPs, for which no $\dot{P}$ has been measured, are plotted at $\dot{P} = 5 \cdot 10^{22}$. All the *Fermi* LAT pulsars lie above $\dot{E} = 10^{33} erg\ s^{-1}$. This picture is taken from the 2PC (Abdo et al. 2013a).

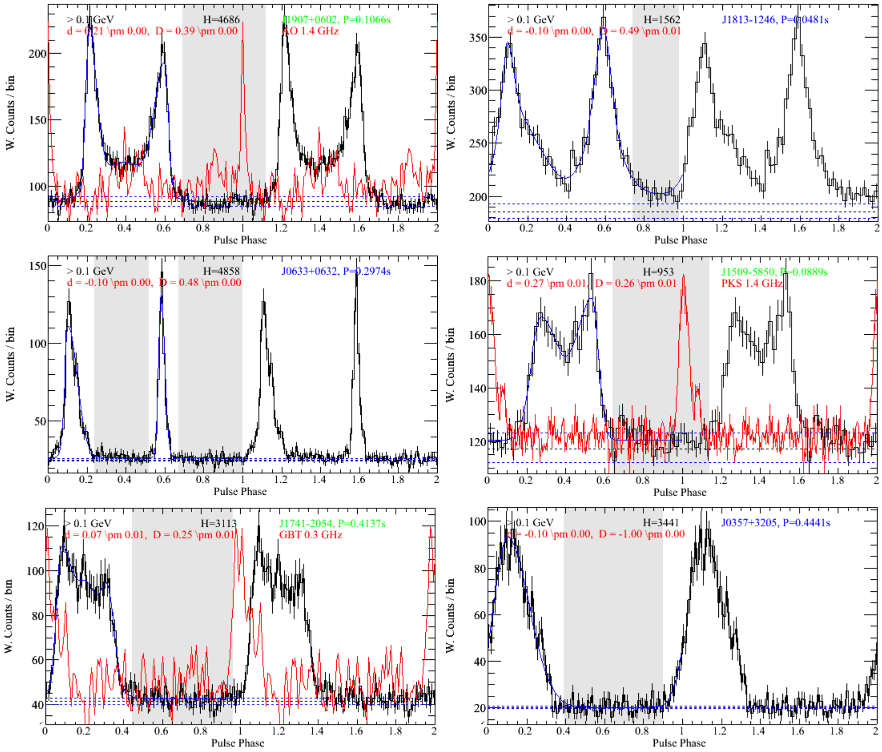

Figure 1.11: These pictures are taken from 2PC Abdo et al. (2013a), from the top to the bottom and from left to right there are shown: J1907+0602 (example of bridge emission), J1813-1246 (example of off-peak emission), J0633+0632 (no bridge, no off-peak emission), J1509-5850, J1741-2054, J0357+3205. The black line is the the γ-ray light curve, the red line is the radio light curve, the horizontal lines are the noise levels (the emission is surely present only when it is higher than the noise levels). On the y axis there are the photon weighted counts (weighted in the sense that they are selected in a maximum likelihood process that use weights), on the x axis there is the phase where 1.0 is a period.

in which the γ-ray emission is produced close to the neutron star surface (Abdo et al. 2009). This would happen because of the strong fields at the surface of young pulsars. Due to the strong fields at the surface of young pulsars, the Quantum Electrodynamics (QED) phenomenon of magnetic pair attenuation would change the particle distribution and produce a spectrum with $b > 1$ (Daugherty & Harding 1996). It is possible to study the pulsar spectra averaged over the whole period (phase averaged spectra) or to study the evolution of the spectra along the rotational phase (phase resolved spectra). This last study needs more photons than the normal phase averaged spectrum, therefore, it cannot be performed for every detected pulsar. Using all these information, detailed model-observation comparisons can be done (Brambilla et al. 2015).

1.2 High Energy Emission Processes and Relativistic Effects

In the pulsar magnetosphere various processes take place. The emission processes can be modified by relativistic and quantum effects. In this section we report the the major processes that are important to the magnetosphere physics. The main references for this chapter are Jackson (1998a); Rybicki & Lightman (1986); Harding & Lai (2006).

A charged particle can be accelerated by the presence of an electric or magnetic field (the acceleration for magnetic fields do no work). When a charged particle is accelerated it emits photons. The formula that describe this behavior is the Liénard or relativistic Larmor formula:

$$P = \frac{2q^2}{3c}\gamma^6[\dot{\beta}^2 - (\boldsymbol{\beta} \times \dot{\boldsymbol{\beta}})^2] \tag{1.5}$$

Where P is the power emitted, q the charge of the particle, c the speed of light, γ the Lorentz factor and $\boldsymbol{\beta} = \mathbf{v}/c$. It can be seen that when the acceleration is parallel to the motion Equation 1.5 becomes:

$$P = \frac{2q^2}{3m^2c^3}\left(\frac{dp}{dt}\right) \tag{1.6}$$

Where m is the particle mass p the particle momentum and t the time. Instead when the acceleration is perpendicular Equation 1.5 becomes:

$$P = \frac{2q^2}{3m^2c^3}\gamma^2\left(\frac{dp}{dt}\right) \tag{1.7}$$

Therefore, the power emitted for a given force is larger when the force is applied perpendicularly to the motion. This happens because the rate of change in momentum for a relativistic particle is greater when the force is perpendicular to the motion. The relativistic motion of particles changes also the angular distribution of the power emitted: this phenomena is called *beaming*, because increasing the velocity of the particle, the emitted radiation focuses in a smaller solid angle.

1.2.1 Curvature Radiation (CR)

Curvature radiation (CR) is the radiation emitted from a particle accelerated along a curved line by centripetal acceleration. This emission mechanism happens for example in the pulsar magnetosphere when the particles are accelerated by a force toward the radius of curvature of the magnetic field lines. The synchrotron radiation (SR) is a particular case of CR[9] but we will discuss it separately. The averaged $\langle \quad \rangle$ power is beamed toward the direction of the velocity:

---

[9] The CR was called SR because it was first observed in electron synchrotrons (Jackson 1998a).

$$\langle \theta^2 \rangle^{\frac{1}{2}} \sim \gamma^{-1} \tag{1.8}$$

where θ is the direction of the emission with respect to the direction of the motion. This behavior changes with the radiation frequency, but the dependence on γ appears both in the low and high frequency limits. For ultra relativistic particles the emission can be considered parallel to the direction of motion. The energy radiated per unit frequency interval is (Jackson 1998a)

$$\frac{dI}{d\omega} = \sqrt{3}\gamma \frac{e^2}{c} \frac{\omega}{\omega_c} \int_{\omega/\omega_c}^{\infty} K_{\frac{5}{3}}(x)\, \mathrm{d}x. \tag{1.9}$$

Where I is the energy emitted, ω the radiation frequency, ω_c is

$$\omega_c = \frac{3}{2}\gamma^3 \frac{c}{\rho} \tag{1.10}$$

is the critical frequency where ρ is the radius of curvature of the curve. K is a modified Bessel function. Calculating the integral, the total energy loss is of the order of $3e^2\gamma^4/\rho$. The integral of the function depending on the frequencies is shown in Figure 1.12. To convert energy to power we merely multiply the Equation 1.9 by the repetition rate $c/2\pi\rho$. To pass from power to number of photons per second we divide by $\hbar\omega$. To pass in energy units respect to frequency we divide by $\hbar$.

1.2.2 Synchrotron Radiation (SR)

As we said in the previous section SR is a special case of CR, where the acceleration is due to the Lorentz force that is perpendicular to the magnetic field line. The total power emitted per frequency by one particle is:

$$P(\omega) = \frac{\sqrt{3}q^3 B \sin\chi}{2\pi m c^2} y \int_{y}^{\infty} K_{\frac{5}{3}}(x)\, \mathrm{d}x. \tag{1.11}$$

Where $y = \omega/\omega_c$. It is easy to see the similarity with Equation 1.9. The additional dependences are from the intensity of the magnetic field B and from the pitch angle χ (the angle between the magnetic field line and the velocity of the particle). When we model SR, it is crucial to model the distribution of the pitch angles that depends directly on the physical mechanisms proposed in the model. The highest energy of synchrotron photons is limited. In the so called *burn-off* limit (de Jager et al. 1996), the maximum energy gain provided by electromagnetic fields is balanced by the synchrotron losses, giving a maximum energy of 160 MeV. However, this limit can be broken by Doppler boosting (de Jager et al. 1996) or by electric fields stronger than the magnetic ones (Kagan et al. 2015).

1.2.3 Compton and Inverse Compton Scattering

Compton scattering refers to the general process by which radiation is scattered off of free electrons (or positrons). A photon that undergoes Compton scattering changes its direction of propagation by an angle θ relative to its original direction, and also undergoes a change in energy ϵ. For low photon energies, Compton scattering is approximated

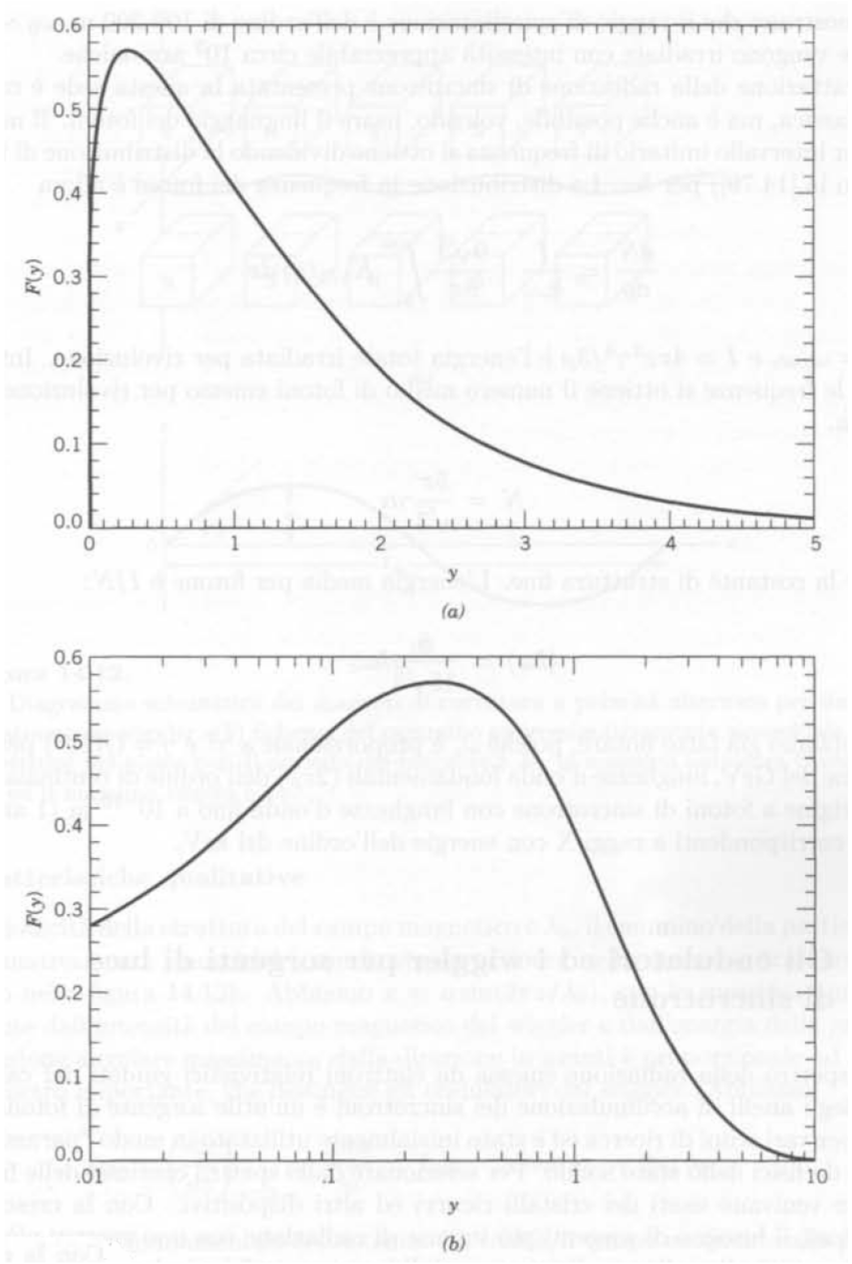

Figure 1.12: Normalized spectra of CR $(1/I)(dI/dy) = (9\sqrt{3}/8\pi)y\int_y^\infty K_{\frac{5}{3}}(x)\,\mathrm{d}x$, where $y = \omega/\omega_c$ and $I = 4\pi e^2\gamma^4/3\rho$. *(a)* y axis with a linear scale, *(b)* y axis with a logarithmic scale. Picture taken from Jackson (1998a).

by classical Thomson scattering. For high $\epsilon\gamma$ where γ is the electron Lorentz factor, quantum effects become important resulting in the total Klein-Nishina cross section (KNCS). The KNCS for extremely high energy photons is:

$$\sigma_K = \frac{3}{8}\sigma_T x^{-1}\left(\ln 2x + \frac{1}{2}\right) \tag{1.12}$$

Where $\sigma_T = 6.65 \cdot 10^{25} cm^2$ is the Thomson cross-section and $x \equiv h\nu/mc^2$, so for high energy photons and electrons $x \gg 1$. In high energy astrophysics, the kinetic energy of the electrons (or positrons) is often greater than the energy of the photons. In this case, energy can be transferred from the particles to the photons. This process is called Inverse Compton scattering (IC). For a highly relativistic particle doing Inverse Compton the final photon energy is (for photon energies $\leqslant$ 100 keV, for higher energy photons, like the ones in *Fermi*, we need to include QED effects) $\epsilon_{ph} \sim \epsilon_e\gamma^2$. In general both IC and Compton scattering energies depend on the scattering angle (the differential cross-section is not uniform). IC is an essential process in the model of magnetar magnetospheres (Zane et al. 2009) and it is thought to produce the pulsar emission seen above 100 GeV (Lyutikov et al. 2012).

1.2.4 Single and Double Photon Pair Production and Photon Splitting

This subsection is focused on three processes that happen in strong magnetic fields. The main reference is Harding & Lai (2006), sections 5.4 and 5.6.

Single photon pair production is the process by which a single photon produces an electron-positron pair. This process cannot occur in a field-free space because energy and momentum cannot both be conserved. However, in the presence of a strong magnetic field with nonzero transverse component to the photon direction, the field absorbs the extra momentum, and single photon pair production can occur. This is a phenomenon predicted by QED. Single photon pair production is an important process in pulsar magnetospheres for $B \geqslant 0.1B_Q$ where $B_Q = m_e^2c^3/(e\hbar) = 4.414 \cdot 10^{13}G$ is the quantum critical magnetic field strength. This phenomenon can happen also for lower magnetic fields, but a higher photon energy is needed. The inverse process of single photon pair production is single photon pair annihilation, in which an electron-positron pair annihilates to form a single photon. The rate of one-photon pair annihilation increases exponentially with increasing B, and surpasses two-photon pair annihilation at $B \sim 10^{13}G$. Single photon pair production is the mechanism that dictated the magnetic attenuation of the pair cascade γ-ray spectrum computed by Daugherty & Harding (1996).

Double photon pair production conserves both energy and momentum, therefore, it can occur in the absence of a magnetic field for sufficiently high photon energies. The sum of the photon energies must exceed $\approx 2m_ec^2$ in the center of momentum frame in order to create a pair. In a strong magnetic field, only the energy and the parallel momentum must be conserved: in fact the photons can absorb extra perpendicular momentum from the magnetic field. This means that photons propagating parallel to each other can pair produce, in contrast to a field-free space. As for single photon pair production, the inverse of two-photon pair production is the annihilation of a pair into two photons. This process is sharply cut off for $B \gtrsim 0.2B_Q$. Additionally, as B increases, an asymmetry in the energies of the produced photons grows so that the process begins to resemble single photon pair annihilation.

Photon splitting is a process by which one photon propagating through a strong magnetic field divides into two or more photons. Although photon splitting conserves energy and momentum even in the absence of a field, photon splitting occurs only due to

QED effects. The rate of photon splitting is:

$$R_{sp} \propto \epsilon^5 B'^6 \sin^6 \theta \tag{1.13}$$

where ϵ is the photon energy in mc^2 units, B' the magnetic field in B_Q units and θ the angle of propagation relative to the field. Photon splitting occurs at any photon energy, unlike pair production. R_{sp} becomes independent from the magnetic field when $B \sim B_Q$. Single photon pair production is a first-order process, while photon splitting is a third order process, therefore, the rate of photon splitting is smaller than the one of single photon pair production. However, because R_{sp} is so sensitive to B, in very strong magnetic fields photons may split before reaching the pair production threshold. Moreover, for $B \geq B_Q$ this mechanism becomes even dominant. This is important for particle acceleration and radiation in the low-altitude, polar cap region of pulsar magnetospheres.

1.2.5 Aberration and Retardation

The relativistic effects playing a role in pulsar emission are the aberration and the retardation of the photons. The star exterior magnetic field and the plasma corotate with the star itself (this will be explained in Chapter 2). In spherical coordinates (r, ζ, ϕ) the corotation velocity at the radius r is $\beta_{rot} = \Omega r \sin\zeta / c$, where ζ is the angle between the rotation axis and $\mathbf{r}$. First order special relativistic effects become important when r is a significant fraction of the R_{LC}. Beyond the R_{LC} the magnetosphere cannot corotate and the phenomenon cannot be described analytically. Aberration causes the photon emission directions to appear shifted to a non-rotating observer in the direction of rotation, so that the emission arrives at an earlier phase (Harding 2005). The standard vectorial aberration formula from special relativity is (Dyks & Rudak 2003)

$$\mathbf{k} = \frac{\mathbf{k}' + [\gamma + (\gamma - 1)(\boldsymbol{\beta} \cdot \mathbf{k}')/\beta^2]\boldsymbol{\beta}}{\gamma(1 + \boldsymbol{\beta} \cdot \mathbf{k}')} \tag{1.14}$$

Where $\mathbf{k}$ is the wave vector in the inertial frame, $\mathbf{k}'$ is the wave vector in the corotating frame and $\boldsymbol{\beta} = \mathbf{v}/c$ where $\mathbf{v}$ is the velocity vector. Retardation (or time of flight delay) is a simple effect due to the finite speed of light and to the high spin frequency of the pulsar. It consists in the fact that for two photons emitted at the same phase in the corotating frame but at different altitudes, arrive to a non rotating inertial observer at a different phase: the photon that was emitted at the higher altitude had less space to travel and so it arrives at the observer's eye at an earlier phase than the one emitted at a lower altitude. The term to subtract from the apparent phase is (see Figure 1.13):

$$\mathbf{r_A} \cdot \mathbf{v_A} / (v_A \cdot R_{LC}) \tag{1.15}$$

where $\mathbf{r_A}$ is the particle position vector and $\mathbf{v_A}$ is the velocity position vector, that indicate the distance already travelled by the photon. It can be seen that the combination of these two effects give origin to the high energy double peak profile of pulsars (Harding 2005). For a practical implementation on a magnetosphere model see Kalapotharakos et al. (2017a).

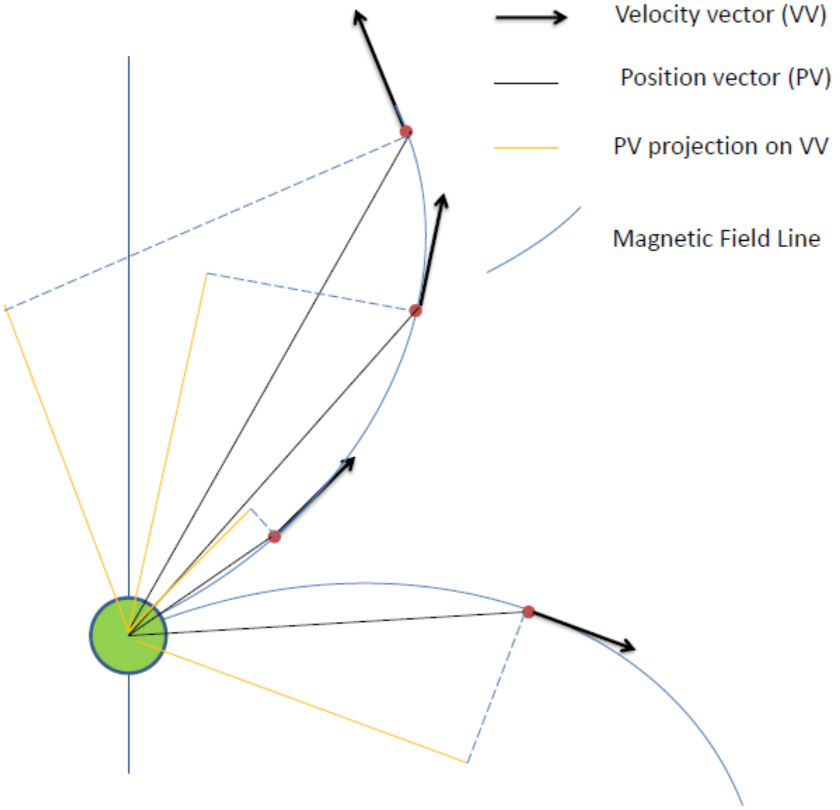
Velocity vector (VV)
Position vector (PV)
PV projection on VV
Magnetic Field Line

Figure 1.13: This picture show the time of flight for different particles on the field lines. The yellow line is $\mathbf{r_A} \cdot \mathbf{v_A}/(v_A \cdot R_{LC})$ where $\mathbf{r_A}$ is the particle position vector and $\mathbf{v_A}$ is the velocity position vector.

CHAPTER 2

The pulsar magnetosphere problem: Theory

2.1 Introduction

The interest in the pulsar magnetosphere started when rotating magnetic neutron stars have been proposed as the energy source in supernova remnants by Wheeler (1966) and Pacini (1967). The neutron star is considered as a simple rotating inclined dipole emitting electromagnetic waves that power the supernova remnants. Then Gold (1968) and Pacini (1968) suggested that these objects were the recently discovered pulsars (Bell & Hewish 1967). The first model for the plasma in such an object was proposed by Goldreich & Julian (1969).

In this chapter we will not follow an historical approach[1], but we will present the main topics as they are important at the current time. In the next section we will introduce the Deutsch solution that describes a uniformly magnetized conductive sphere in vacuum. In Section 2.3 we will review the plasma theory of the force-free magnetosphere. A brief overview of the locations and mechanisms that can supply the plasma is given in Section 2.4. In the last section we will check the consistency of this scenario estimating the conditions of the magnetospheric plasma.

2.2 The Deutsch solution

In the previous section and in the introductory chapter of this thesis we said that a pulsar acts as an inclined magnetic rotating dipole. Therefore the simplest description of the magnetic field around the pulsar is given by a conductive sphere in vacuum uniformly magnetized. This solution, proposed in Deutsch (1955), was presented more than a decade before the discovery of pulsars. The purpose was to study the magnetosphere of normal stars. A good in-depth analysis of the solution with respect to pulsars is given in Michel & Li (1999). Here I am going to describe only its main features.

2.2.1 The fields and the field lines

The speed of the corotating[2] frame of the star increases with respect to the distance of the point we consider from the axis of rotation. At a certain distance, this speed reaches and surpasses the speed of light. This locus is called the light cylinder (LC)

$$R_{\mathrm{LC}} = \frac{c}{\Omega} \tag{2.1}$$

---

[1] An account of the theory developed until the nineties can be found in Michel (1991b).

[2] A frame rotating with the same angular velocity of the star's surface.

Where $\Omega = 2\pi/P$ and P is the neutron star period. This zone is very important because it divides the magnetosphere into two parts. In the part inside the LC, the fields are able to corotate with the star. This is because the fields travel at the speed of light, and the frame's velocity inside the LC is less than c. However, the field lines beyond the LC are not traveling fast enough to follow the corotation and are therefore swept back. Figure 2.1 illustrates this behavior, which is exhibited by an inclined dipole. In the case of an aligned dipole, the fields have cylindrical symmetry; as a result, this change is not seen. Another big difference between the the two dipoles is the intensity of the aligned dipole's electric field is lower than the one generated by the inclined dipole. This is because the only relevant contribution comes from the motion of the ideal circuit through the magnetic field.

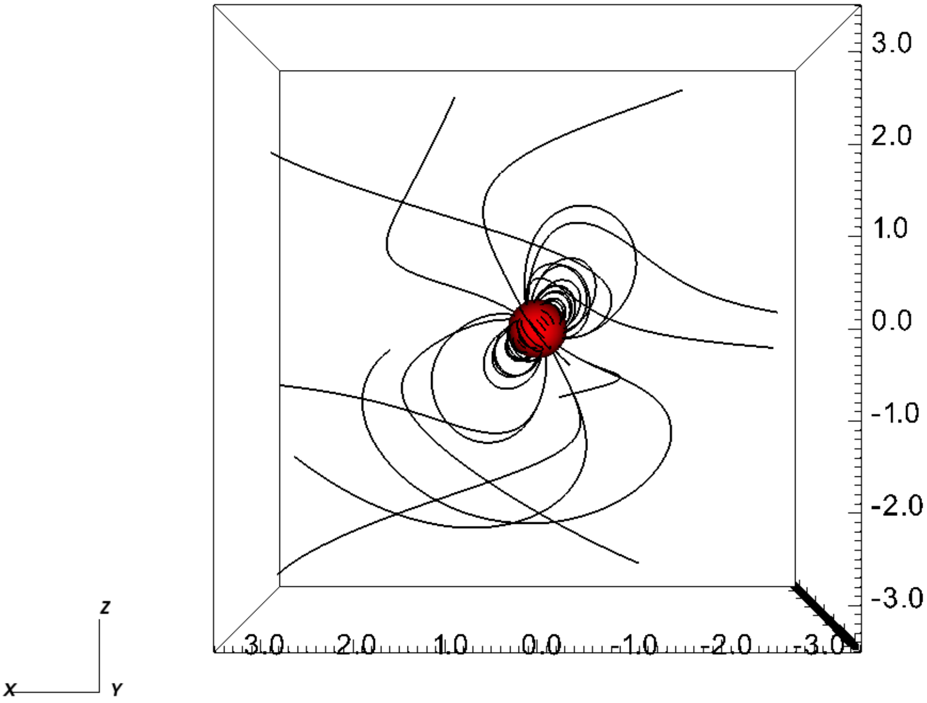

Figure 2.1: In this Figure there are shown the open and closed magnetic field lines for the Deutsch solution of a 45° inclined rotator. The axes are in R_{LC} units. This picture has been obtained using the software VisIt (Childs et al. 2012).

The LC divides the field lines of an inclined dipole into two categories: the field lines inside the LC can close whereas the field lines that cross the LC are swept back and therefore cannot close. In this way, there are some lines that are open and others that are closed. While this might appear to contradict $\nabla \cdot \mathbf{B} = 0$, it is actually quite standard. Look at Figure 2.2; outside the LC the fronts of the open magnetic field lines become parallel. This marks the transition from the static zone to the radiation zone, and the LC is exactly at the induction zone[3]. This explains the apparent contradiction of the open field lines because it shows that they form a radiation field, which becomes more as an electromagnetic wave with a planar wavefront as we go further in the radiation zone. In a radiative field, the field lines are changing direction smoothly passing through a zero amplitude point, as it happens for a sinusoidal wave. This explain why $\nabla \cdot \mathbf{B} = 0$ is enforced, because the field lines are not interrupted and they smoothly pass from pointing in one direction to the other. Moreover, a radiation field scales as r^{-1} and the divergence for such a field is zero (look at the expression in cylindrical coordinates).

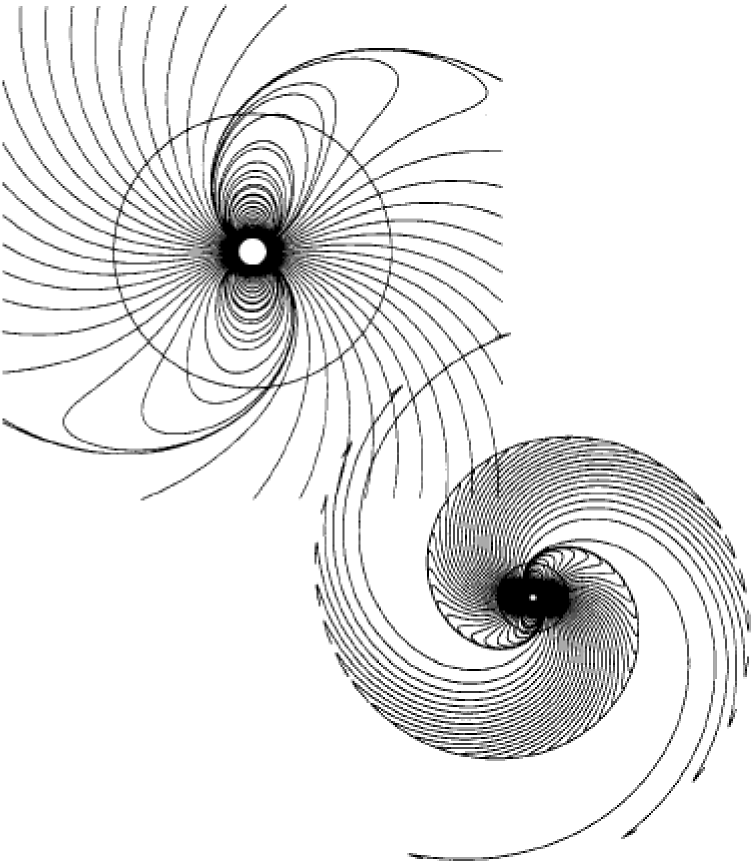

Figure 2.2: This figure shows the structure of a magnetic dipole on two different scales. The dipole is 90° inclined with respect to the rotational axis. The open magnetic field lines outside the LC are swept back and become parallel wavefronts. The circle indicates the LC. This picture is taken from Yadigaroglu (1997).

---

[3] I am using the names used in Jackson (1998b).

Here I report the formula in the form presented by Michel & Li (1999).

$$B_r = 2B_0\left\{\frac{a^3}{r^3}\cos\xi\cos\theta + \frac{h_1/\rho}{(h_1/\rho)_\alpha}\sin\xi\sin\theta e^{i\phi_s}\right\} \tag{2.2}$$

$$B_\theta = B_0\left\{\frac{a^3}{r^3}\cos\xi\sin\theta + \left[\left(\frac{\rho^2}{\rho h_2' + h_2}\right)_\alpha h_2 + \left(\frac{\rho}{h_1}\right)_\alpha\left(h_1' + \frac{h_1}{\rho}\right)\right]\sin\xi\cos\theta e^{i\phi_s}\right\} \tag{2.3}$$

$$B_\phi = B_0\left\{\left(\frac{\rho^2}{\rho h_2' + h_2}\right)_\alpha h_2\cos 2\theta + \left(\frac{\rho}{h_1}\right)_\alpha\left(h_1' + \frac{h_1}{\rho}\right)\right\}i\sin\xi e^{i\phi_s} \tag{2.4}$$

$$E_r = E_0\left\{-\frac{1}{2}\frac{a^4}{r^4}\cos\xi(3\cos 2\theta + 1) + 3\left(\frac{\rho}{\rho h_2' + h_2}\right)_\alpha\frac{h_2}{\rho}\sin\xi\sin 2\theta e^{i\phi_s}\right\} \tag{2.5}$$

$$E_\theta = E_0\left\{-\frac{a^4}{r^4}\cos\xi\sin 2\theta + \left[\left(\frac{\rho}{\rho h_2' + h_2}\right)_\alpha\left(\frac{\rho h_2' + h_2}{\rho}\right)\cos 2\theta - \frac{h_1}{(h_1)_\alpha}\right]\sin\xi e^{i\phi_s}\right\} \tag{2.6}$$

$$E_\phi = E_0\left\{\left(\frac{\rho}{\rho h_2' + h_2}\right)_\alpha\left(\frac{\rho h_2' + h_2}{\rho}\right) - \frac{h_1}{(h_1)_\alpha}\right\}i\sin\xi\cos\theta e^{i\phi_s} \tag{2.7}$$

Where (r, θ, ϕ) are the spherical coordinates, with θ the polar angle and ϕ the azimuthal angle, a is the stellar radius, ξ the angle between the magnetic axis and the rotational axis, B_0 is the strength of the magnetic field on the magnetic equator at the stellar surface, $\rho = r\omega/c$, $\alpha = a\omega/c$, $\phi_s = \phi - \omega t$, and $E_0 = \omega a B_0$. h_1, h_2 and h_1', h_2' are spherical Bessel functions of the third kind with argument ρ and their derivatives, respectively. The subscript α means that the functions enclosed are evaluated at $\rho = \alpha$. Specifically, we have

$$h_1 = \left[-\frac{1}{\rho} - \frac{i}{\rho^2}\right]e^{i\rho} \tag{2.8}$$

$$h_2 = \left[\frac{2}{\rho^2} + i\left(\frac{2}{\rho^3} - \frac{1}{\rho}\right)\right]e^{i\rho} \tag{2.9}$$

$$h_1' = \left[-\frac{3}{\rho^2} + i\left(\frac{1}{\rho} - \frac{3}{\rho^3}\right)\right]e^{i\rho} \tag{2.10}$$

$$h_2' = \left[(\frac{9}{\rho^3} - \frac{1}{\rho}) + i\left(\frac{9}{\rho^4} - \frac{4}{\rho^2}\right)\right]e^{i\rho} \tag{2.11}$$

The spin down power $\dot{\mathcal{E}}$ of this solution is

$$\dot{\mathcal{E}} = \frac{\Omega^4 a^6 B_0^2}{6c^3}\sin^2\xi \tag{2.12}$$

When we look at the aligned dipole magnetic field $\xi = 0$ we see that we return to the normal dipolar magnetic field.

$$B_r = 2B_0\frac{a^3}{r^3}\cos\theta \tag{2.13}$$

$$B_\theta = B_0 \frac{a^3}{r^3} \sin\theta \tag{2.14}$$

The induced quadrupolar electric field in this case is

$$E_r = E_0 \frac{a^4}{r^4} (-3\cos^2\theta + 1) \tag{2.15}$$

$$E_\theta = -E_0 \frac{a^4}{r^4} 2\sin\theta\cos\theta \tag{2.16}$$

2.2.2 The charge

The magnetic field structure inside a neutron star is unknown. The Deutsch solution is calculated using a uniformly magnetized sphere. However, the field for a magnetic conductive sphere tends asymptotically to a dipolar field far away from the surface (Jackson (1998b), sec. $5.9 - C - a$). Therefore different assumptions for the inner magnetic field will result in distortions from the standard dipolar field outside the star, which are more significant close to the surface.

If the star is a perfect conductor, within the star, the sum of the Lorentz force and the Coulomb force is zero. Therefore, this condition gives us the expression for the inner electric field that is induced by the rotation of the magnetic field:

$$\mathbf{E} + \mathbf{V} \times \mathbf{B} = 0 \tag{2.17}$$

Where $\mathbf{V}$ is the rotation velocity. Given an electric field, the Poisson equation tells us that there should be a charge in the center of the star. Actually, one of the effects that the magnetization vector distribution has is to change the amount and the distribution of the charge in the star that arise from the rotation. Before the rotation starts, it is commonly assumed that the neutron star is neutral. When the star rotates, the charge generated by the rotation is balanced by an opposite surface charge distribution that accounts for the discontinuity of the electric field on the surface. As we mentioned before, the magnetic field just outside the star is mainly dipolar, and this combined with the Equation (2.17) gives a quadrupolar electric field. Due to this quadrupolar electric field there is a quadrupolar surface charge superimposed to the surface charge that neutralizes the inner charge. However, this does not change the charge balance, because the surface charge integrated over the sphere's surface is zero. For an aligned dipole the quadrupolar charge is:

$$2\Omega B_0 \frac{a^3}{r^3} (1 - 3\cos^2\theta) \tag{2.18}$$

This charge offset on the surface is important because it can change the physics of the particles extracted from the neutron star surface. A detailed reference reporting all the analytical expressions for the charges is Michel & Li (1999), from paragraph 4.0 to 4.5.

2.3 The force-free magnetosphere

Goldreich & Julian (1969) showed that this vacuum solution cannot exist. The electric field induced by the rotating magnetic field is so strong that the electric force applied to a charged particle is stronger than the neutron star gravity. Therefore, the space surrounding the neutron star is populated by charged particles.

2.3.1 The corotation

Let us consider these particles extracted from the neutron star surface. If they are enough to screen the parallel electric field along the magnetic field lines, the electric field is perpendicular to the magnetic field

$$\mathbf{E} \cdot \mathbf{B} = 0 \tag{2.19}$$

which defines the ideal magnetohydrodynamic (MHD) limit (I personally suggest Bellan (2006) as a reference, however any plasma physics book deals with the MHD limit). The ideal MHD limit describes a plasma that behaves as a perfect conductor. Equation 2.19 implies that the magnetic field lines are equipotential. The electric field in the observer's frame is given by

$$\mathbf{E} + \mathbf{v} \times \mathbf{B} = 0 \tag{2.20}$$

where $\mathbf{v}$ is the fluid velocity of the plasma. Another feature of this limit is that the plasma flows "frozen" to the magnetic field lines. A direct consequence of this is that a rotating plasma in ideal MHD follows what is known as Ferraro's isorotational law (Ferraro 1937). I report a simple derivation from Cowling (1957). Substituting the Equation 2.20 into the Faraday's law, we obtain another important equation for the MHD limit, the induction equation

$$\nabla \times (\mathbf{v} \times \mathbf{B}) = \frac{\partial \mathbf{B}}{\partial t} \tag{2.21}$$

It should be stressed that velocity components parallel to the magnetic field are not contributing to the induction. Using the fact that in ideal MHD the fluid is incompressible ($\nabla \cdot \mathbf{v} = 0$) and that there are no magnetic monopoles ($\nabla \cdot \mathbf{B} = 0$) we obtain

$$\frac{\partial \mathbf{B}}{\partial t} = (\mathbf{B} \cdot \nabla)\mathbf{v} - (\mathbf{v} \cdot \nabla)\mathbf{B} \tag{2.22}$$

In a cylindrical geometry (r, ϕ, z) with $v = \Omega r$, where Ω is the local angular velocity:

$$\frac{\partial B_r}{\partial t} = -\Omega \frac{\partial B_r}{\partial \phi} \tag{2.23}$$

$$\frac{\partial B_z}{\partial t} = -\Omega \frac{\partial B_z}{\partial \phi} \tag{2.24}$$

$$\frac{\partial B_\phi}{\partial t} = r \left(B_r \frac{\partial \Omega}{\partial r} + B_z \frac{\partial \Omega}{\partial z} \right) - \Omega \frac{\partial B_\phi}{\partial \phi} \tag{2.25}$$

For the cylindrical symmetry $\partial_\phi = 0$ and for stationarity $\frac{\partial B_\phi}{\partial t} = 0$. Therefore, Equation 2.25 becomes

$$(\mathbf{B} \cdot \nabla)\Omega = 0 \tag{2.26}$$

which means that Ω is constant along the field lines, that therefore corotate at the same angular speed.

A neutron star can be considered as a rotating conductive solid magnet. Therefore, all the magnetic field line foot points rotate with the same angular velocity. This does not happen on the Sun where there is a differential angular velocity and every field line rotates with a different constant angular velocity. Therefore, we can say that the whole magnetosphere corotates with the neutron star. However, this corotation is expected to break down approaching the light cylinder.

2.3.2 Force-free electrodynamics

The magnetic energy density in the plasma is much larger than the energy density of the particles, this condition is referred to as *magnetized*

$$B^2/4\pi\rho \gg \gamma mc^2 \tag{2.27}$$

For this reason, the inertial and pressure terms are usually ignored in describing the magnetospheric plasma.
When the plasma motion becomes relativistic the displacement current term in the Ampere's law, and consequently the electric field become important. Therefore, the charge neutrality assumption assumed in non relativistic MHD fails.
Ignoring inertial and pressure term and including displacement current are proper to the *force-free electrodynamic limit*. In this limit, the sum of the forces acting on the plasma is negligible and the analogue to the Euler equation for fluid dynamics becomes:

$$\rho\mathbf{E} + \mathbf{J} \times \mathbf{B} = 0 \tag{2.28}$$

This condition with the Maxwell equations form the set of equations that govern force-free electrodynamics. This set of equations with equation 2.19 gives a characteristic current (Gruzinov 2005). Taking the vector product of Equation 2.28 with $\mathbf{B}$ we get:

$$\rho(\mathbf{E} \times \mathbf{B}) + (\mathbf{B} \cdot \mathbf{J})\mathbf{B} - (\mathbf{B} \cdot \mathbf{B})\mathbf{J} = 0 \tag{2.29}$$

$$\mathbf{J} = \frac{\rho(\mathbf{E} \times \mathbf{B})}{B^2} + \frac{(\mathbf{B} \cdot \mathbf{J})}{B^2}\mathbf{B} \tag{2.30}$$

In the Equation 2.30, we can see that the current is divided along two components. The first term along the drift velocity $\mathbf{E} \times \mathbf{B}/B^2$, the second term along $\mathbf{B}$. If we take the Faraday's and the Ampere's law and we multiply them by $\mathbf{E}$ and $\mathbf{B}$ respectively, and then we subtract them we get

$$\partial_t(\mathbf{B} \cdot \mathbf{E}) = (\nabla \times \mathbf{B}) \cdot \mathbf{B} - \mathbf{E} \cdot (\nabla \times \mathbf{E}) - \mathbf{J} \cdot \mathbf{B} \tag{2.31}$$

Using Equation 2.19, we find the form of $\mathbf{J} \cdot \mathbf{B}$. Therefore, the characteristic current has the form

$$\mathbf{J} = \frac{\rho(\mathbf{E} \times \mathbf{B})}{B^2} + \frac{(\nabla \times \mathbf{B}) \cdot \mathbf{B} - \mathbf{E} \cdot (\nabla \times \mathbf{E})}{B^2}\mathbf{B} \tag{2.32}$$

The factor multiplying $\mathbf{B}$ in the second term is constant along the magnetic field lines (λ, Gruzinov (2006); Bai & Spitkovsky (2010)). Goldreich & Julian (1969) indicated another interesting property for this corotating magnetosphere. If we apply the divergence operator on the electric field of Equation 2.20 we get a characteristic charge density

$$\rho_{GJ} = \frac{\nabla \cdot \mathbf{E}}{4\pi c} = -\frac{\Omega \cdot \mathbf{B}}{2\pi c} + \frac{(\Omega \times \mathbf{R}) \cdot (\nabla \times \mathbf{B})}{4\pi c} \tag{2.33}$$

known as Goldreich-Julian charge density. Therefore, in this relativistic system the plasma is charged. It is interesting to notice that the whole magnetosphere is globally negatively charged. In fact, the force-free magnetosphere is a conductive natural extension of the negative offset surface charge present in the vacuum case that we described in Section 2.2.

2.3.3 The force-free magnetosphere structure

Goldreich & Julian (1969) described this rotating magnetosphere with the open field lines transporting electromagnetic Poynting flux outward. As the review of Michel (1982) described, the Poynting flux of such an object should differ only by a small factor from the spin down of a rotating magnetic dipole. As it was described for the aligned case, the corotating current (the first term from Equation 2.32) opens more magnetic field lines, therefore the Poynting flux should increase with respect to the one of the Deutsch solution (in the previous Section 2.2). The determination of this factor relies on numerical simulations (Gruzinov 2005). An increase of the pulsar spin down is observed in the inclined case (Spitkovsky 2006)

$$L \sim \frac{\mu^2 \Omega^4}{c^3}(1 + \sin^2 \alpha) \tag{2.34}$$

Where μ is the magnetic moment and α the angle between the magnetic pole and the axis of rotation. The motivation for this increase is not yet clear (Tchekhovskoy et al. 2016). In Figure 2.3, we show the magnetic field structure of an inclined rotators in the force-free limit.

Lyubarskii (1990) pointed out another feature of the magnetosphere structure. The currents that flow along the last open field lines should merge outside the light cylinder on the equatorial plane forming a charged current sheet where magnetic field lines of opposite polarity reconnect. However, the force-free limit inside this region is not going to be respected because of the conversion of the magnetic energy into particle kinetic energy. In astrophysics, the characteristic scale of the magnetic field is larger compared to the scale where the electric plasma resistivity happens, therefore, we can usually consider the plasma as an ideal conductor (e.g. Bellan (2006); Cowling (1957)). This is why the MHD limit works so well for astrophysics. However, reconnection is generated by the magnetic field topology and therefore the regions where it happens are comparable to the scale of the magnetic field itself. This is why magnetic reconnection is an important dissipative process in astrophysics (Kagan et al. 2015).

A numerical solution for the aligned rotator was first found by Contopoulos et al. (1999), while for the inclined rotator by Spitkovsky (2006). The two solutions are showed in Figure 2.4. For an in depth analysis of the force-free solution in the aligned case we refer to Timokhin (2006).

2.3.4 The dissipative models

The pulsar magnetosphere cannot be in the ideal force-free limit, because we observe non thermal radiation. Non thermal radiation comes from accelerated particles, therefore, a net force acting on them must be present. In order to have this force, regions of dissipation can be inserted in the magnetosphere. Different more or less physically motivated attempts had been made, because the form of the physical dissipation is not clear. However, some dissipative models (Kalapotharakos et al. 2014; Brambilla et al. 2015) had been particularly successful in reproducing the pulsar γ-ray phenomenology.

2.4 Plasma supply and pair production

In this section, we briefly review some important steps about how the magnetosphere could be filled with particles and therefore, approach the force-free limit. The particles could be extracted from the surface or produced in electron positron pair cascades by energetic photons.

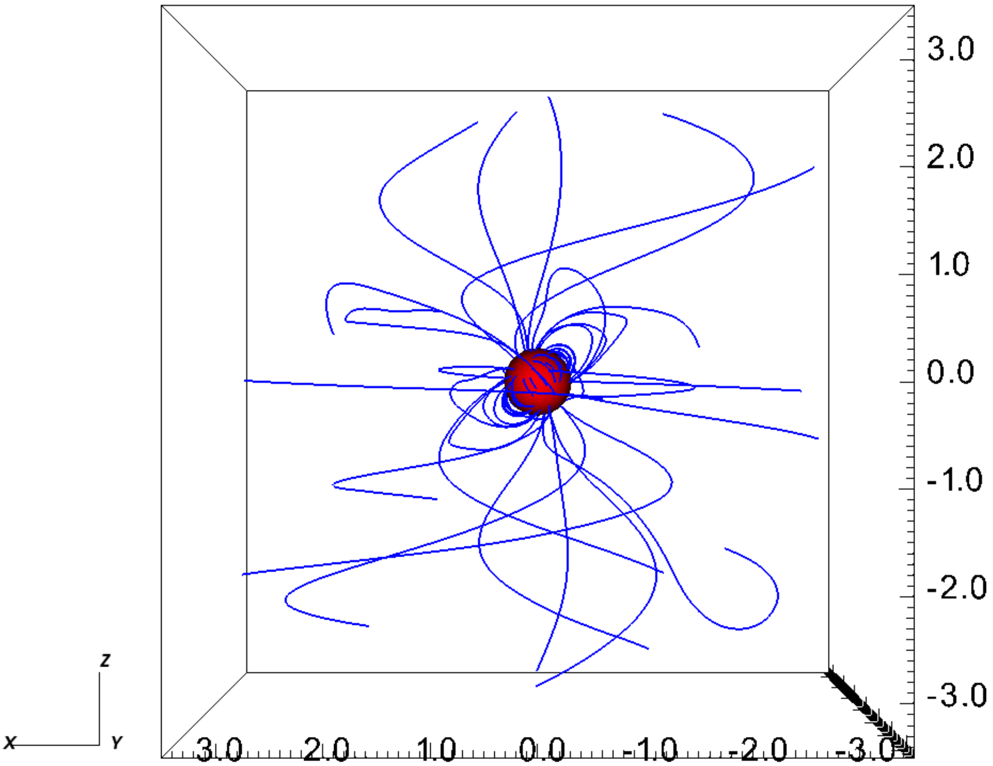
3.0
2.0
1.0
0.0
-1.0
-2.0
-3.0
Z
X
Y
3.0
2.0
1.0
0.0
-1.0
-2.0
-3.0

Figure 2.3: In this Figure there are shown the open and closed magnetic field lines for the force-free magnetosphere of a 45° inclined rotator. The axes are in $R_{\rm LC}$ units. This picture has been obtained using the software VisIt (Childs et al. 2012).

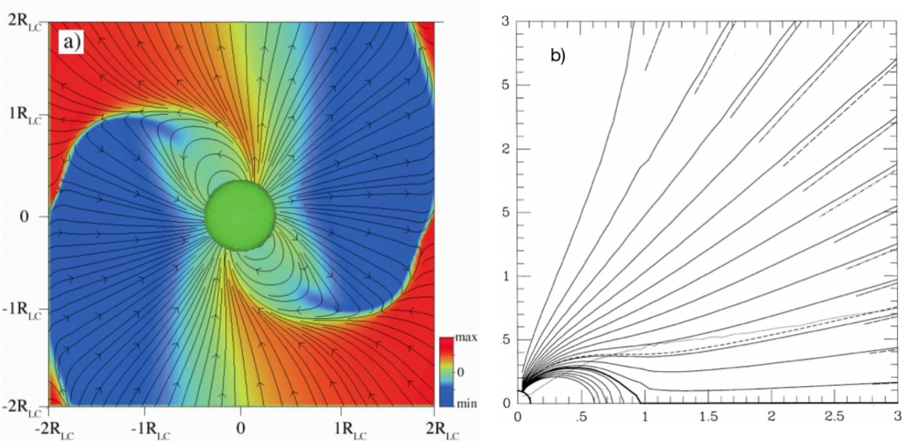

Figure 2.4: This figure shows the magnetic field lines of the first force-free solutions of the pulsar magnetosphere. a) is from Spitkovsky (2006), and it is for a 60° inclined rotator. The color scale represents the in plane component of the magnetic field. b) is the aligned rotator solution from Contopoulos et al. (1999). The dashed-dotted lines on the outer edge represent the asymptotic solution, the region between the dashed line and the thick line represents the current region that flows in the opposite direction of the one flowing from the polar cap. The dotted line is the null line, where the charge density changes sign.

2.4.1 The electrosphere

In order to approach the force-free limit satisfying Equation 2.19, particles should be enough to screen the electric field parallel to the magnetic field lines. Goldreich & Julian (1969) thought these particles would be extracted from the star surface, electrons and ions with respect to the sign of the charge needed. This setup has been researched with simulations (Krause-Polstorff & Michel 1985; Spitkovsky & Arons 2002) and it was found that it gives origin to an electrosphere. The electrosphere, is a solution in which particles of only one sign screen the accelerating electric fields at the surface. The particles with different sign of charge are organized in a disk and a dome, see Figure 2.5. However, accelerating electric fields are still present far from the surface, therefore it is not a force-free solution. The non neutral plasma outside the star is subject to the Diocotron instability, a typical instability of non-neutral plasmas (e.g. Bellan (2006)). This allows particles to fill a larger volume but still not the entire magnetosphere (Pétri 2009).

2.4.2 Polar cap pair production

This picture with particles extracted only from the surface is not complete. Sturrock (1971) showed that electrons accelerated from the polar caps could emit γ-rays that undergo pair production. This picture became more solid during the years. Primary electrons would accelerate and emit γ-rays by curvature radiation or energize photons by inverse Compton. These γ-rays would produce pairs (called secondaries) by magnetic pair production, a quantum-electrodynamic (QED) process possible because of the high magnetic fields (Harding & Lai 2006). The pairs screen the electric field and limit the accelerating voltage, but pairs could still be produced after these fronts (Harding & Mus-

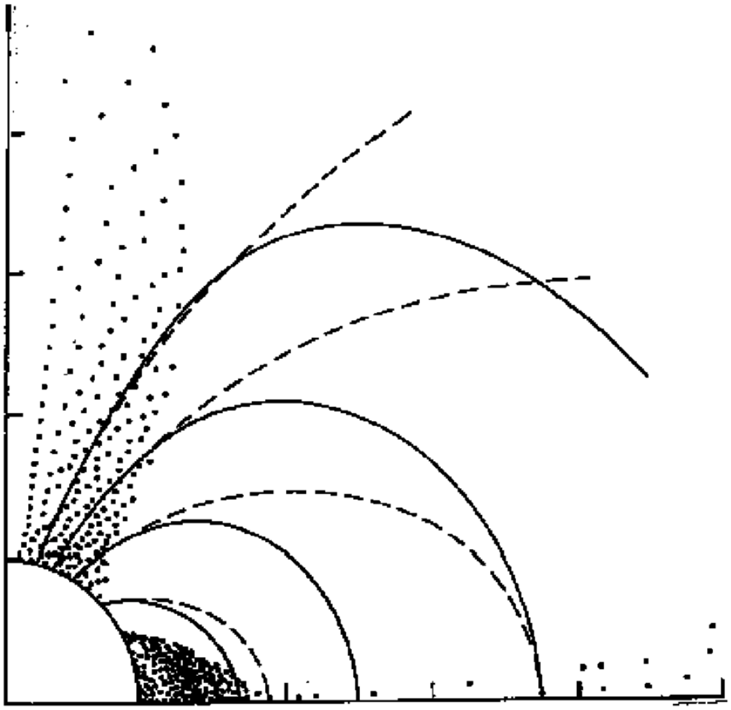

Figure 2.5: Electrosphere solution from Krause-Polstorff & Michel (1985). The dashed lines are the magnetic field lines, the solid lines are equipotential lines, the dots are the particles.

limov 1998, 2001, 2002). The pairs are produced in cascades with large pitch angles and radiate synchrotron photons γ-rays that undergo to pair production again. These kind of studies worked fixing the external voltage the the particles had to screen. Beloborodov (2008) presented an analytical study in which the quantity fixed was the current density $\mathbf{J}$ and not the voltage. The current chosen is the one from the force-free solution. This description looks more realistic, because the local current is set by the global structure of the magnetosphere and not by the local pair production process. The suggestion from this study is that the key parameter for the pair production is $\alpha = J_{cf}/\rho_{GJ}c$, where J_{cf} is the current in the corotating frame, while ρ_{GJ} is the Goldreich-Julian charge density (Equation 2.33). If $\alpha^{-1} < 1$ (either $\alpha < 0$ or $\alpha > 1$) the pair production happens. Timokhin & Arons (2013) simulated it discovering that the process is time-dependent on the μs time scale. Timokhin & Harding (2015) merged the previous model with the numerical Monte Carlo simulation of the pair cascade. They found that the maximum number of pairs produced per primary particle extracted is $\sim 10^5$.

2.4.3 Pair production in other regions of the magnetosphere

The pair production on the polar cap is widely accepted. However, there are other sites in the pulsar magnetosphere where the pair production could happen. One of these is the pulsar Y-point and the current sheet. The Y-point is where the last open field lines merge and the current sheet starts. The pair production in the current sheet was first mentioned by Lyubarskii (1996). In this site, the fields are lower than close to the surface, therefore, magnetic one-photon pair production does not occur. There are two ways in which the pair production can happen. One is through the photons produced locally in the current sheet, the other is triggered by the photons coming from another region of the star, as it was proposed for the outer gap (Chiang & Romani 1994). The outer gap (Cheng et al. 1976) is another site where the pair production can happen. It is a region with not enough particles to maintain Equation 2.19 and where the charge density changes sign. In this region, the particles would be accelerated, emit high energy photons that would trigger the pair production. The outer gap was originally thought of as a vacuum magnetic field, however, similar structures could be present even in a near force-free magnetosphere. In general a region in which Equation 2.19 is not satisfied is referred to as a gap, because there is a lack of particles, and there particles are accelerated. However, all the sites included in this subsection have not been investigated in as much depth as the polar cap, therefore, leaving more work to be done.

2.5 Estimating the conditions of the plasma in the pulsar magnetosphere

Since the seminal work of Goldreich & Julian (1969), it has been known that a pulsar should have a magnetosphere. In this chapter I want to show what are the expected conditions of the magnetospheric plasma with some simple calculations. I will consider the magnetosphere for a young pulsar.

2.5.1 The conditions of the plasma

Most of the pulsars spin down as rotating magnetic dipoles. If we measure their period and period derivative, we can estimate the intensity of the magnetic field on their surface (Equation 1.1), that is usually around 10^{12}G for not recycled pulsars. Let us assume the pulsar period is 0.1 s. According to Goldreich & Julian (1969), the charge density in a force-free (FF, see the previous section 2.3) magnetosphere can be approximated as

$$\rho_{GJ} \sim -\frac{\Omega B}{2\pi c} \tag{2.35}$$

considering that the axis of rotation and the magnetic field are aligned. Here B is the magnetic field, Ω is the inverse of the period multiplied by 2π and c is the speed of light. If we consider this expression to evaluate the charge density on the pulsar surface we obtain a charge density of 333.3 $\mathrm{statC/cm^3}$. This charge flows away from the surface at c; this assumes that the charge is of the sign to be accelerated by the E field above the surface, however this is not always true for the global force-free magnetosphere. If we consider the charge density as composed by electrons and positrons, we obtain a flux at the surface of $2.2 \cdot 10^{22}$ $\mathrm{part/scm^2}$.

How does this flux scale with the distance? Up to $1.0\ R_{\mathrm{LC}}$, we assume the plasma flow to be proportional to Eq.(2.35) times c and so it scales as r^{-3} because the plasma flows following the magnetic field lines[4]. Outside of 1.0 R_{LC} it scales as r^{-2}, like a flux without sources in a spherical geometry moving radially outward at constant velocity c

$$n(R) = \frac{N}{4\pi R^2 dR} \tag{2.36}$$

Where $n(R)$ is the density with respect to the radius R, N is the total number of particles flowing out in a shell dR thick. The flux is $n(R)c$.

The plasma radiation undergoes attenuation by the pair production processes in zones relatively close to the surface. The particles that are extracted from the surface are called primaries, instead the ones that are pair produced are called the secondaries. The pair creation process has both theoretical and observational proofs (Sturrock 1971; de Jager et al. 1996). We estimate the multiplicity of the plasma, that is the actual number of particles divided by the number of the primaries, to be 10^5 from the results of Timokhin & Harding (2015). Always following Timokhin & Harding (2015), the primaries are supposed to have $\gamma = 10^7$ because of pair production opacity.

With these assumptions, we can estimate the particle density along the radial direction. In the rest of this thesis, we will see that the particle distribution does not change only with respect to the radial distance, but for these first estimates we will ignore it.

Once we know these density profiles, we will be able to estimate some parameters describing the plasma: the magnetization (σ) that is the ratio of the magnetic energy density to the particle energy density, the temperature below which the plasma becomes collisional, the multiplicity that is the ratio between the minimum number of charges to obtain the Goldreich Julian charge density and the actual number of particles, the gyro frequency (ω_B) and the annihilation rate between electrons and positrons. Now I will outline how these quantities can be calculated.

---

[4] The magnetic field of a rotating dipole scales as r^{-3} inside the LC (static region), and as r^{-1} outside of it (radiative region). See Jackson (1998b).

2.5.2 Definition of important quantities

We define magnetization[5] as

$$\sigma = \frac{B^2}{8\pi n m c^2 \gamma} \tag{2.37}$$

Where B is the local magnetic field, n is the particle density, m is the particle mass and in the pulsar magnetosphere we think there are electrons and positrons, c is the speed of light and γ is the Lorentz factor. The magnetization indicates the ratio of magnetic energy to particle energy density. In the pair creation process the energy is conserved therefore the quantity $\Sigma_i \gamma_i$, where the index i is one for each particle, remains constant before and after the pairs are produced, causing the presence of more particles but with a smaller Lorentz factor. This quantity is important because it tells us that the motion of the plasma is controlled by the fields. When $\sigma >> 1$ the plasma is called magnetized, because the magnetic energy is larger than the particle energy density. In the opposite limit with $\sigma << 1$ the particle energy density dominates the field energy.

We will see that in the force-free limit particles are flowing along the magnetic field lines at ultra relativistic speed; so we think that in a real pulsar the motion perpendicular to the magnetic field lines is much less significant than the one parallel to the magnetic field lines. However, we want to evaluate whether this plasma could be collisional in the perpendicular direction. In the parallel direction the γ are high and the particle distribution is not thermal but given by the accelerating fields, this suggests that the collisions are not important along this direction.

In general plasma becomes collisional through Coulomb collisions when it is cold (e.g. Boyd & Sanderson (2003)). The collisions behave differently than collisions in normal gas because the Coulomb cross section decreases when the temperature increases (e.g. Somov (2012)). The formula for the collisional time scale is:

$$\tau_{coul} = \frac{(k_B T)^{\frac{3}{2}} (4\pi)^2 \sqrt{m}}{n e^4} \tag{2.38}$$

where k_B is the Boltzmann constant. Other collisions that we need to evaluate are the electron-positron annihilation events. The cross section for these collisions in a relativistic environment is given by the Klein-Nishina cross section (e.g. Jackson (1998b)), but for our evaluation we will use the Thompson cross section ($\sigma_{Thompson}$) for the sake of simplicity.

$$\tau_{ann} = 1/nc\sigma_{Thompson} \tag{2.39}$$

These quantities have to be compared with the gyro time scale: if the gyro timescale is larger than the collisional time scale, the collisions are important. The gyro frequency formula is:

$$\omega_B = \frac{eB}{m\gamma c} \tag{2.40}$$

The higher the γ, the lower the frequency, so the larger the time scale is. Therefore we want to check the gyro frequency for the highest γ, because it will give the most stringent condition for the importance of the collisions.

We carry out these calculation in Table 2.1 and find that collisions are not important.

---

[5] Usually magnetization is not defined in this way but with $\sigma = B^2/8\pi n m c^2$ because it is used in the comoving frame to describe the plasma in the relativistic MHD approximation. However, we are interested in the inertial frame and in our simulation $B > E$ in all the regions except for the current sheet, as we will see later.

2.5.3 Conclusions

In the Table 2.1 we report the results of these estimates. The minimum gyro frequency is calculated for photons with the γ of the primaries, the maximum instead for particles at rest. In reality these estimates are very coarse. First because the multiplicity$\gg 1$ and it implies that only few particles have $\gamma = 10^7$. Moreover as we said before, the plasma is anisotropic, because the main motion is along the magnetic field lines. For the gyro radius what counts is the momentum perpendicular to the magnetic field lines, but there are no hints except that $p_{||} \gg p_\perp$, that is why we considered the γ of $p_{||}$ for the calculation.
The magnetization is high everywhere and after $1.0 R_{\rm LC}$ it remains constant, because the magnetic energy density and the flux decrease with the same power law in the radiative zone. This is expected and it is the first part of a bigger problem called the $\sigma-$problem, because observations tell us that far away from the pulsar the magnetization drops (Kennel & Coroniti 1984).
From the Table 2.1, we can see that the plasma should be magnetized everywhere in the magnetosphere. Moreover it should be collisionless: Thompson collisions are rare because of the low densities, and the temperature at which Coulomb collisions could become important is very low. Therefore we expect that the plasma in the pulsar magnetosphere to be a relativistic, magnetized and collisionless pair plasma.

Table 2.1: Plasma estimated conditions in the radial direction.

Distance (R_{LC})	**Particle density (#/cm3)**	**Minimum Gyro Frequency (Hz)**	**Maximum Gyro Frequency (Hz)**	**Magnetization**	**Thompson Collisions Frequency (Hz)**	**Coulomb Collisions Temperature (K)**
0.2	$7.7 \cdot 10^{9}$	$1.9 \cdot 10^{6}$	$1.9 \cdot 10^{13}$	$1.5 \cdot 10^{4}$	$1.4 \cdot 10^{-3}$	$4.9 \cdot 10^{3}$
0.5	$4.9 \cdot 10^{8}$	$1.2 \cdot 10^{5}$	$1.2 \cdot 10^{12}$	$9.7 \cdot 10^{2}$	$8.8 \cdot 10^{-5}$	$4.9 \cdot 10^{3}$
1.0	$1.2 \cdot 10^{8}$	$1.5 \cdot 10^{4}$	$1.5 \cdot 10^{11}$	60.9	$2.2 \cdot 10^{-5}$	$7.0 \cdot 10^{3}$
2.0	$3.1 \cdot 10^{7}$	$7.7 \cdot 10^{3}$	$7.7 \cdot 10^{10}$	60.9	$5.5 \cdot 10^{-6}$	$4.9 \cdot 10^{3}$
5.0	$4.9 \cdot 10^{6}$	$3.1 \cdot 10^{3}$	$3.1 \cdot 10^{10}$	60.9	$8.8 \cdot 10^{-7}$	$3.1 \cdot 10^{3}$
50.0	$4.9 \cdot 10^{4}$	$3.1 \cdot 10^{2}$	$3.1 \cdot 10^{9}$	60.9	$8.8 \cdot 10^{-9}$	$9.8 \cdot 10^{2}$
500.0	$4.9 \cdot 10^{2}$	30.6	$3.1 \cdot 10^{8}$	60.9	$8.8 \cdot 10^{-11}$	$3.1 \cdot 10^{2}$
1000.0	$1.2 \cdot 10^{2}$	15.3	$1.5 \cdot 10^{8}$	60.9	$2.2 \cdot 10^{-11}$	$2.2 \cdot 10^{2}$

CHAPTER 3

A PIC code for the pulsar magnetosphere

In chapter 2, we discussed the theory of plasma physics of the global pulsar magnetosphere. Furthermore we gave a detailed picture of the magnetosphere using the force free electrodynamics limit and discussed the departure of the magnetosphere from this limit. We will use Particle In Cell (PIC) codes as a tool to study the non-idealities of the magnetosphere.

3.1 Introduction and PIC code basics

Let us begin by considering the Vlasov equations for plasma physics (see for example Bellan (2006)). In the Vlasov description the space where the equations should be integrated is not 3D like in a code to simulate plasma in the MHD limit, but it is 6D because the equations work with the distribution function that is defined on the phase space (3 spatial dimensions and 3 correspondent velocity dimensions). Calculations on a 6D domain would take a lot of time, but there are ways to avoid this problem[1].
Between the 1950's and 1970's the Particle In Cell (PIC) approach was developed by J.Dawson, O. Buneman, B. Langdon and C. Birdsall which reduced the time to perform these calculations. The book *Plasma Physics via Computer Simulation* by Birdsall & Langdon (1991) is still one of the main references for the field.

3.1.1 Scheme for a PIC code

A typical plasma problem has an electromagnetic part and a particle dynamics part that interact together, and a PIC code describes this interaction cyclically. How? A generic fluid can be thought of either as many single molecules moving according to the physical laws and the interaction between them, or as a continuum in which certain physical properties are defined locally. In a PIC code the plasma is discretized in elements that represents samples of the species composing the plasma itself, therefore this approach places itself in between these two descriptions. These elements are called macro particles or super particles.
As it is shown in Figure 3.1, what happens in a PIC code is the following:

- We predict the motion of the macro particles according to the forces that move them for a short time step Δt (In Figure 3.1 the top rectangle).
- This motion has an effect on the fields that is mediated through either the charge density or the current density (In Figure 3.1 the right rectangle). The fields and the

---

[1] However gyrokinetic codes integrate on a 5D space and they are commonly used in research

charge or the current density are defined on a discrete grid, and not in a $\mathbb{R}^3$ space like the particle positions and velocities, so there is need of a weighting operation.

- The fields are evolved for the same time step Δt according to some of the Maxwell equations, electrostatic codes use the Poisson equation, electromagnetic codes use Faraday's and Ampere's laws (in Figure 3.1 the bottom rectangle).
- Once the new fields are calculated, they should be somehow interpolated from the discrete grid to the exact particle position, where the acting force is calculated (In Figure 3.1 the left rectangle). Then the scheme returns to the first step.

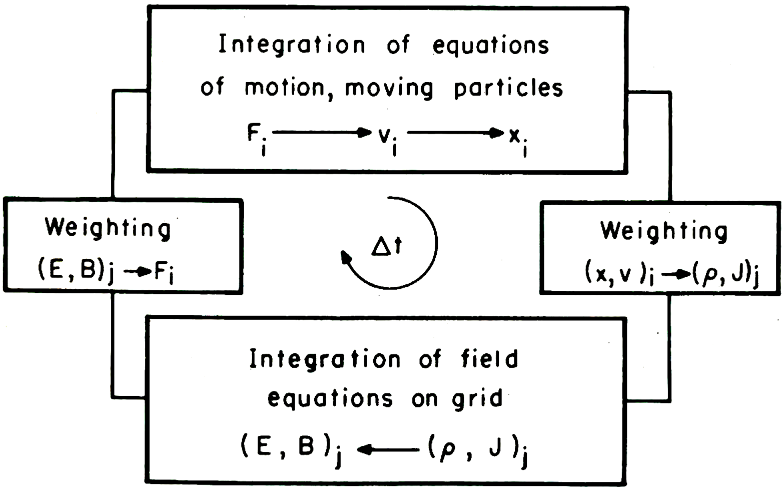
Integration of equations
of motion, moving particles
$F_i \rightarrow v_i \rightarrow x_i$
Weighting
$(E,B)_j \rightarrow F_i$
Δt
Weighting
$(x,v)_i \rightarrow (\rho,J)_j$
Integration of field
equations on grid
$(E,B)_j \leftarrow (\rho,J)_j$

Figure 3.1: The scheme of a PIC code. The figure is taken from Birdsall & Langdon (1991).

I did not mention any plasma limit such as ideal MHD; this is because PIC codes do not need to enforce any physical condition in the plasma description, and the equations are the basic Maxwell equations. For this reason they are often referred to as self consistent methods. This is the reason why it is interesting to use them to study the breaking of the force free limit in the pulsar magnetosphere, however, they have numerical limitations (not representing collisions well and resolution related artifacts), like every technique to simulate physics, which I will explore later.

3.1.2 Particles

The particles are not modeled as a point charge, but their charge is distributed over a finite volume. The shape of this volume can vary, and it determines the discretization of the fluid into single macro particles. In Figure 3.2 we show the 1D particle shape functions with the lowest order over a cell. The higher the order, the more the charge of the particle is distributed over many cells, and then the better the discretization will be. However, the computational cost will increase using higher order shape functions, therefore a balance is needed. Squared shape functions (1^{st} order) or triangular shape functions (2^{nd} order) are the most commonly used. It is important to use the same shape function when we calculate the charge or current density from the particles (the box on the right in Figure 3.1), and when we interpolate the fields on the grid to the particle

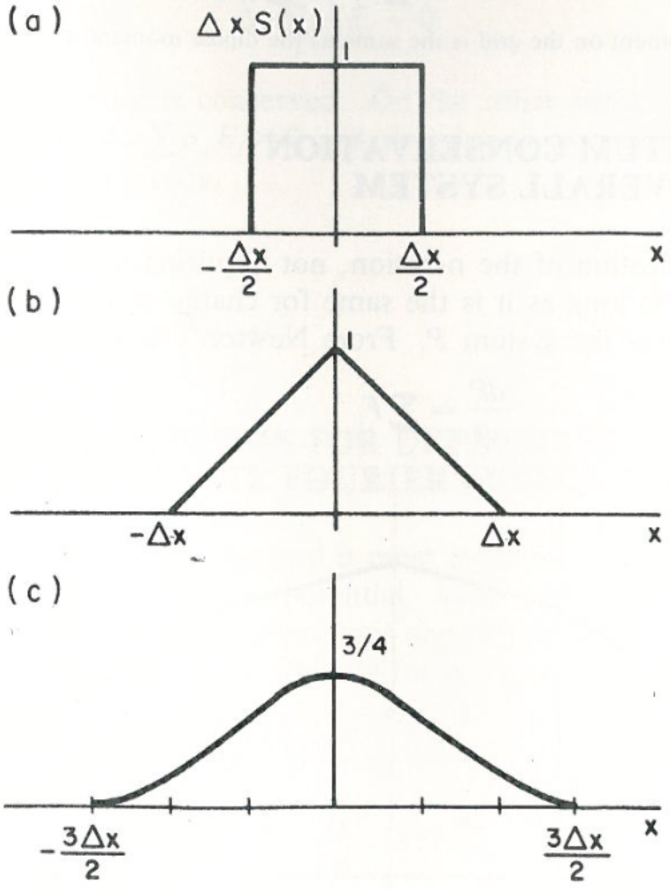
(a)
Δ x S(x)
1
$-\frac{\Delta x}{2}$
$\frac{\Delta x}{2}$
x
(b)
1
$-\Delta x$
Δx
x
(c)
3/4
$-\frac{3\Delta x}{2}$
$\frac{3\Delta x}{2}$
x

Figure 3.2: First orders of the particle shape function. Figure taken from Birdsall & Langdon (1991).

position (the box on the left in Figure 3.1), because this has important implications in the conservation of momentum. The total momentum of the system P changes according to the sum of the forces acting F_i on our system

$$\frac{dP}{dt} = \sum_i F_i \tag{3.1}$$

If we rewrite the forces (limiting ourselves only to the electric field for simplicity) we can rewrite the previous equation interpolating the fields on the particle positions

$$\frac{dP}{dt} = \sum_i^{N_p} q_i \Delta x \sum_j^{N_c} E_j S(X_j - x_i) \tag{3.2}$$

Where q_i are the charges of the macro particles, Δx is the field grid spacing, E_j is the electric field components on the different cells and $S(X_j - x_i)$ is the particle shape function with which we interpolate the field at the position x_i using electric field components at the positions X_j, N_p is the total number of macroparticles in the simulation and N_c the number of the grid cells in the domain.

If we use the same shape function for the two weighing operations in the PIC cycle, we can write:

$$\frac{dP}{dt} = \Delta x \sum_j E_j \sum_i q_i S(X_j - x_i) \tag{3.3}$$

and see that we obtain the momentum equations using only quantities defined on the field grid

$$\frac{dP}{dt} = \Delta x \sum_j E_j \rho_j \tag{3.4}$$

where ρ_j is the charge density defined on the grid. Therefore the two weighting procedures are equivalent only if they use the same shape function. This property is usually referred to as *zero self-force* because if we use two different shape functions there is an artificial force acting on the particle at every cycle and so the total momentum is no longer conserved. However, this *zero self force* condition is rooted in a more profound scenario. PIC belongs to the category of the so called "particle-mesh" techniques (opposed to "particle-particle" techniques). Particle-mesh codes in general do not capture accurately short range forces, but they are accurate for long range forces[2]. In a plasma, collective phenomena cause long range forces, while Coulomb collisions are the most common short range forces. For this reason, PIC codes are used mainly to simulate collisionless plasma. A simpler aspect of this problem can be found in the notes of Lapenta (checked on: 2017-03-03); `https://perswww.kuleuven.be/~u0052182/weather/pic.pdf`. When two particles of a PIC code are approaching each other, at a long distance the force is the exact one. The problem arises at a short distance when the two macro particles of opposite sign overlap, and therefore neutralize the charge in the overlapping region (Figure 3.3). This causes the short range interactions to be weaker, as it is shown in Figure 3.4. As we just saw, the shape function should be the same for the two weighing procedures. However, the shape of the super particle has important effects on the simulation by itself: the higher the order of the shape function, the less noisy the particle is. This is due to the interaction of the grid with the particle. If the

---

[2] If the reader is interested in a complete exposition of this problem I suggest the reading of Hockney & Eastwood (1981).

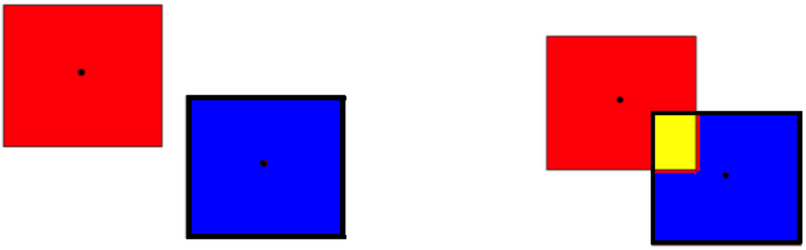

Figure 3.3: At long distances particles do not overlap, at short distances part of their charge could be neutralized if the other particle has opposite sign. Figure taken from Lapenta (checked on: 2017-03-03).

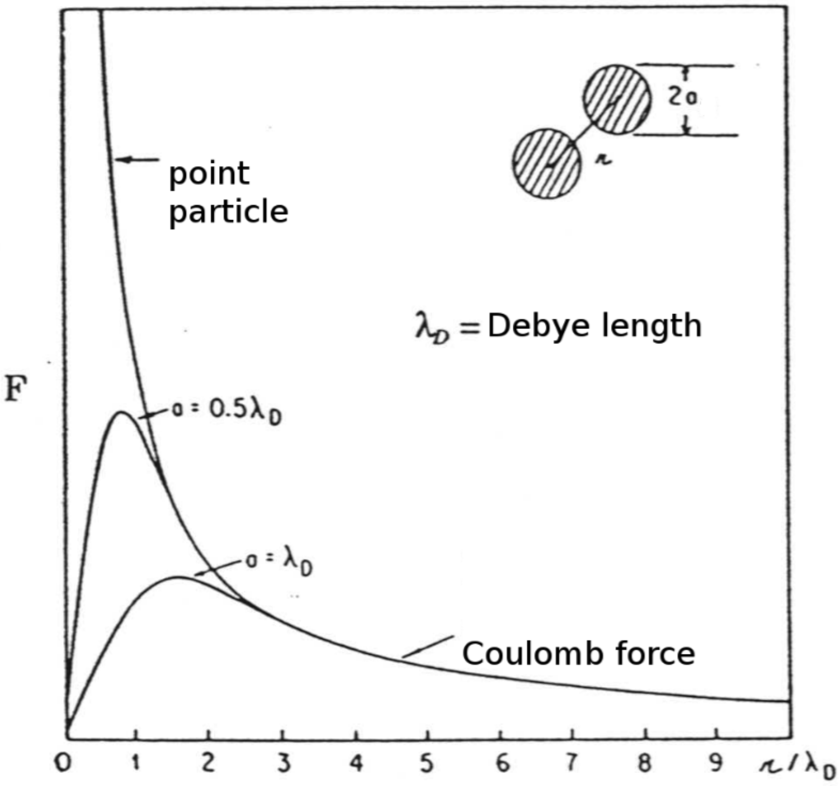

Figure 3.4: In this figure the force between two macro particles (F - y axes) is plot against their distance (r - x axis). The three curves represent a point particle, a particle with radius a of a half the Debye length (λ_D) and another with a radius of one λ_D. As you can see the force changes at small distances, but it does not at larger distances. All the lengths are expressed in λ_D units. Figure taken from Lapenta (checked on: 2017-03-03).

shape function has a lower order (as shape (a) in Figure 3.2) the input that this particle gives to the grid can be described with a Fourier series that is truncated earlier than the one for a particle with higher order shape function. These missing terms in the Fourier series generate aliases on the grid introducing noise in the simulation. The two ways to decrease this noise are either to use high order shape functions or to increase the number of macro particles per charge unit.

3.1.3 The particle pusher

The algorithm commonly used for particle dynamics is called the *leap-frog method*. The two first-order differential equations to be integrated separately for each particle are:

$$m\frac{d\mathbf{v}}{dt} = \mathbf{F} \tag{3.5}$$

$$\frac{d\mathbf{x}}{dt} = \mathbf{v} \tag{3.6}$$

where $\mathbf{F}$ is the force, $\mathbf{v}$ the velocity, m the mass, $\mathbf{x}$ the space coordinate and t the time coordinate. These equations are replaced by the *finite-difference equations*

$$m\frac{\mathbf{v_{new}} - \mathbf{v_{old}}}{\Delta t} = \mathbf{F_{old}} \tag{3.7}$$

$$\frac{\mathbf{x_{new}} - \mathbf{x_{old}}}{\Delta t} = \mathbf{v_{new}} \tag{3.8}$$

This scheme is preferred over higher order schemes because it uses less memory and it is faster. In the Figure 3.5 the *time centering* of the method is shown: $\mathbf{v}$ is $\Delta t/2$ shifted with respect to $\mathbf{F}$ and $\mathbf{x}$. For this reason, care should be taken in calculating initial conditions and the particle energetics. Another issue for the leap frog method is how to represent the gyromotion. The most commonly used solution is the one presented for the first

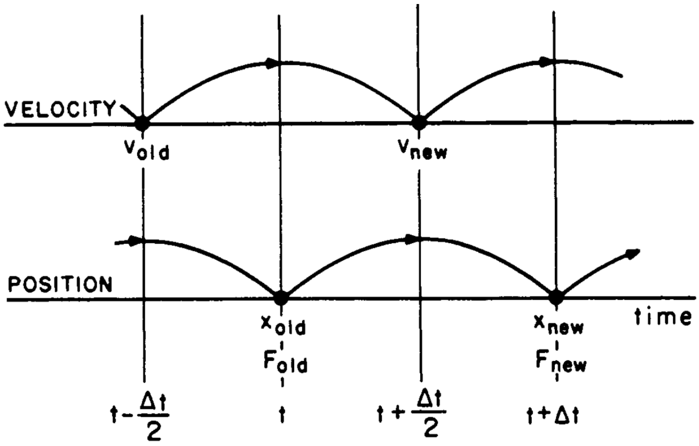

Figure 3.5: Time centering of $\mathbf{F}$, $\mathbf{v}$ and $\mathbf{x}$ in a *leap-frog* scheme. Figure taken from Birdsall & Langdon (1991).

time by Boris (1970). The physical motivation of this method relies in the physics of the electromagnetic force $\mathbf{F}_{EM}$ acting on a particle

$$\mathbf{F}_{EM} = \mathbf{F}_{electric} + \mathbf{F}_{magnetic} = q\mathbf{E} + q(\mathbf{v} \times \mathbf{B}) \tag{3.9}$$

The electric force $\mathbf{F}_{electric}$ changes the magnitude of the velocity of the particle. The magnetic force $\mathbf{F}_{magnetic}$ instead changes only the direction of the particle velocity, not the magnitude. Therefore Boris divided his scheme in this way

$$\textit{half-acceleration}(\mathbf{F}_{electric}) \Rightarrow \textit{rotation}(\mathbf{F}_{magnetic}) \Rightarrow \textit{half-acceleration}(\mathbf{F}_{electric}) \tag{3.10}$$

where the velocity that is rotated is an average of the velocity between the half steps. This scheme permits to avoid numerical instabilities related to the gyro motion even without resolving the motion itself (Birdsall & Langdon 1991). When electric fields are transformed from one inertial frame to another using the Lorentz transformation, part of the electric field transforms into magnetic field and vice versa. The force exerted on particles from the electric field cancels with part of the force exerted by the magnetic field, so that the motion of the particles is identical in both frames. For PIC calculations involving relativistic species, it implies eventually that the particle pusher preserves the property of electric field and magnetic field cancellation in the Lorentz force term, either exactly or to such degree that the associated errors can be neglected (Vay 2008). However, if the Boris scheme is extrapolated to relativistic speed ($\mathbf{v} \rightarrow \gamma\mathbf{v}$) it does not preserve this property and may thus lead to large errors when calculating the orbits of relativistic species. Vay (2008) found that using $\mathbf{v}$ instead of $\gamma\mathbf{v}$ in the rotation resolved these problems. We implemented this pusher in our code.

3.1.4 General PIC restrictions

The scheme that was just outlined is known as FDTD (Finite Difference Time Domain) explicit PIC. There are two fundamental scales in a plasma, the plasma frequency ω_p (the highest frequency in a plasma) and the Debye length λ_D (the skin depth λ_{sd} if the plasma is relativistic) (Bellan 2006).

As was shown in chapter 4 of Birdsall & Langdon (1991), if we want to simulate an harmonic oscillator with a leapfrog scheme pusher we need to have $\omega_0 \Delta t < 2.0$, where ω_0 is the frequency of the oscillator, otherwise the oscillation will grow unstable. The Langmuir waves are the oscillations happening at ω_p and their mechanism behaves as a harmonic oscillator. Therefore $\omega_p \Delta t < 2.0$ allows the PIC simulation to remain stable.

Resolving the ω_p does not automatically resolve the Debye length/skin depth. When this length is not resolved, numerical heating warms up the plasma until this physical length becomes resolved in the grid[3].

The so-called implicit PIC (Brackbill & Forslund 1982) codes eliminate these limitations in exchange for a much larger computational cost. In this case, one does not need to have a time step that resolves the frequencies in the system, because the solver is advanced iteratively. However, the iteration costs much more computer time Birdsall & Langdon (1991).

---

[3] Birdsall & Langdon (1991) gives a complete description of the Debye shielding in a FDTD PIC in chapter 12.

3.1.5 Electromagnetic PIC codes

Electromagnetic PIC codes use the Faraday's law and the Ampere's law to describe the evolution of the system

$$\nabla \times \mathbf{E} = -\frac{1}{c}\frac{\partial \mathbf{B}}{\partial t} \tag{3.11}$$

$$\nabla \times \mathbf{B} = \frac{1}{c}\frac{\partial \mathbf{E}}{\partial t} + \frac{4\pi}{c}\mathbf{J} \tag{3.12}$$

and the current density J becomes the source for the Maxwell equations and not the charge density ρ.

3.1.6 Dispersion relation and Courant condition

In reality the dispersion relation of electromagnetic waves in vacuum is ($c = 1$):

$$\omega^2 = k^2 \tag{3.13}$$

In all the schemes there is a modified dispersion relation for waves because of their description on the grid. If we look at their dispersion relation (Birdsall & Langdon 1991) it has the form:

$$\sin^2\left(\frac{\omega\Delta t}{2}\right) = \left(\frac{\Delta t}{\Delta x}\right)^2 \sin^2\left(\frac{k\Delta x}{2}\right) \tag{3.14}$$

if we look for a solution

$$\frac{\omega\Delta t}{2} = \arcsin\sqrt{\left(\frac{\Delta t}{\Delta x}\right)^2 \sin^2\left(\frac{k\Delta x}{2}\right)} \tag{3.15}$$

it can be seen that for $k \simeq \pi/\Delta x$ and for $\Delta t > \Delta x$ no real solution is possible. This last statement gives us another important condition, the Courant-Levy stability criterion that is expressed for the three dimensional space and with c:

$$c\Delta t \leq \left(\frac{1}{\Delta x^2} + \frac{1}{\Delta y^2} + \frac{1}{\Delta z^2}\right)^{-1/2} \tag{3.16}$$

In Figure 3.6 the dispersion relation is shown for a 1D case. The natural dispersion relation is achieved when $c\Delta t/\Delta x = 1.0$, while for $\Delta t \to 0$ it deviates from the real case. This is important to notice because it implies that a smaller time step is not always going to improve our simulation.

3.1.7 Current weighting and filtering

In the subsection 3.1.2 we saw the general role of the particle shape function for either electromagnetic and electrostatic PIC codes. However, in electromagnetic codes this is a little more complicated than in electrostatic codes because the particles have a velocity and their effect on the fields evolution is mediated by the current density **J**. The continuity equation should be consistently implemented in the code:

$$\frac{\partial \rho}{\partial t} = -\nabla \cdot \mathbf{J} \tag{3.17}$$

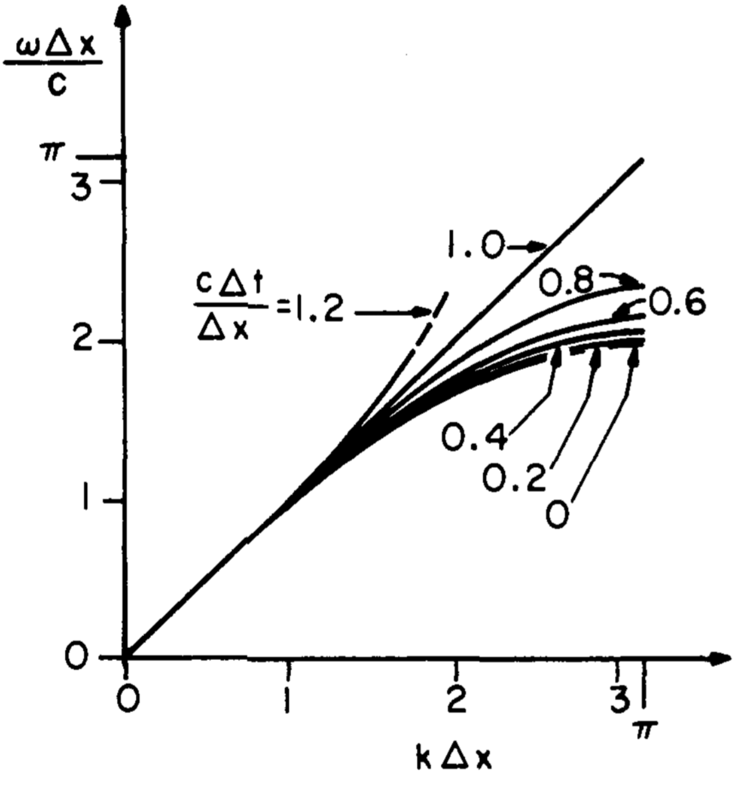

Figure 3.6: Dispersion relation for a 1D electromagnetic FDTD PIC scheme. On the y axis we have the adimensional frequency ω of the wave, while on the x axis the adimensional wavenumber k. The different lines correspond to different Courant conditions. Figure taken from Birdsall & Langdon (1991).

The most common solution is the one presented by Villasenor & Buneman (1992), where the key idea is that the currents are calculated proportionally to the amount of charge crossing a cell boundary[4]. For the case reported in Figure 3.7 (the simplest one, in 2D, more cells can be involved) the equations describing the currents are:

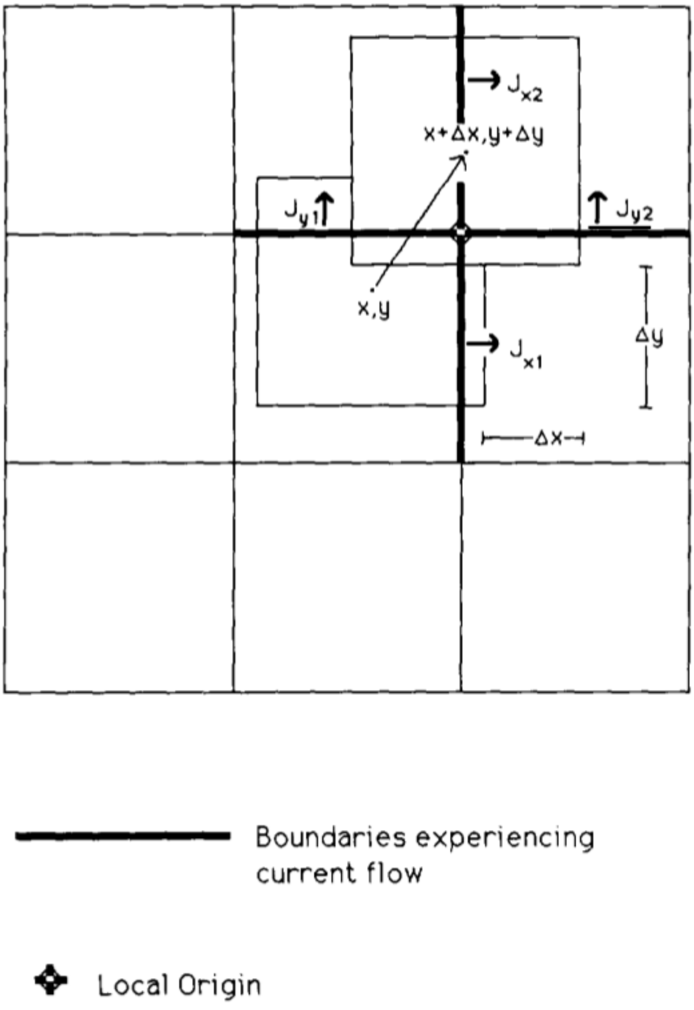
J_{x2}
$x+\Delta x, y+\Delta y$
J_{y1}
J_{y2}
x,y
J_{x1}
Δy
Δx
Boundaries experiencing current flow
Local Origin

Figure 3.7: In the simplest, most common type of move, motion of the charge will only create a current across four cell boundaries. A move as shown will create the four fluxes J_{x1}, J_{x2}, J_{y1} and J_{y2} as given in eqs. 3.18-3.21. The coordinates (x, y) describing the location of the charge center at the start of the move are measured relative to the "local origin". Figure taken from Villasenor & Buneman (1992).

$$J_{x1} = \Delta x \left(\frac{1}{2} - y - \frac{1}{2}\Delta y \right) \tag{3.18}$$

---

[4] Previous method for calculating the currents were based on particle position (Birdsall & Langdon 1991).

$$J_{x2} = \Delta x \left(\frac{1}{2} + y + \frac{1}{2} \Delta y \right) \tag{3.19}$$

$$J_{y1} = \Delta y \left(\frac{1}{2} - x - \frac{1}{2} \Delta x \right) \tag{3.20}$$

$$J_{y2} = \Delta y \left(\frac{1}{2} + x + \frac{1}{2} \Delta x \right) \tag{3.21}$$

As we said in the subsection 3.1.2 to reduce the noise in a PIC code there are two main strategies: one is to increase the number of macro particles used in the simulation, the other is to increase the order of the particle shape function. Both the methods increase considerably the computational time. Another solution is to apply digital filtering to the current densities in order to reduce the noisy behavior at short wavelengths. However this method does not always conserve Eq. 3.17 and it should be used carefully. A reference for the most common techniques is Vay & Godfrey (2014).

3.1.8 The Yee mesh

In a typical explicit PIC code the components of the electromagnetic fields are not located all at the same place: Yee (1966) found that if the components were placed in specific locations the grid assumed elegant properties. This technique was first developed for general electromagnetic FDTD algorithms. If (x, y, z) are the coordinates of the center of the cell and we assume a cubic cell of side Δ the components are placed at $E_x(x + \Delta/2, y, z)$, $E_y(x, y + \Delta/2, z)$, $E_z(x, y, z + \Delta/2)$, $B_x(x, y + \Delta/2, z + \Delta/2)$, $B_y(x + \Delta/2, y, z + \Delta/2)$, $E_z(x + \Delta/2, y + \Delta/2, z)$. The electric field components are advanced by a half cell side in their direction, while the magnetic field components are advanced by a half cell side along all the directions but the their own. Figure 3.8 gives a good idea of where these components are. The Yee algorithm centers its **E** and **B** components in three-dimensional space so that every **E** component is surrounded by four circulating **B** components, and every **B** component is surrounded by four circulating **E** components. This provides a simple picture of three-dimensional space being filled by an interlinked array of Faraday's law and Ampere's law contours. For example, it is possible to identify Yee **E** components associated with displacement current flux linking **B** loops, as well as **B** components associated with magnetic flux linking **E** loops (Taflove & Hagness 2005). Another interesting property is that the FDTD algorithm conserves $\nabla \cdot \mathbf{E}$ and $\nabla \cdot \mathbf{B}$ locally if no sources are present. For the demonstration we point the reader to Taflove & Hagness (2005), where this is demonstrated for the FDTD vacuum case. If the source **J** is inserted and the continuity equation (3.17) holds $\nabla \cdot \mathbf{E}$ is conserved globally (and locally it obeys the continuity equation) and $\nabla \cdot \mathbf{B}$ is locally conserved (there are no magnetic charges) (Birdsall & Langdon 1991). In section 3.1.7 we saw that this is possible using the current deposition scheme introduced by Villasenor & Buneman (1992).

The conservation of the two divergences is a very important property for the final solution (it prevents a whole set of unphysical solutions) and has important consequences for operations in electromagnetic PIC codes, in fact any operation that acts during the run of the code needs to be written in a way that preserves these two quantities. Otherwise the code needs to operate a Poisson equation solver on the solution and correct it, but this is in general a computationally expensive operation and the correction is not guaranteed to be the right one. A very common example for an operation is injecting charged particles in the simulation: this has to be done overlapping a positive particle to a negative one otherwise this will leave a trace in the divergence of the fields.

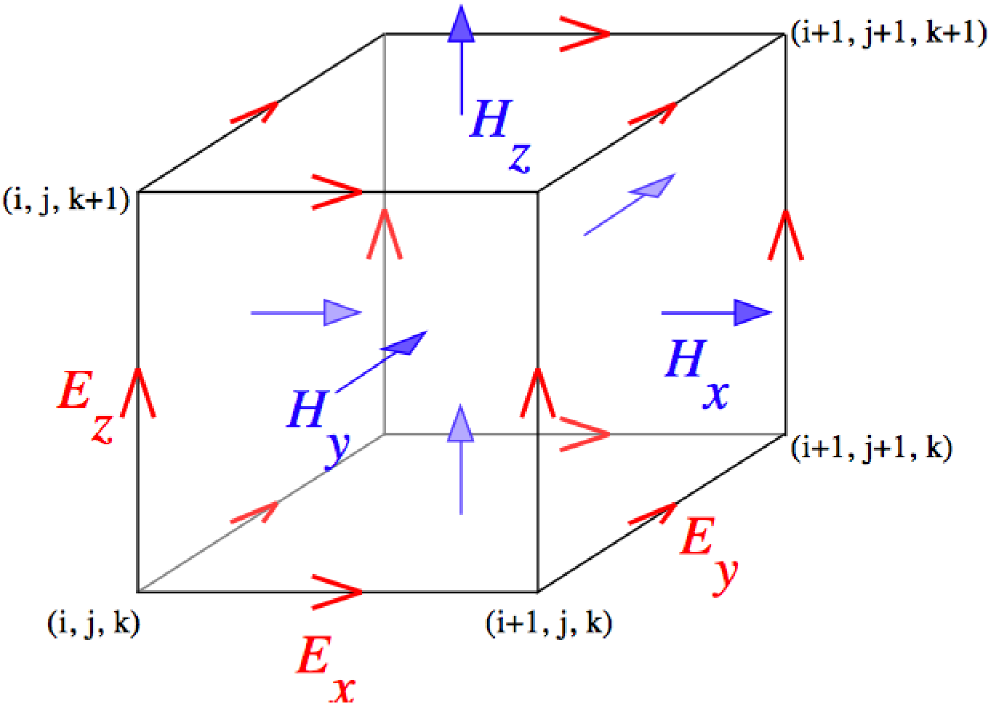
(i+1, j+1, k+1)
(i, j, k+1)
H z
H x
E z
H y
(i+1, j+1, k)
E y
(i, j, k)
(i+1, j, k)
E x

Figure 3.8: Electromagnetic component positions on a Yee mesh. Figure taken from Johnson (checked on: 2017-05-01).

3.2 A PIC code for the pulsar magnetosphere

I started my Ph.D. working on EPOCH, a 3D electromagnetic relativistic publicly available PIC code (Arber et al. 2015). However, Dr. Kalapotharakos wrote from scratch a PIC code, C-3PA[5] (Kalapotharakos et al. 2017a), and inside our group we decided to concentrate our energies on this code. Both codes are written in `fortran90`. I contributed to the developing and testing of the code. The code is developed specifically for the pulsar magnetosphere problem, however it can be modified to simulate other phenomena.

3.2.1 The real pulsar problem

As we said in Section 3.1.4, explicit PIC codes are limited by the need to resolve ω_p and λ_{sd}. Nowadays, a realistic ($B \geq 10^8$G) pulsar magnetosphere is impossible to be simulated within a 3D global simulation because of the computational resources available. In fact, ω_p and λ_{sd} are too small compared to the scales of the global magnetosphere. However, we can simulate a magnetosphere with many characteristics similar to a real one and learn some of its physics. We will simulate a rotating spherical magnet resolving its light cylinder inside the simulation domain. We will populate the magnetosphere with a magnetized ($\sigma > 10$) electron-positron plasma, see Equation 2.37. This toy model will be our pulsar. In order to achieve this we will set $B_0 \sim 10^5$G, $a = 10^6$cm (see Equations 2.2-2.7) and a stellar radius $r_0 = 0.36R_{\rm LC}$. In a real pulsar $B_0 = 10^8 \div 10^{15}$G and $r_0 = a$ that means $r_0 < 0.2R_{\rm LC}$ for MSPs and $r_0 < 0.01R_{\rm LC}$ for normal pulsars. Usually in plasma simulations it is convenient to indicate the domain size in units of plasma skin depths or Larmor radii. However, in the global pulsar magnetosphere problem these quantities range over one order of magnitude, if not two (see Table 2.1). It is good when the skin depth is resolved at least by one cell close to the neutron star surface. The gyro radius of low energy particles is difficult to resolve on the grid, but it should be resolved in the particle space, therefore the gyro frequency should be resolved by the code time step. We do not resolve λ_{sd} approximately in a sphere of radius $0.9R_{\rm LC}$ centered on the star. The consequences of this will be explored later.

3.2.2 Boundary conditions

As we said the NS has effective radius of $0.36R_{\rm LC}$. The NS surface should be very conductive because in the neutron star crust electrons are in a quantum degenerate state and therefore they behave like a metal (Chamel & Haensel 2008). The magnetic field of the star could be very complex (Reisenegger 2009), however we will implement a simple dipolar field in vacuum (see Equation 3.23). This choice is done for the sake of simplicity and because at large distance the dipolar component should dominate (Jackson 1998a). Moreover, this component is the one that is directly measured by the spin down of RPPs (Equation 1.1). In order to reproduce this setting, we set a dipolar magnetic field inside a sphere of radius $r_s = 0.28R_{\rm LC}$.

$$\mathbf{B} = \frac{3\mathbf{n}(\mathbf{n}\cdot\mathbf{m}) - \mathbf{m}}{r^3} \tag{3.22}$$

where $\mathbf{n}$ is the versor of $\mathbf{r}$, the position vector with respect to (0,0,0). $\mathbf{m} = B_0 a^3 \mathbf{u_m}$ is the magnetic moment ($\mathbf{u_m}$ is a versor) and defines the inclination angle as $\alpha = \arccos\left(\frac{\mathbf{m}\cdot\mathbf{\Omega}}{m\Omega}\right)$.

---

[5] **C**artesian **3**D **P**IC code for **A**strophysical studies.

For a rotating conductor the electric field is not zero, but is set by the stellar rotation

$$\mathbf{E} = -\frac{1}{c}(\mathbf{\Omega} \times \mathbf{r}) \times \mathbf{B} \tag{3.23}$$

So far, this boundary is the same as the one described in Spitkovsky & Arons (2002) and it resembles more a dielectric than a conductor. The main reason is that the current does not flow on this surface, but a charge entering into this region remains stuck where it crossed the boundary. This can be seen looking at $\nabla \cdot \mathbf{E}$ on any conductive wall implemented in PIC, for example shooting a particle against a wall beyond which both the fields are set to zero. A very elegant solution to this problem has been implemented in Philippov & Spitkovsky (2014), but it is computationally too expensive because it needs to follow a lot of particles. We achieved a working solution with some compromises. We implemented a transition layer outside the surface. In this layer $\mathbf{B}$ is let free to evolve according to the Maxwell equations but $\mathbf{E}$ is set according to Eq. 3.23. This layer extends between $0.28R_{\mathrm{LC}}$ and $0.36R_{\mathrm{LC}}$. We noticed that this implementation mitigates the accumulation of charges and allows currents to flow in this small region.

As we said in Section 2.2.1 a rotating magnet generates an electromagnetic wave. This wave propagates outward to infinity. Our simulation cannot be infinite, and for FDTD methods these waves touching the domain boundaries had always been a problem. In fact, these waves were reflected back and influenced the simulation. However, some solutions had been found (Taflove & Hagness 2005). We implemented the Perfectly Matched Layer (PML) boundaries (Berenger 1994, 1996). The PML acts as an infinite material that absorbs any incident wave. Thus the reflection of waves is highly decreased. When particles pass through PML we remove them. This causes a charge accumulation (because explicit PIC codes are charge conservative). However, we keep the boundary far enough from the region of interest to not influence it. We placed the PML layer between $4.5R_{\mathrm{LC}}$ and $4.8R_{\mathrm{LC}}$, on the edges of a simulation cube $(-4.8R_{\mathrm{LC}}, 4.8R_{\mathrm{LC}})$, and we tested that they not influence the simulation inside a cube of side $(-3R_{\mathrm{LC}}, 3R_{\mathrm{LC}})$.

3.2.3 Parallelization with MPI and computation time

A 3D electromagnetic PIC code simulation of the pulsar magnetosphere cannot run on a simple laptop. It needs to be parallelized and run on a super computer using many processors. We run our simulations on NCCS Discover and NAS Pleiades. Here I will describe briefly how the parallelization for our code works. Message Passage Interface or MPI, is a portable message-passing standard. The standard defines the syntax and semantics of a core of library routines. The standard has different implementations. An accurate description of all the routines can be found on the website of the implementation called MPICH (https://www.mpich.org/static/docs/v3.1/www3/ Accessed: 10/10/2017). This is not the only way to parallelize a code, but I thought to be useful to report it. Moreover, this does not intend to be a guide or tutorial to parallelize a code, but its purpose is only to describe the process. Therefore, following these steps alone will not result in a parallelized code.

Parallelization works as the cells in an organisms: they are independent entities that pass messages between them. The idea is to divide our simulation domain in these separate entities (subdomains) that will perform the computation and store the arrays of variables. Some variables can be shared by all the domains, but they cannot be the entirety of the variables because of the limited memory of each one of the cores where the computations are distributed. In this example the call to the commands is done in the style

of `fortran90`.
This is the starting point:

```
call MPI_INIT(...)
call MPI_COMM_RANK(MPI_COMM_WORLD,...)
call MPI_COMM_SIZE(MPI_COMM_WORLD,...)
```

We need to introduce two terms: communicator, group and process. A communicator can be thought of a handle to a group. A group is an ordered set of processes, where a process can be thought as the operations that will be performed on a single core. Each process is associated with a rank (a number). A first general communicator (`MPI_COMM_WORLD`) is created that knows of all the processes available. Each process gets its rank, a number that identifies itself uniquely with respect to all the other processes.
Now we create the cartesian topology: the processes are distributed on a cartesian grid. Each process communicates with another process close to it in directions orthogonal to each other. A new communicator (`comm_cart3d`) is created from the previous one and this time it knows of the cartesian topology.

```
call MPI_CART_CREATE(MPI_COMM_WORLD,...,comm_cart3d,...)
call MPI_CART_COORDS(comm_cart3d,...)
call MPI_CART_SHIFT(comm_cart3d,...)
```

In this call, we define the dimensions of the cartesian topology and if it is periodic or not. the number of dimensions is not limited to ≤ 3, therefore the domain could be a hypercube. A new communicator with this information is created. Then we assign the coordinates to the communicator on this process and we give the communicator the ranks for a shift upward or downward (e.g. `1,-1`) for each direction (e.g. `0,1,2`). For a 3D case the last call should be repeated 6 times.
Now we need to determine the ranks of the neighboring processes given their cartesian location. We will store these values in an array (`pmsd`) so that they will be always available for any MPI operation. If $crds(3)$ contains the coordinates of the process:

```
do isf=-1,1
do jsf=-1,1
do ksf=-1,1
      coordback(1)=crds(1)-isf;
      crdback(2)=crds(2)-jsf;
      crdback(3)=crds(3)-ksf;
      coordforw(1)=crds(1)+isf;
      crdforw(2)=crds(2)+jsf;
      crdforw(3)=crds(3)+ksf;
      call MPI_Cart_rank(comm_cart3d,crdback,pmsd(isf,jsf,ksf,1),ierr)
      call MPI_Cart_rank(comm_cart3d,crdforw,pmsd(isf,jsf,ksf,2),ierr)
enddo
enddo
enddo
```

However, if the simulation is not supposed to be periodic the processes on the edges of the cartesian topology will not have a neighboring process. This can be checked if `coordback` or `coordforw` exceed the dimensions given in the previous calls. In this case `pmsd` should be set equal to `MPI_PROC_NULL`. Now that the communicator is

defined, we have the process coordinates (`crds`) and all the ranks of the neighboring processes (`pmsd`). We can start our code operations and communications. Each process knows its position in the global domain (`crds`) and we can define all the variables needed from them (like the origin of the subdomain). This allows to define domains with different sizes, maintaining the cartesian topology. Usually, the most time consuming part of a PIC code is pushing the particles. If smaller domains are placed where the regions with more particles are, the simulation can be sped up. This is a form of "load balancing". In the pulsar magnetosphere problem, we know that particle density will be higher at the center of the domain. Therefore, we changed the size of the domains making them smaller at the center. Using $16^3 = 4096$ cores, a simulation with this load balancing is ~ 7 times faster than a simulation without load balancing. The domain shapes are shown in Figure 3.9. Now what matters the most are the communications inside the code. `MPI_BARRIER(MPI_COMM_WORLD,...)` tells the communicator to wait for all the processes to arrive at that point. This function should be called only when necessary, because unnecessary barriers slow down the code. `MPI_BARRIER` uses the general communicator. `MPI_SENDRECV, MPI_SEND, MPI_RECV` can be used to send and receive information between the domains. However, if there is a mutual exchange of information between the ranks, it is advised to use `MPI_SENDRECV`. If the size of the data is not known a priori, the size of these data should be transferred before transferring the data itself. The most common information to pass are individual particles that cross the domain and the field values. Usually the fields living on the grid in each subdomain have overlapping regions that are used to have the first cells of the next domains available without using MPI. These cells are called *ghost zones*. For example, a first order method needs a 1-cell thick ghost zone while a second order method needs a 2-cell thick ghost zone. Other common calls are `MPI_REDUCE` and `MPI_ALLREDUCE` that gather values from all the processes (e.g. the total number of particles). At the end of the program `MPI_FINALIZE(...)` should be called.
A small note for saving files and visualizing the content of our simulations. We used the well documented program VisIt (Childs et al. 2012) and the file formats
Silo (https://wci.llnl.gov/simulation/computer codes/silo Accessed: 20/10/2017)
and
VTK (https://www.vtk.org/ Accessed: 20/10/2017).
For their implementation we refer to the guide provided online.

3.2.4 Radiation reaction

Radiation reaction forces can be very important in plasma physics. For example in the pulsar magnetosphere, the magnetic fields are so high that the particles are supposed to lose all their perpendicular momentum very quickly, if a mechanism to give particles a pitch angle is not provided. The implementation of classical[6] radiation reaction forces in explicit PIC codes is not very well studied, however, comparisons had been done between the different techniques (Vranic et al. 2016). Radiation reaction forces need to be implemented because the frequency emitted from relativistic particles cannot be captured by the simulation, since it is too high. Radiation reaction forces can be expressed

---

[6] Classical is not opposed to relativistic. In this case classical is used in opposition to quantum, therefore to QED radiation reaction effects.

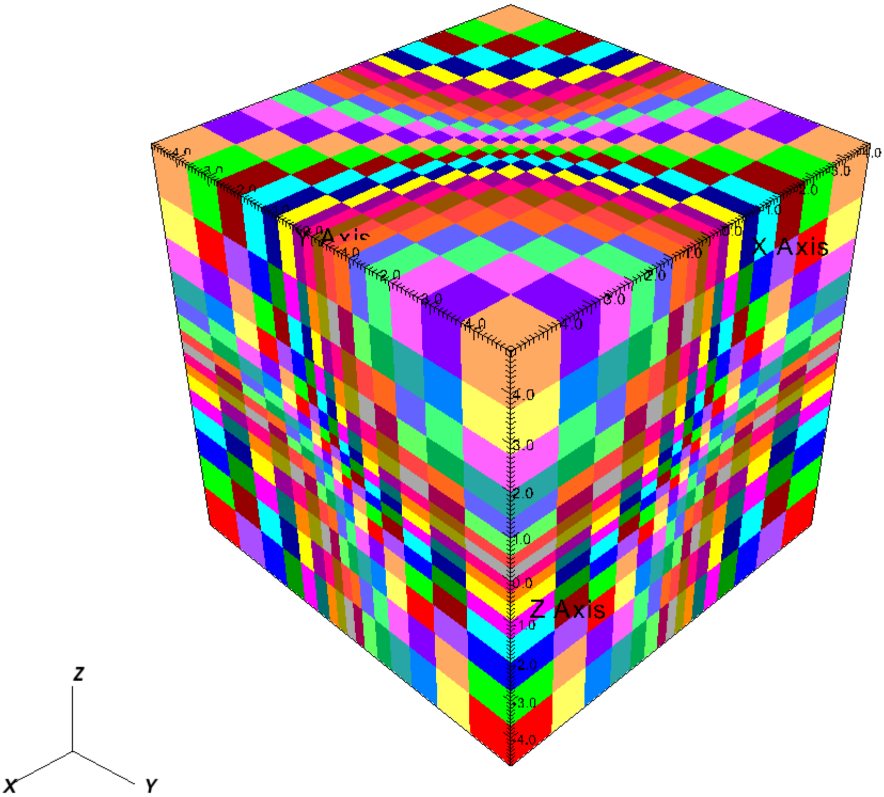

Figure 3.9: A representation of the non-uniform distribution of the computational domains implemented in the C-3PA code (16x16x16). The structure shown in takes care the load balance issue by taking into account the fact that the central regions have much higher particle number densities. The implementation keeps the original simple cartesian communication between the various sub-domains. Even though this implementation is still not optimum it can reduce the total computational times, relatively to the uniform domains, by ~ 1 order of magnitude.

with the formula given by Landau & Lifshitz (1980):

$$\mathbf{f} = \frac{2q^3\gamma}{3mc^3}\left[\left(\frac{\partial}{\partial t} + \mathbf{v}\cdot\nabla\right)\mathbf{E} + \frac{\mathbf{v}}{c}\times\left(\frac{\partial}{\partial t} + \mathbf{v}\cdot\nabla\right)\mathbf{B}\right] + \\ + \frac{2q^4}{3m^2c^4}\left[\mathbf{E}\times\mathbf{B} + \mathbf{B}\times\left(\mathbf{B}\times\frac{\mathbf{v}}{c}\right) + \mathbf{E}\left(\frac{\mathbf{v}}{c}\cdot\mathbf{E}\right)\right] - \\ - \frac{2q^4\gamma^2}{3m^2c^5}\mathbf{v}\left[\left(\mathbf{E} + \frac{\mathbf{v}}{c}\times\mathbf{B}\right)^2 - \left(\mathbf{E}\cdot\frac{\mathbf{v}}{c}\right)^2\right] \quad (3.24)$$

The first term is found to be negligible (Tamburini et al. 2010) and we tested it by applying it to stationary magnetosphere solutions. We implemented the second and the third terms following the numerical scheme outlined in Tamburini et al. (2010).

$$\mathbf{f} = \frac{2q^4}{3m^2c^4}\left[\mathbf{E}\times\mathbf{B} + \mathbf{B}\times\left(\mathbf{B}\times\frac{\mathbf{v}}{c}\right) + \mathbf{E}\left(\frac{\mathbf{v}}{c}\cdot\mathbf{E}\right)\right] - \\ - \frac{2q^4\gamma^2}{3m^2c^5}\mathbf{v}\left[\left(\mathbf{E} + \frac{\mathbf{v}}{c}\times\mathbf{B}\right)^2 - \left(\mathbf{E}\cdot\frac{\mathbf{v}}{c}\right)^2\right] \quad (3.25)$$

In general it is important to resolve the gyro time scale, because otherwise the radiation reaction losses are over estimated. However, use of the artificially low PIC fields in the radiation reaction formula will not give realistic force values for a real pulsar magnetosphere. As it was outlined in Cerutti et al. (2016) and Kalapotharakos et al. (2017a), the radiation reaction forces in a real pulsar magnetosphere would be more important than in this low magnetic field case; especially the synchrotron cooling time should be shorter. In order to have the plasma behave in this way in our toy model, we artificially decreased the synchrotron cooling time t_{sc}. When we calculate the forces acting on each single particle, we increase B to B_{eff} in Equation 3.25

$$t_{\mathrm{sc}} = -\frac{\gamma}{\dot{\gamma}} \propto B_{\mathrm{eff}}^{-2}\gamma^{-1} \quad (3.26)$$

So that $t_{\mathrm{sc}} \ll 1/\Omega$, where $1/\Omega$ is the light crossing time, but $t_{\mathrm{sc}} \geq 5\Delta t$, where Δt is the time step. In fact, the cooling time must be resolved in the simulation. Cerutti et al. (2016) implemented a different method that produced a similar effect on the particles in his code. It is difficult to test these two methods against each other, besides looking qualitatively to the particle trajectories obtained for each one of them. The reason is that both methods follow a qualitative principle, that cannot be precisely quantified. However, this does not go against the spirit of using PIC codes as toy models, as we said in Section 3.2.1.

3.2.5 A simple test: the two stream instability

Besides the tests on the individual routines, we tested the code with the two stream instability, a classical test for plasma simulations. A good reference for testing the instability in PIC codes is Birdsall & Langdon (1991). In this instability two streams of electrons are flowing one through each other. A perturbation in the density of one of the two streams is reinforced by the bunching of particles in the other stream. The instability generates an electric field extracting energy from the kinetic energy in the particles. The instability ends when all the energy that could be extracted from the relative motion finishes. The linear phase of the instability presents a growth rate of

$$\omega_{2si} = \omega_p/2 \quad (3.27)$$

The instability has also a characteristic length $\lambda_{2\mathrm{si}}$, therefore the domain of the simulation L should be larger than $\lambda_{2\mathrm{si}}$

$$L > \frac{\sqrt{2}\pi v_0}{\omega_p} \tag{3.28}$$

where v_0 is the velocity of one of the two streams. We performed the simulation in 3D and we implemented periodic boundary conditions for both fields and particles in all the three directions. In Figure 3.17 we report the measure of the growth rate in the linear phase of the instability. The plot shows the average amplitude of the electric field along the direction of the streams vs time. In the next figures we show some snapshots of the evolution of the two stream instability. A full video of the process can be found at:

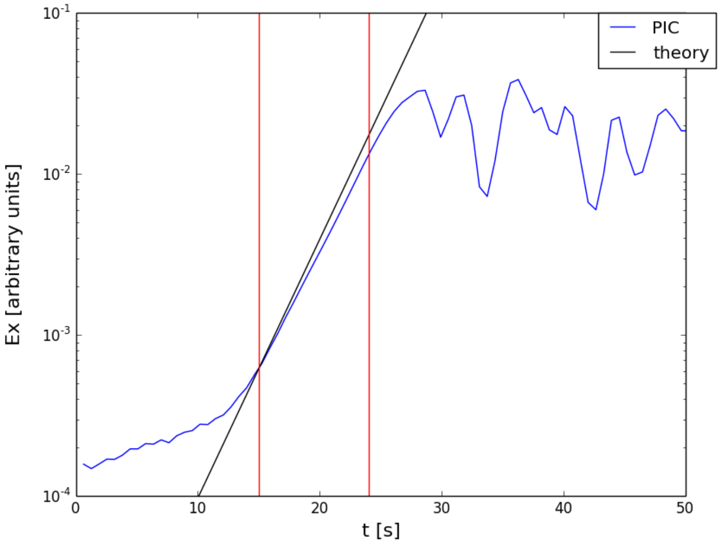

Figure 3.10: Blue line: Measure of the growth rate of the two stream instability vs time. On the y-axis we plot E_x, the average amplitude of the electric field component in arbitrary units. On the x-axis we have the time in the simulation in seconds. Black line: the expected growth rate from theory (Birdsall & Langdon 1991). The two vertical red lines indicate where we evaluated the growth rate of the instability, the beginning and the end of the linear phase of the instability.

`https://www.youtube.com/watch?v=ZZAP_oiz0pA&feature=youtu.be`
Brambilla (Accessed: 20/10/2017)

The plot on the top shows the phase space of the particles on the direction of the streams with v_x and x. The colors distinguish the two streams at the initial stage of the simulation. The plot on the bottom shows a sample of the particles in 3D. The vectors indicate the velocity vector $\mathbf{v}$ of the particles sampled, while the color and the dimension of the vectors indicate the magnitude of the velocity $|\mathbf{v}|$.

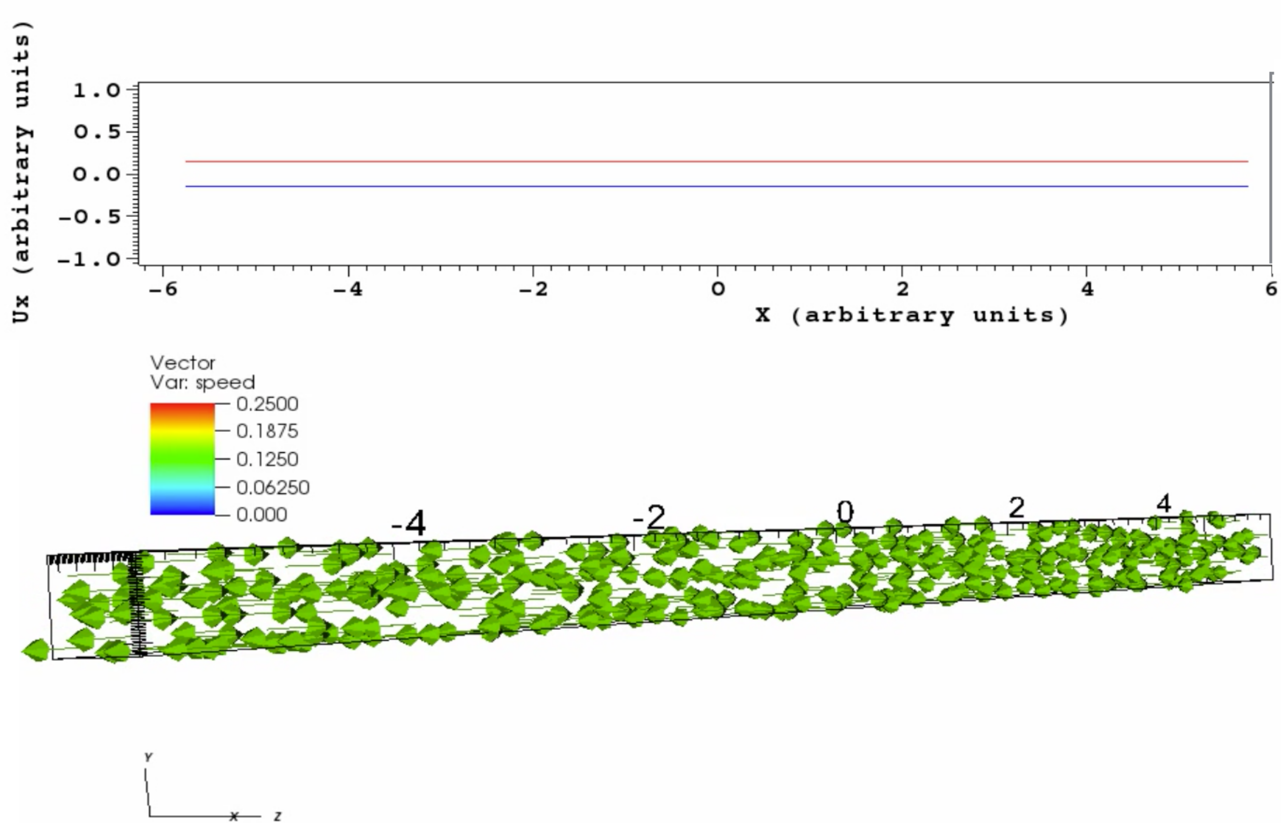

Figure 3.11: Initial stage of the simulation of the two stream instability simulation. The plot on the top shows the phase space of the particles on the direction of the streams with v_x and x. The colors distinguish the two streams of the particles. The plot on the bottom shows a sample of the particles in 3D. The vectors indicate the velocity vector $\mathbf{v}$ of the particles sampled, while the color and the dimension of the vectors indicate the magnitude of the velocity $|\mathbf{v}|$.

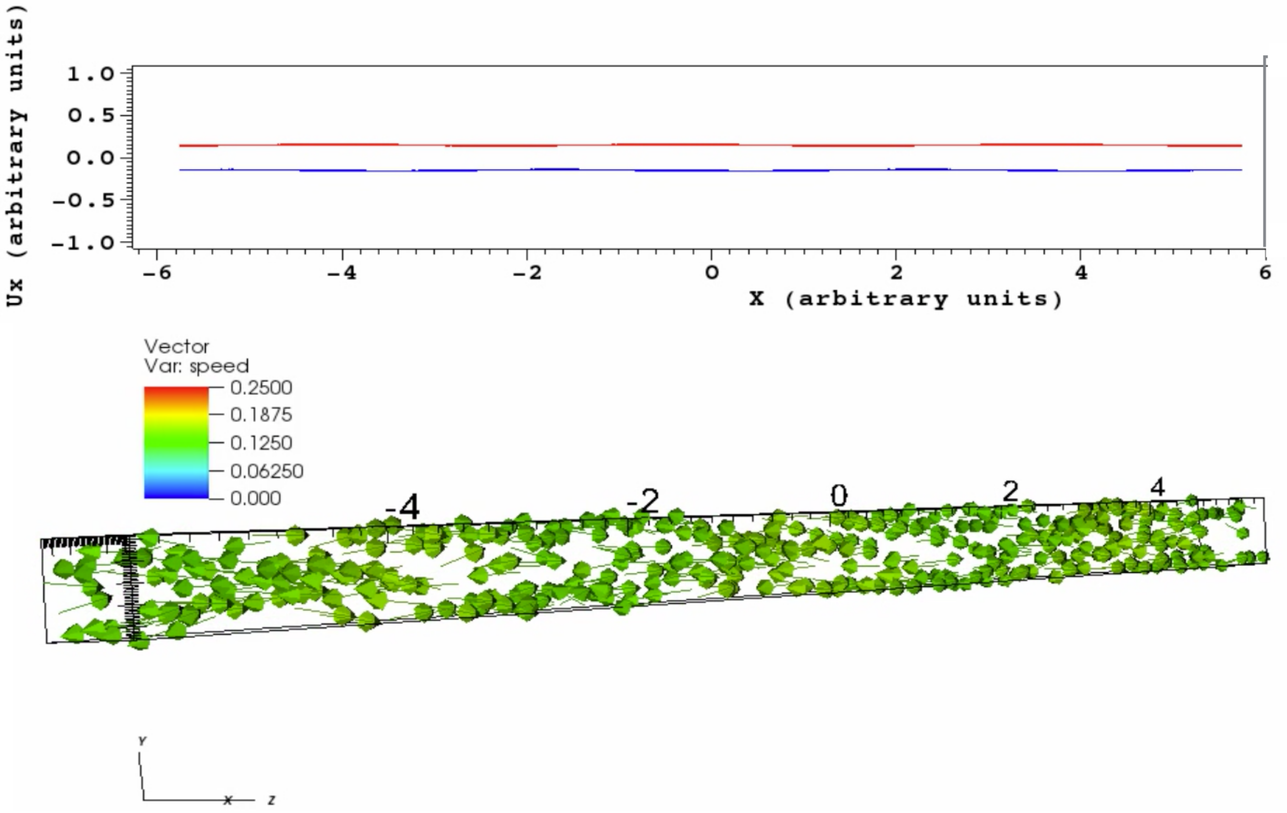

Figure 3.12: Linear phase of the two stream instability simulation. The plot on the top shows the phase space of the particles on the direction of the streams with v_x and x. The colors distinguish the two streams of the particles at the initial stage of the simulation. The plot on the bottom shows a sample of the particles in 3D. The vectors indicate the velocity vector $\mathbf{v}$ of the particles sampled, while the color and the dimension of the vectors indicate the magnitude of the velocity $|\mathbf{v}|$.

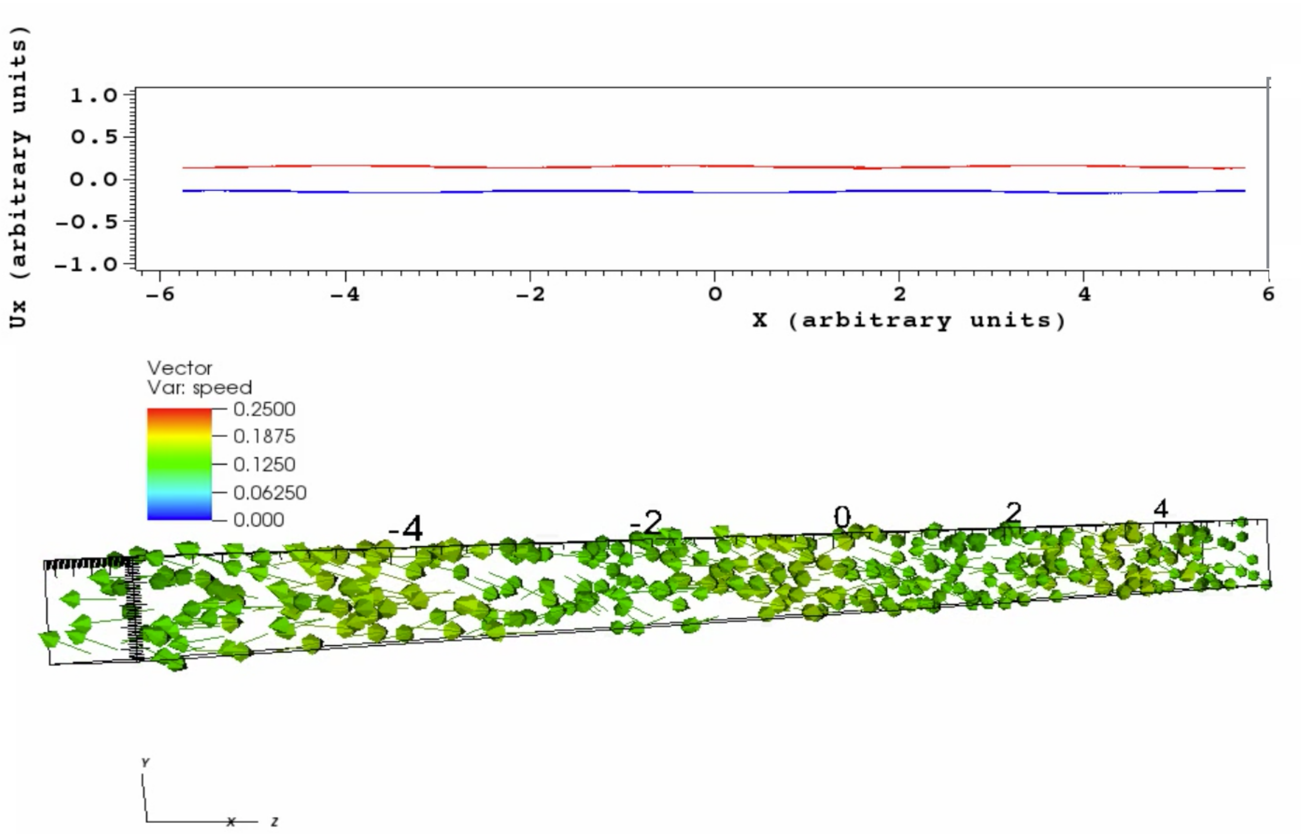

Figure 3.13: Linear phase of the two stream instability simulation. The plot on the top shows the phase space of the particles on the direction of the streams with v_x and x. The colors distinguish the two streams of the particles at the initial stage of the simulation. The plot on the bottom shows a sample of the particles in 3D. The vectors indicate the velocity vector $\mathbf{v}$ of the particles sampled, while the color and the dimension of the vectors indicate the magnitude of the velocity $|\mathbf{v}|$.

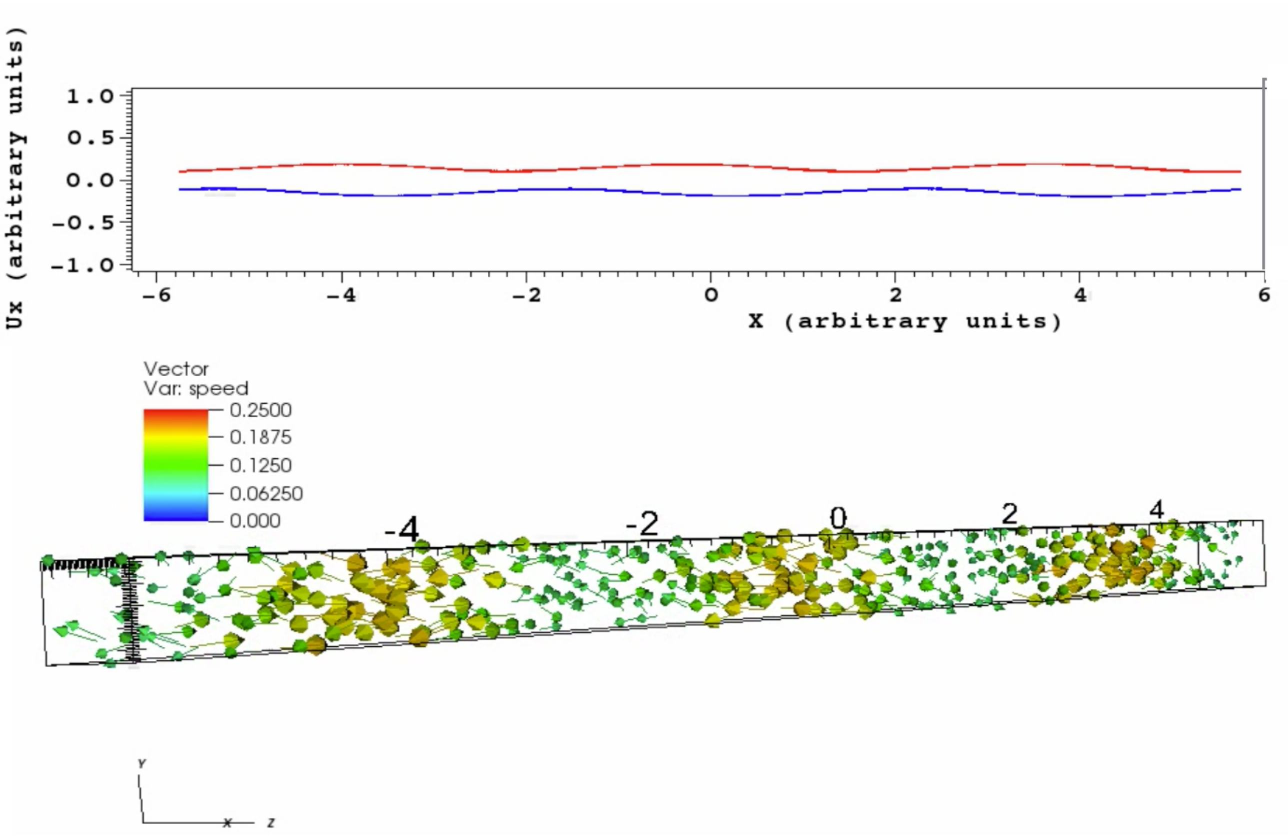

Figure 3.14: End of the linear phase/beginning of the non linear phase of the two stream instability simulation. The plot on the top shows the phase space of the particles on the direction of the streams with v_x and x. The colors distinguish the two streams of the particles at the initial stage of the simulation. The plot on the bottom shows a sample of the particles in 3D. The vectors indicate the velocity vector $\mathbf{v}$ of the particles sampled, while the color and the dimension of the vectors indicate the magnitude of the velocity $|\mathbf{v}|$.

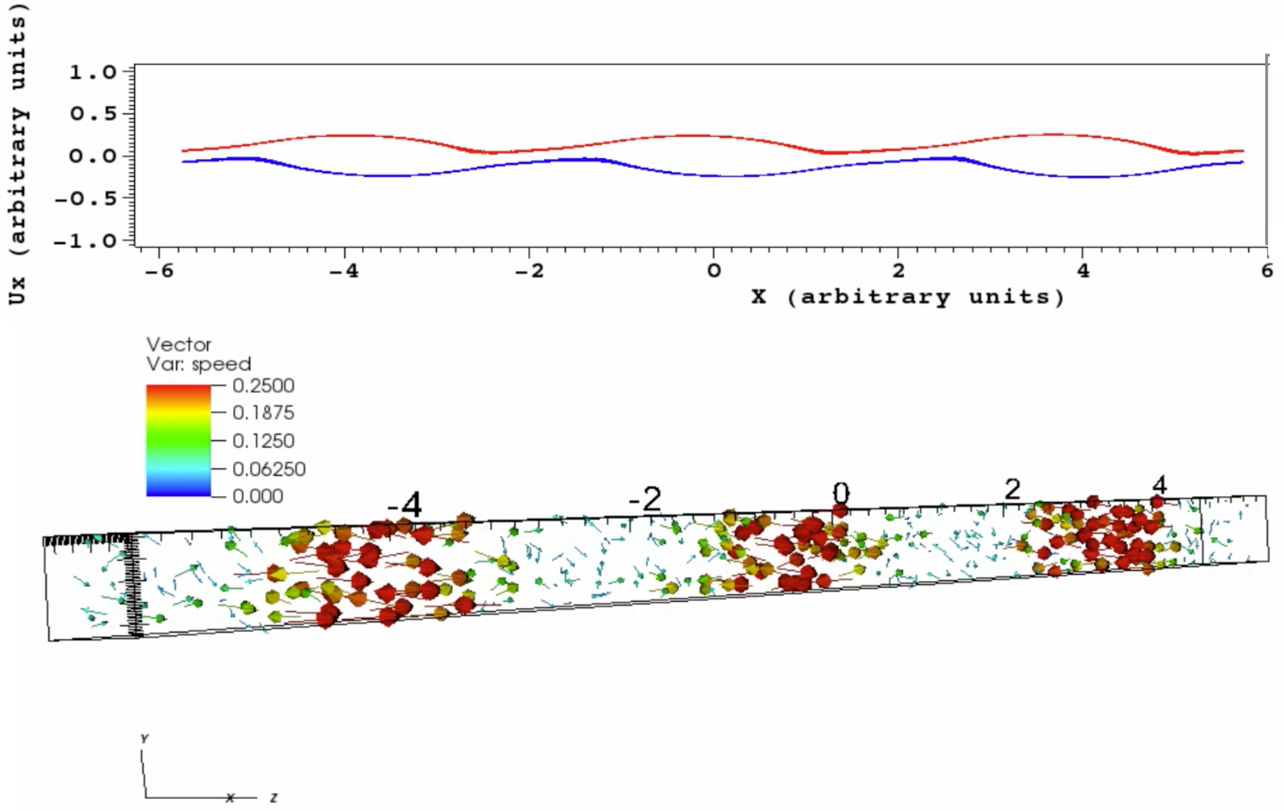

Figure 3.15: Non linear phase of the two stream instability simulation. The plot on the top shows the phase space of the particles on the direction of the streams with v_x and x. The colors distinguish the two streams of the particles at the initial stage of the simulation. The plot on the bottom shows a sample of the particles in 3D. The vectors indicate the velocity vector $\mathbf{v}$ of the particles sampled, while the color and the dimension of the vectors indicate the magnitude of the velocity $|\mathbf{v}|$.

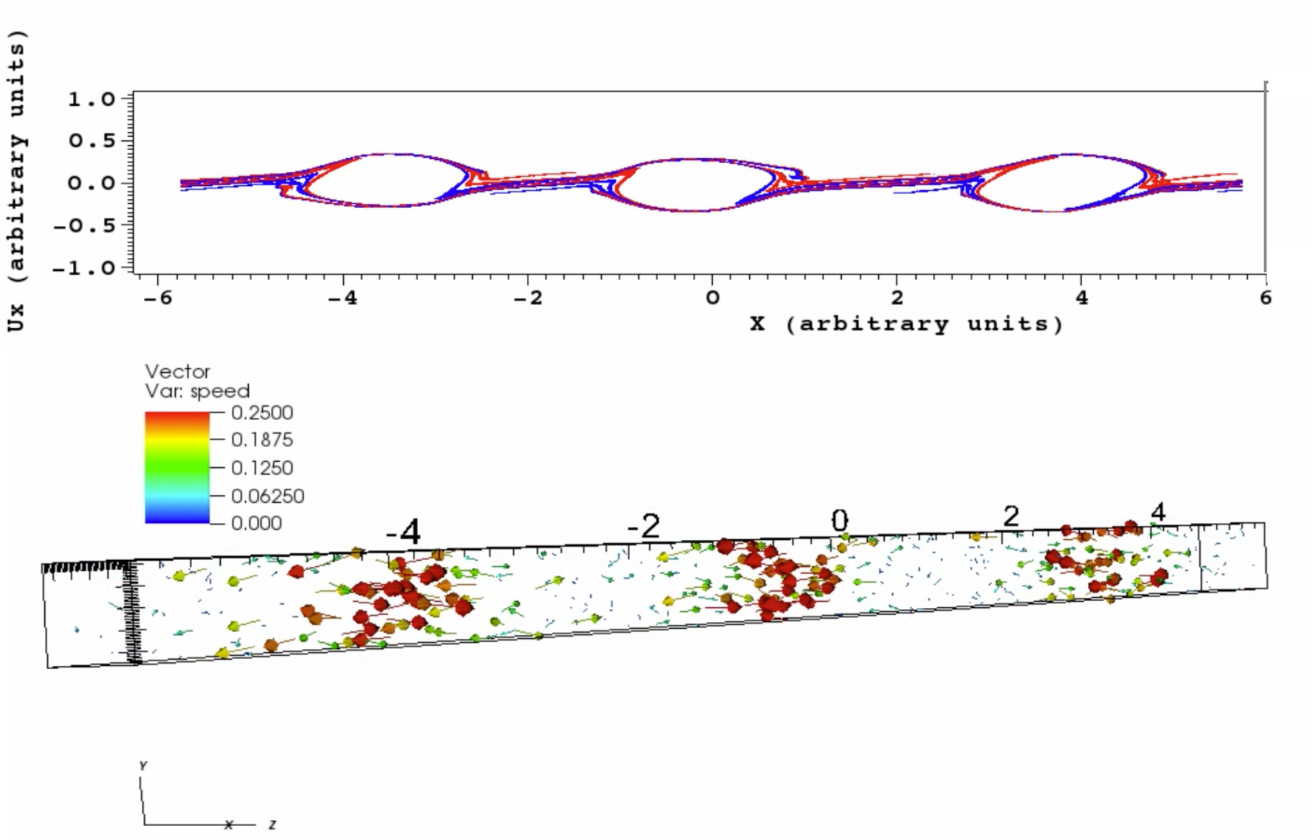

Figure 3.16: Non linear phase of the two stream instability simulation. The plot on the top shows the phase space of the particles on the direction of the streams with v_x and x. The colors distinguish the two streams of the particles at the initial stage of the simulation. The plot on the bottom shows a sample of the particles in 3D. The vectors indicate the velocity vector $\mathbf{v}$ of the particles sampled, while the color and the dimension of the vectors indicate the magnitude of the velocity $|\mathbf{v}|$.

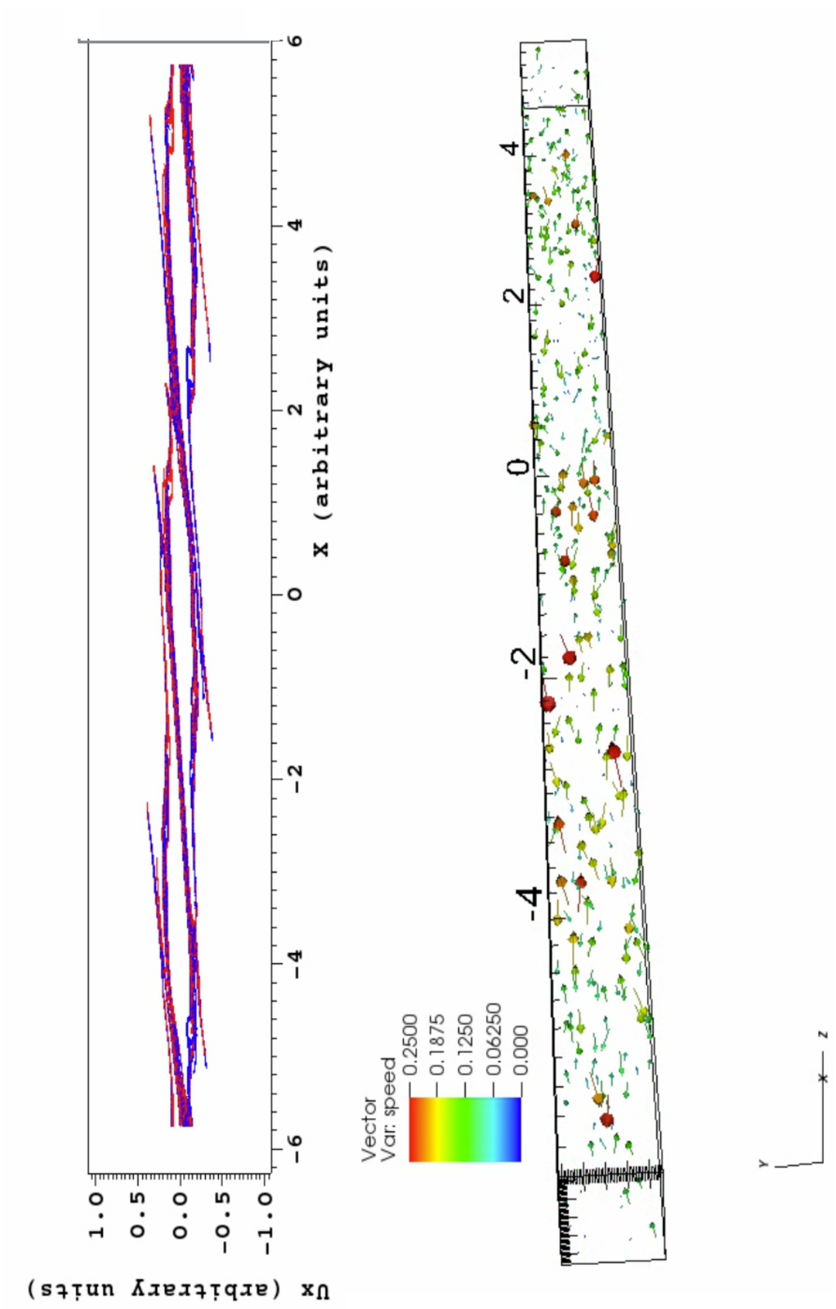

Figure 3.17: Non linear phase of the two stream instability simulation. The plot on the top shows the phase space of the particles on the direction of the streams with v_x and x. The colors distinguish the two streams of the particles at the initial stage of the simulation. The plot on the bottom shows a sample of the particles in 3D. The vectors indicate the velocity vector $\mathbf{v}$ of the particles sampled, while the color and the dimension of the vectors indicate the magnitude of the velocity $|\mathbf{v}|$.

CHAPTER 4

PIC simulations of the pulsar magnetosphere

In this chapter, I describe the research done during my three years of Ph.D. together with the group of Dr. Harding at NASA GSFC. The outcome of this work is collected in two papers that we submitted in October 2017: Kalapotharakos et al. (2017a) and Brambilla et al. (2017). I report here only the work on which I actively contributed, which entails the the entirety of Brambilla et al. (2017) and the first part of Kalapotharakos et al. (2017a). This work has been done using the PIC code C-3PA, described in the Chapter 3. First, we obtain a pulsar magnetosphere approaching the force-free limit. In order to do this we compare our PIC simulation with force-free electrodynamics simulations taken from Kalapotharakos et al. (2012) (Section 4.1). In Section 4.2, we use PIC codes and address this problem only from the point of view of the number of particles injected in the magnetosphere. We supply particles wherever they are needed and study the pulsar magnetospheres varying only this parameter. In Section 4.3, we insert one more degree of complexity, forcing the particles to be supplied only at the stellar surface. I outline the motivations for these operations in each section. I conclude this chapter with a discussion of these results. In this chapter, if not indicated otherwise, all the Figures are produced with VisIt (Childs et al. 2012). The units of the simulations are: B_{LC}, the magnetic field at the light cylinder in vacuum, for the electromagnetic fields and R_{LC}, the light cylinder radius, for the lengths. The magnetic field at the light cylinder in vacuum can be calculated with $B_{\mathrm{LC}} = B_{star}(\frac{r_0}{R_{\mathrm{LC}}})^3$. where B_{star} is the magnetic field at the star surface and r_0 the surface radius.

4.1 Force-free simulations for comparison

In this section I present the MHD force-free magnetosphere solution, in order to compare this solution to the ones we will obtain in the next sections. We use the simulations obtained with the procedure outlined in Kalapotharakos et al. (2012). These simulations are ideal force-free simulations. Figure 4.1 shows the cases for $\alpha = 0°, 45°, 90°$. The magnetosphere is charged as indicated in Section 2.3.2 . In Figure 4.1 I show the magnetosphere structure plotting $\nabla \cdot \mathbf{E}$, J and $\mathbf{J} \cdot \mathbf{B}/B$. $\mathbf{J}$ is calculated using Equation 2.32. This figure will be a useful comparison for what we will see in the next chapters.

4.2 Magnetospheres with particles supplied everywhere

In this Section, I show the pulsar magnetospheres produced supplying particles everywhere in the domain. As I mentioned above, this is done in order to have the model depending only on one parameter, the global injection rate $\mathcal{F}$.

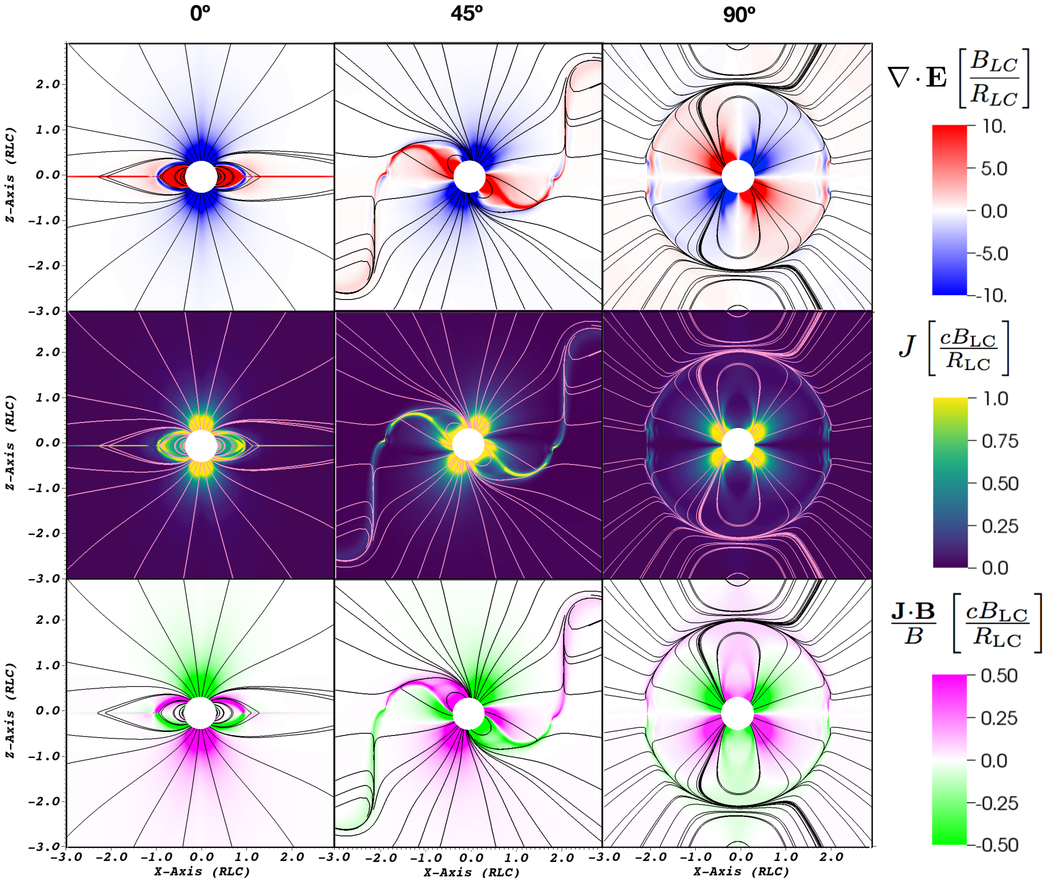

Figure 4.1: The divergence of the electric field, the absolute value of the current density and the projection of the current density on the magnetic field lines for magnetospheres close to the force-free limit for $\alpha = 0^\circ, 45^\circ, 90^\circ$.

4.2.1 Simulation set up

At each time-step and at each cell up to $r = 2.5R_{LC}$ one pair (e^-, e^+) is injected at rest (γ_L = 1; γ_L is the Lorentz factor) as long as the plasma local magnetization

$$\sigma_M = \frac{B^2}{8\pi(n_{e^+} + n_{e^-})m_e c^2} \tag{4.1}$$

exceeds a locally predefined value, Σ, that varies according to

$$\Sigma = \begin{cases} \Sigma_0 \left(\frac{r_0}{r}\right)^3, \text{if } \mathrm{r} \leq \mathrm{R_{LC}} \\ \Sigma_0 \left(\frac{r_0}{R_{\mathrm{LC}}}\right)^3 \frac{R_{\mathrm{LC}}}{r}, \text{if } \mathrm{r} > \mathrm{R_{LC}} \end{cases} \tag{4.2}$$

where Σ_0 is the value of Σ at r_0, r_0 the stellar radius. r is the radial coordinate in spherical coordinates. Our code starts with some initial (estimated) Σ_0 value which is adjusted in time so that $\mathcal{F}$ reaches the originally adopted goal-value. We tried different prescriptions for the particle injection over the whole volume, but this one gives the cleanest result. The unit of measure of $\mathcal{F}$ is the injection rate:

$$\mathcal{F}_{\mathrm{GJ}} = \frac{2\rho_{\mathrm{GJ}} A_{pc} c}{q_e} \tag{4.3}$$

where the factor 2 accounts for the two poles and ρ_{GJ} is the Goldreich-Julian charge density in the pulsar polar cap (see also Equation 2.33),

$$\rho_{\mathrm{GJ}} \sim \frac{\Omega B_0 \cos\alpha}{2\pi c} \tag{4.4}$$

where α is the inclination angle between the rotation axis and the magnetic moment, B_0 is the magnetic field at the star pole, Ω is the angular frequency of the neutron star rotation, q_e is the electron charge, and

$$A_{pc} \sim \pi r_0^3 \Omega / c \tag{4.5}$$

is the area of the polar cap. We introduce also the unit $\mathcal{F}^0_{\mathrm{GJ}} = \mathcal{F}_{\mathrm{GJ}} / \cos\alpha$ representing the ρ_{GJ} for an aligned rotator. The simulation domains are cubes of side $9.6R_{\mathrm{LC}}$ with the neutron star rotating at the center. A perfectly matched layer (PML) is implemented at the outer boundary of the domain (see Chapter 3). We use a grid size of $d = 0.02R_{\mathrm{LC}}$ and a time step small enough to resolve ω_p everywhere in the domain with at least three time steps ($dt = 0.003R_{\mathrm{LC}}/c$). We do not resolve λ_{sd} close to the star and we observe that the numerical heating gives a small speed to the particles. The simulations are obtained with a $\gamma_{max} \sim 500$

$$\gamma_{max} \sim \frac{\Omega^2 r_0^3 B_0 e}{m_e c^2} \tag{4.6}$$

where B_0 the magnetic field at the star radius. γ_{max} is the Lorentz factor of an electron accelerated through all the voltage between the center of the polar cap of an aligned rotator and the last open field line (e.g. Ruderman & Sutherland 1975). The value of B_0 is chosen small enough in order to resolve the gyro frequency everywhere in the domain and at the same time to keep the plasma well magnetized everywhere ($\sigma > 10$). The only place where σ drops is the layer inside the current sheet, but this is expected and it should happen also in the real pulsar. In these simulations $\sigma > 10$ everywhere and the gyro frequency is resolved everywhere.

4.2.2 Approaching the force-free magnetosphere

We gradually increased $\mathcal{F}$ trying to reach a solution that approach the ideal MHD solutions shown in Section 4.1. However, the proximity to this solution needs to be quantified. We identify two methods: measuring the Poynting flux along radial shells and measuring the average electromagnetic energy density in a spherical shell around the star. Then the macroscopic quantities in the solution should be similar to the ones of Section 4.1 but, as we will see later, far from force-free magnetospheres can be very similar to a solution approaching a force-free magnetosphere. The Poynting flux is a more standard method, but it can be difficult to evaluate how close the theoretical value is to a magnetosphere approaching the force-free limit because of the dissipation in the outer magnetosphere. It is always a good practice to check where the dissipation comes from in explicit PIC codes. For example, if B_0 is too low and consequently $\sigma \not> 10$ everywhere the Poynting flux will be dissipated[1]. The force-free configuration is characterized by a specific value of electromagnetic energy density (Bellan 2006). Therefore, we evaluate this quantity in our PIC simulations and we find that it saturates very well on a specific value that coincides with the quantity from the force-free electrodynamic simulations, see Figure 4.2. We consider also the average magnetic energy density, because this quantity is used for non relativistic plasma, but the behavior does not show any difference from the electromagnetic energy density. We obtain our near-force-free solution for $\mathcal{F} \sim 25\mathcal{F}_{\mathrm{GJ}}$. In Figure 4.3, 4.4, 4.5 we show the charge density, the current density

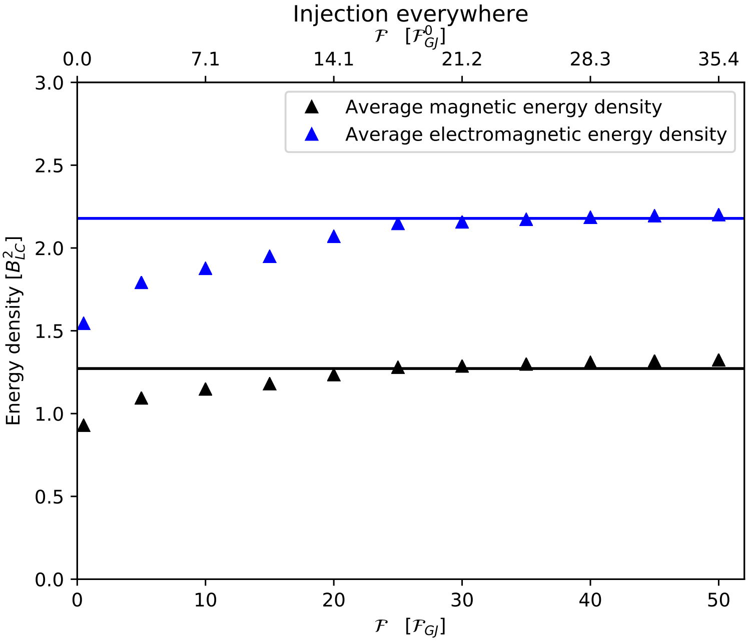

Figure 4.2: Average electromagnetic and magnetic energy density as a function of injection rate, for simulations with injection everywhere and $\alpha = 45°$. The solid lines are the expected values from force-free electrodynamics. According to this quantity the saturation to the force-free value happens at $\mathcal{F} \sim 25\mathcal{F}_{\mathrm{GJ}}$.

---

[1] All our simulations have $\sigma > 10$ everywhere; this is mostly a note of caution.

and $\mathbf{J} \cdot \mathbf{B}/B$ respectively. In this solution we can look where the most energetic particles

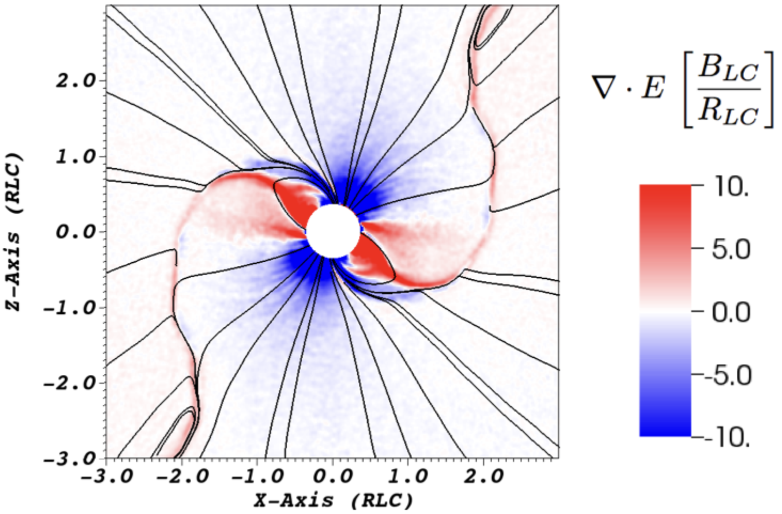

Figure 4.3: The divergence of the electric field and the magnetic field lines in the background. This magnetosphere close to the force-free limit is obtained with particles injected everywhere in the domain with $\mathcal{F} = 25\mathcal{F}_{\mathrm{GJ}}$.

are and we see that they are close to the Y-point and in the reconneccting current layer. In Figure 4.6, we show the average Lorentz factor $\langle\gamma\rangle$ that shows the importance of the Y-point and the current sheet. We obtain similar solutions for values of α that span the whole range from $0°$ to $90°$.

4.2.3 Distinguishing between noisy and accelerating electric fields

Not resolving λ_{sd} introduces artificial heating. This is a very well known behavior for a thermal plasma (Birdsall & Langdon 1991). This phenomenon is known as finite grid instability. However, the pulsar magnetosphere is a very different system from a plasma with a Maxwellian distribution, first because the distribution is strongly non-thermal, second because the plasma leaves the magnetosphere before it has time to thermalize. Moreover, the use of radiation reaction can push these differences even further. Using the simulations presented above, we study the effects of not resolving λ_{sd} in the simulation. In Figure 4.7 and 4.8 we see the changes in two simulations obtained with the same $\mathcal{F}$, one with a spatial grid of size d that is twice as thin as the other (8 times more cells). Both the simulations are without radiation reaction. In Figure 4.7 we show the two particle energy distribution in the simulations. The one obtained with $d = 0.04R_{\mathrm{LC}}$ has a larger portion of particles between $\gamma \sim 10$ and $\gamma \sim 80$ than the one with $d = 0.02R_{\mathrm{LC}}$. These particles are heated by not resolving the λ_{sd} and by the aliases introduced with the coarser macro particles (see Section 3.1.2). In Figure 4.8, we show the distribution of E_0/E in the simulation. We can see that in the magnetosphere with $d = 0.02R_{\mathrm{LC}}$ the distribution peak is shifted to lower values. This leads us to believe that this peak represents the noisy E_0, and that the change in the slope starting from ~ 0.1 is the accelerating electric field. This hypothesis is reinforced looking at Figure 4.9 which shows the E_0 in

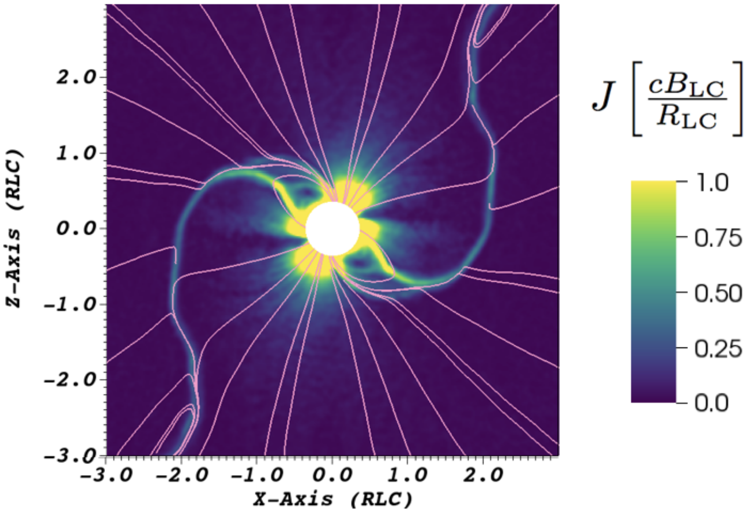

Figure 4.4: The current density and the magnetic field lines in the background. This magnetosphere close to the force-free limit is obtained with particles injected everywhere in the domain with $\mathcal{F} = 25\mathcal{F}_{\rm GJ}$.

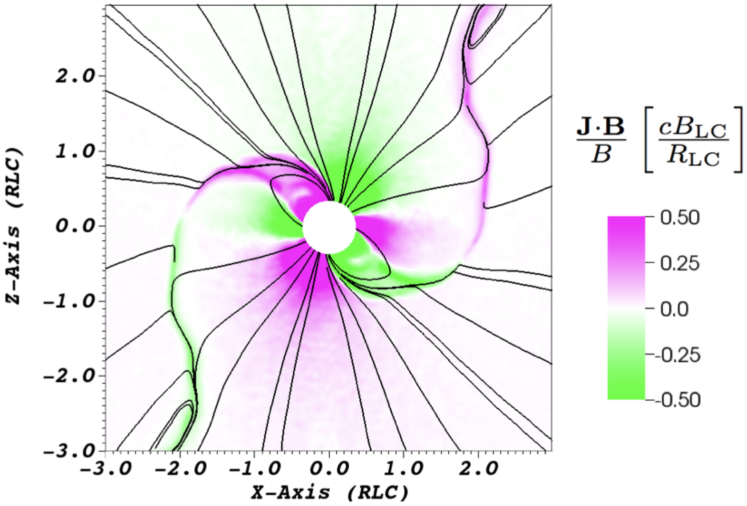

Figure 4.5: $\mathbf{J} \cdot \mathbf{B}/B$ and the magnetic field lines in the background. This magnetosphere close to the force-free limit is obtained with particles injected everywhere in the domain with $\mathcal{F} = 25\mathcal{F}_{\rm GJ}$.

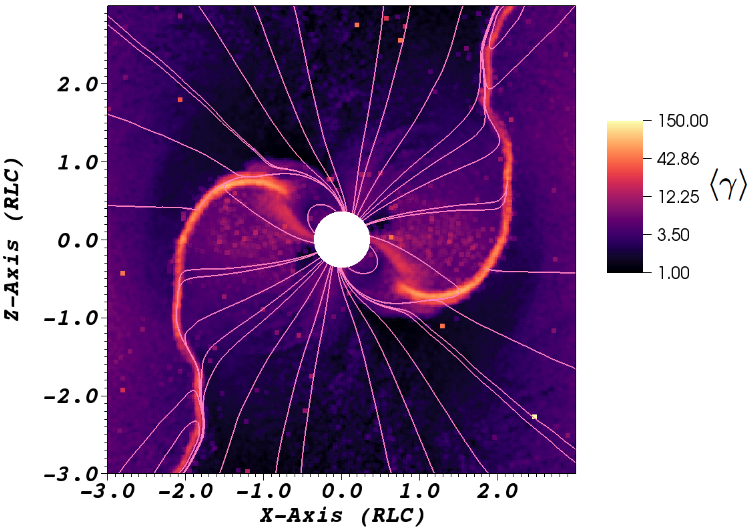

Figure 4.6: $\langle\gamma\rangle$ and the magnetic field lines in the background. This magnetosphere close to the force-free limit is obtained with particles injected everywhere in the domain with $\mathcal{F} = 25\mathcal{F}_{\rm GJ}$.

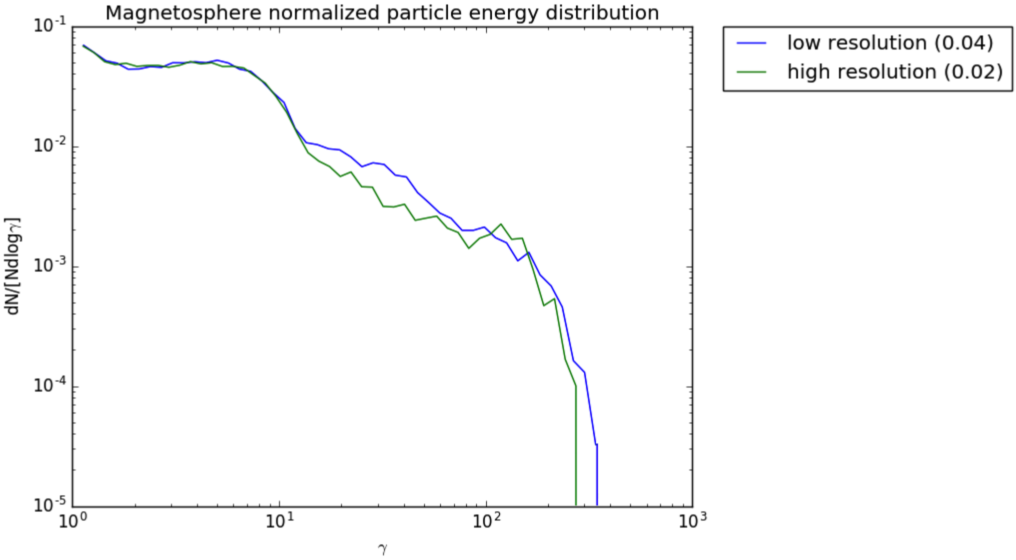

Figure 4.7: Effect on the particle energy distribution of the different resolution of $\lambda_{\rm sd}$ in two PIC simulations approaching the force-free limit ($\alpha = 45°$, $\mathcal{F} \sim 25\mathcal{F}_{\rm GJ}$). We show the particle energy distribution. The selected domain is a spherical shell between $0.36R_{\rm LC}$ and $2.5R_{\rm LC}$. In the lower resolution simulation, we have a larger portion of particles between $\gamma \sim 10$ and $\gamma \sim 80$. These particles are heated by not resolving the $\lambda_{\rm sd}$ and by the aliases introduced with the coarser macro particles.

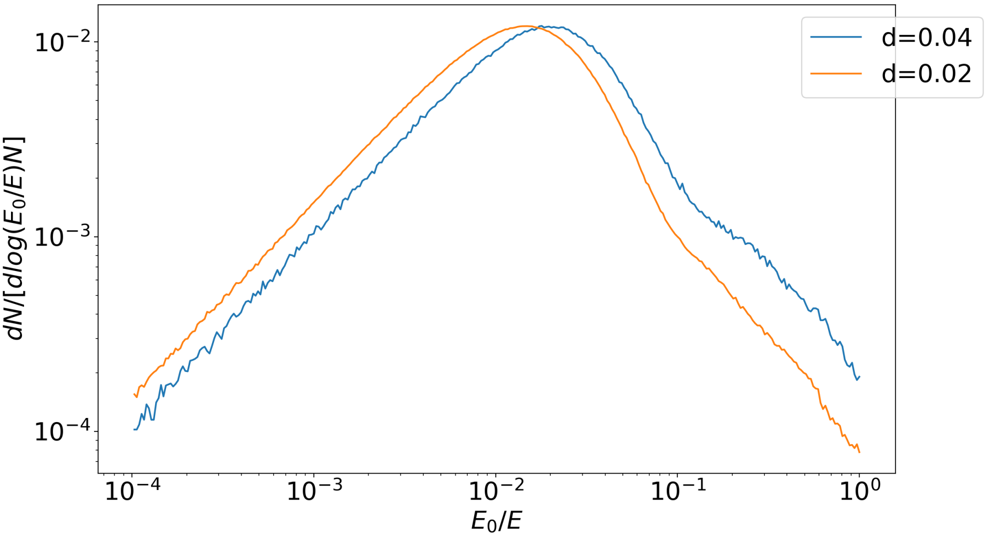

Figure 4.8: Effect on E_0 of the different resolution of $\lambda_{\rm sd}$ in two PIC simulations approaching the force-free limit ($\alpha = 45°$, $\mathcal{F} \sim 25\mathcal{F}_{\rm GJ}$). We show the distribution of E_0 inside the simulation. The selected domain is a spherical shell between $0.36R_{\rm LC}$ and $2.5R_{\rm LC}$. We can see that the noise peak shifts to the right in a lower resolution simulation.

simulations with increasing $\mathcal{F}$ (this time all the simulations are obtained with the same parameters besides $\mathcal{F}$). We can see that that as $\mathcal{F}$ increases, the bell shape grows and, when the noise starts, the peak move to the right. This hypothesis for distinguishing the accelerating electric field from the noisy one is very important for the work done in Kalapotharakos et al. (2017a).

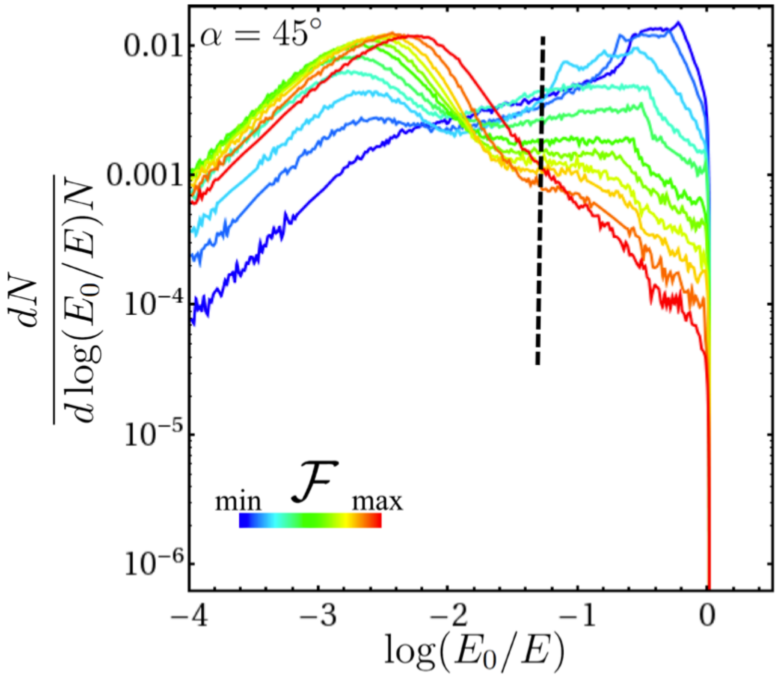

Figure 4.9: The distribution, in log-log scale, of the E_0/E values calculated at points randomly selected within the spherical shell that is defined by the stellar surface and the sphere with $r = 2.0R_{\rm LC}$. The point density corresponds to ~ 1 point per computational cell. The plotted results correspond to simulations of $\alpha = 45°$. The different colors correspond to different $\mathcal{F}$ values. $\mathcal{F}$ increases as the color changes gradually from blue to red. The vertical dashed line marks the value to the right of which we consider that the actual acceleration takes place. This Figure is taken from Kalapotharakos et al. (2017a).

4.3 Magnetosphere with particles supplied only at the surface

In the previous section, we injected particles everywhere in the domain according to Equation 4.2. This prescription is far from reality. As we explained in Chapter 2, the pair production can happen only in specific regions where particles are accelerated by two channels, single photon and double photon pair production. We decided to ignore the photon-photon pair production that can happen in the outer magnetosphere and we considered a magnetosphere with particles supplied only at the neutron star surface. This is because we start from the hypothesis that pair production on the polar cap is always going to happen, while the pair production in the outer magnetosphere might not always take place. The comparison between the magnetosphere obtained with surface injection only and the one obtained with injection everywhere will give us the two extremes between which a real magnetosphere can be found.

4.3.1 Simulation setup

The simulation setup is similar to the previous case, but this time particles are injected in a small layer that extends from $0.36R_{\rm LC}$ to $0.5R_{\rm LC}$. The prescription for the magnetization becomes:

$$\Sigma = \Sigma_0 \left(\frac{r_0}{r}\right)^3 \tag{4.7}$$

Injecting particles only from the surface generates solutions with a higher density of particles close to the star. This makes the noise related to the resolution of $\lambda_{\rm sd}$ worse. In order to evaluate this effect, we consider the layers around the star up to $0.5R_{\rm LC}$. We do not resolve λ_{sd} approximately in a sphere of radius $0.9R_{\rm LC}$ centered on the star. We observe that the numerical heating gives a small speed to the particles. The upper limit of this speed is $\gamma \lesssim 30$, but only 1.7% of the particles reach $\gamma > 20$. However, we consider as physical only $\gamma \gtrsim 30$. The simulations in this paper are obtained with a $\gamma_{max} \sim 500$

4.3.2 Formation of a force-free like magnetosphere

The possibility to fill the entire magnetosphere and make it nearly force-free everywhere with injection of particles only from the surface has been shown in Cerutti et al. (2016). However, Cerutti et al. (2016) focuses mostly on the high-energy emission and not on the magnetosphere structure. As we increase the $\mathcal{F}$ at the stellar surface we expect to find many different magnetosphere configurations ranging from charge-separated magnetospheres (Krause-Polstorff & Michel 1985; Spitkovsky & Arons 2002) to a close to force-free solution (Contopoulos et al. 1999; Spitkovsky 2006). First, we use again the average electromagnetic energy density method outlined in Section 4.2.2 to find at which $\mathcal{F}$ value our magnetosphere approached the force-free limit. The result for $\alpha = 45°$ is $\mathcal{F} = 12.5$ as it is shown in Figure 4.10. We reach a near force-free solution for all the values of α. In Figure 4.11 we show the charge density of near force-free magnetospheres with inclination angle $0°$, $45°$, $85°$ obtained with this method. We use $85°$ instead of $90°$, since for $\alpha = 90°$ the injection rate unit is 0 (Equation 4.4). For the different inclination angles we find also a different distribution in the energy of electrons and positrons (Figure 4.12): when the current sheet is completely positively charged (aligned case) positrons are accelerated at higher energies than electrons, when the current sheet approaches a symmetry of the opposite charges ($\alpha \sim 90°$) this difference disappears. As we mentioned in the previous Section the Poynting flux also reflects this approach to the force-free limit. The Poynting flux increases toward the force-free value as $\mathcal{F}$ increases. The two values between which the Poynting flux varies are the force-free and the vacuum spin down power $\dot{\mathcal{E}}$ both indicated in Chapter 2. In Figure 4.13 we evaluate the Poynting flux through spherical shells for pulsars with $\alpha = 45°$ with increasing $\mathcal{F}$. The Poynting flux decreases along the radial direction because it gets dissipated by $J \cdot E$ in the volume enclosed by the shell. However, we note that the dissipation, especially for the higher $\mathcal{F}$, takes place close to the LC, and beyond that near the equatorial current sheet. In Figure 4.13 we see that the maximum dissipation happens for $\mathcal{F} = 3.5\mathcal{F}_{\rm GJ}$ and does not exceed 15% of the Poynting flux at the surface. The maximum percentage in dissipation happens for $\mathcal{F} = 0.5\mathcal{F}_{\rm GJ}$ (~ 20%) but this is because the absolute value of the Poynting flux is lower. The dissipation decreases monotonically going toward the force

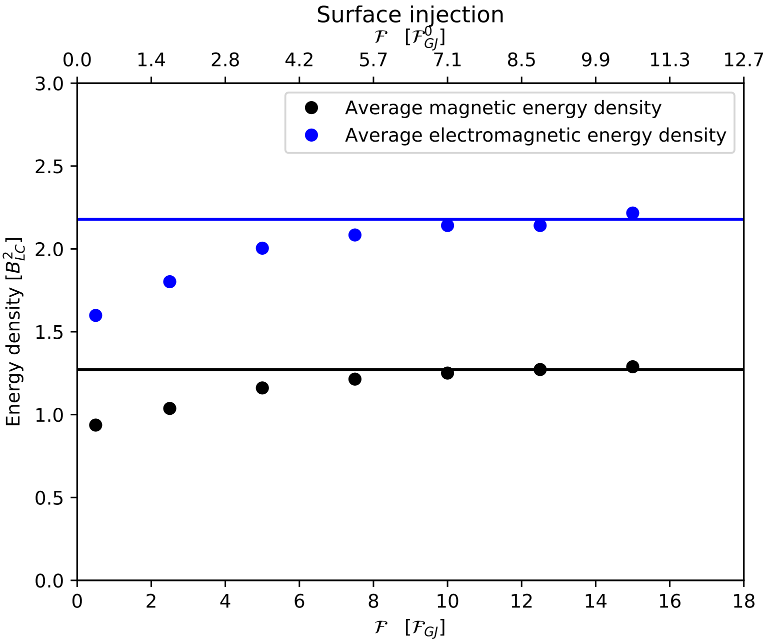

Figure 4.10: Average electromagnetic and magnetic energy density as a function of injection rate, for simulations with injection from the surface and $\alpha = 45°$. The solid lines are the expected values from force-free electrodynamics. According to this quantity the saturation to the force-free value happens at $\mathcal{F} \sim 12.5\mathcal{F}_{\rm GJ}$.

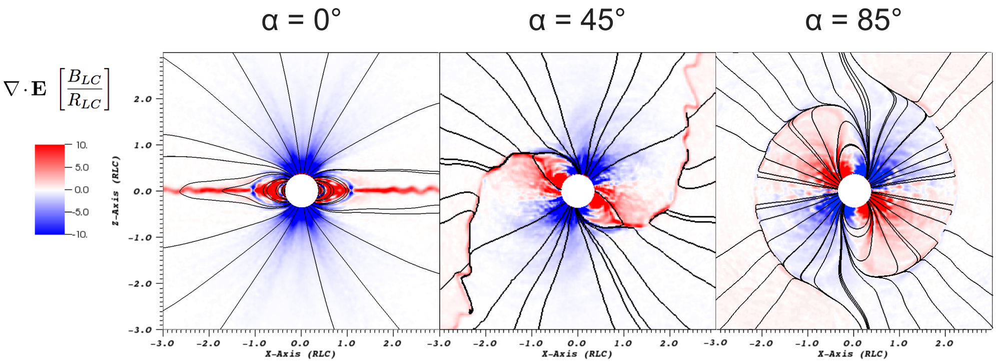

Figure 4.11: In this figure we show the close to force-free simulations obtained injecting particles from the surface. We show cases that cover the whole range of inclination angles α. The color is the divergence of the electric field, while the field lines are the magnetic field lines projected onto the poloidal plane. The $0°$ case is obtained with $\mathcal{F} = 5\mathcal{F}_{\rm GJ} = 5\mathcal{F}^0_{\rm GJ}$, the $45°$ case with $\mathcal{F} = 12.5\mathcal{F}_{\rm GJ} = 8.84\mathcal{F}^0_{\rm GJ}$ and the $85°$ with $\mathcal{F} = 125\mathcal{F}_{\rm GJ} = 10.89\mathcal{F}^0_{\rm GJ}$.

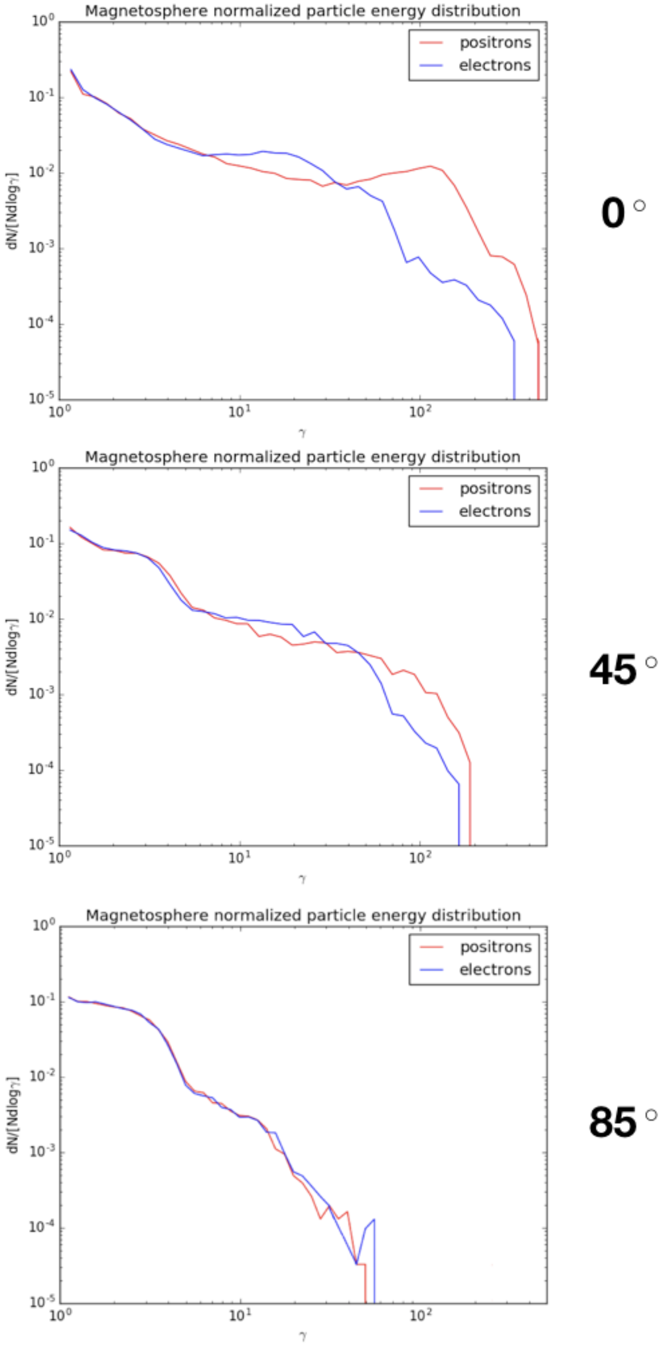

Figure 4.12: Electron and positron energy distribution for near-force-free magnetospheres with different α: when the current sheet is completely positively charged (aligned case) positrons are accelerated at higher energies than electrons, when the current sheet approaches a symmetry of opposite charges ($\alpha \sim 90^\circ$) this difference disappears.

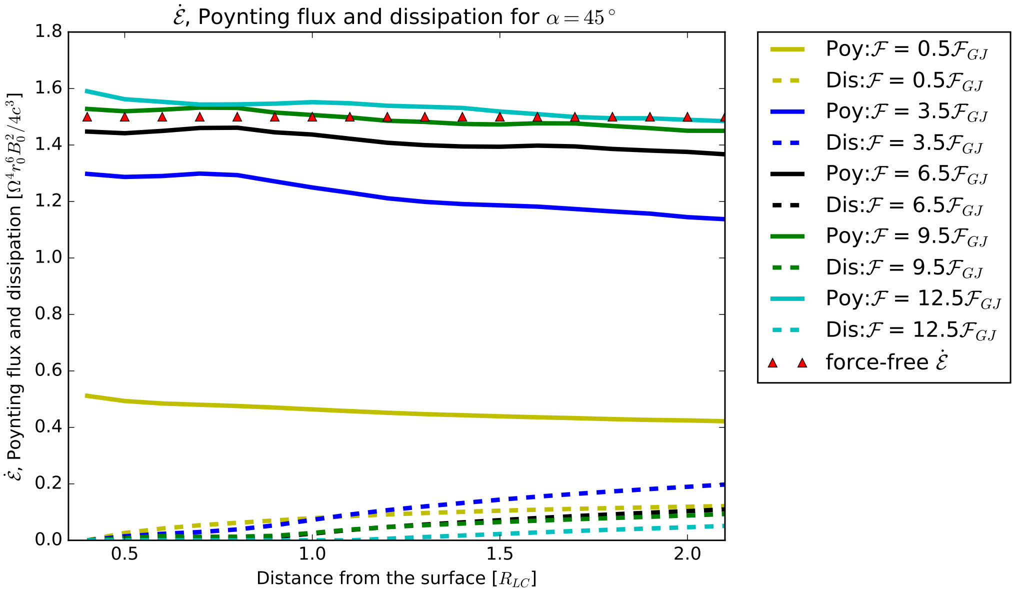

Figure 4.13: Variation of the Poynting flux and of the dissipation with the radial distance for different injection rates. This plot is for the $\alpha = 45^\circ$ case.

free solution from $\mathcal{F} = 3.5\mathcal{F}_{\rm GJ}$. The dissipation for the nearest to force-free solution is $\sim 6\%$. However, Poynting flux and electromagnetic energy density are not the only two quantities of interest. Studying how the magnetosphere changes its configuration while the number of particles injected increases is interesting because it shows possible configurations in which a pulsar can operate. The magnetic field structure, shown in Figure 4.14, begins to resemble the force-free structure already from $\mathcal{F} \sim 5\mathcal{F}_{\rm GJ}$, while for $\mathcal{F} = 0.5\mathcal{F}_{\rm GJ}$ it is very close to the vacuum one. The evolution of the current configuration seems to follow the magnetic field structure, in particular once the magnetic field resembles the force-free one, a clear separatrix/Y-point/current sheet configuration is present. We consider the accelerating electric field to be E_0 (Gruzinov 2008; Li et al. 2012) that is defined as:

$$B_0^2 - E_0^2 = \mathbf{B}^2 - \mathbf{E}^2 \tag{4.8}$$

$$B_0 E_0 = \mathbf{B} \cdot \mathbf{E} \tag{4.9}$$

with $E_0 \geq 0$. The electric field gets gradually screened with higher particle injection, but we can see that the regions that are hardest to screen are the polar cap outflow region and the separatrix region. When the current sheet region is formed, it never gets completely screened. Another effect that we expected is the relationship between E_0 and particle energy distribution. The more E_0 is unscreened, the higher the energy to which particles can be accelerated. If we look at the total particle energy distribution in Figure 4.15, we can see that the fraction of particles that are accelerated to higher energies is the largest for the smallest $\mathcal{F}$.

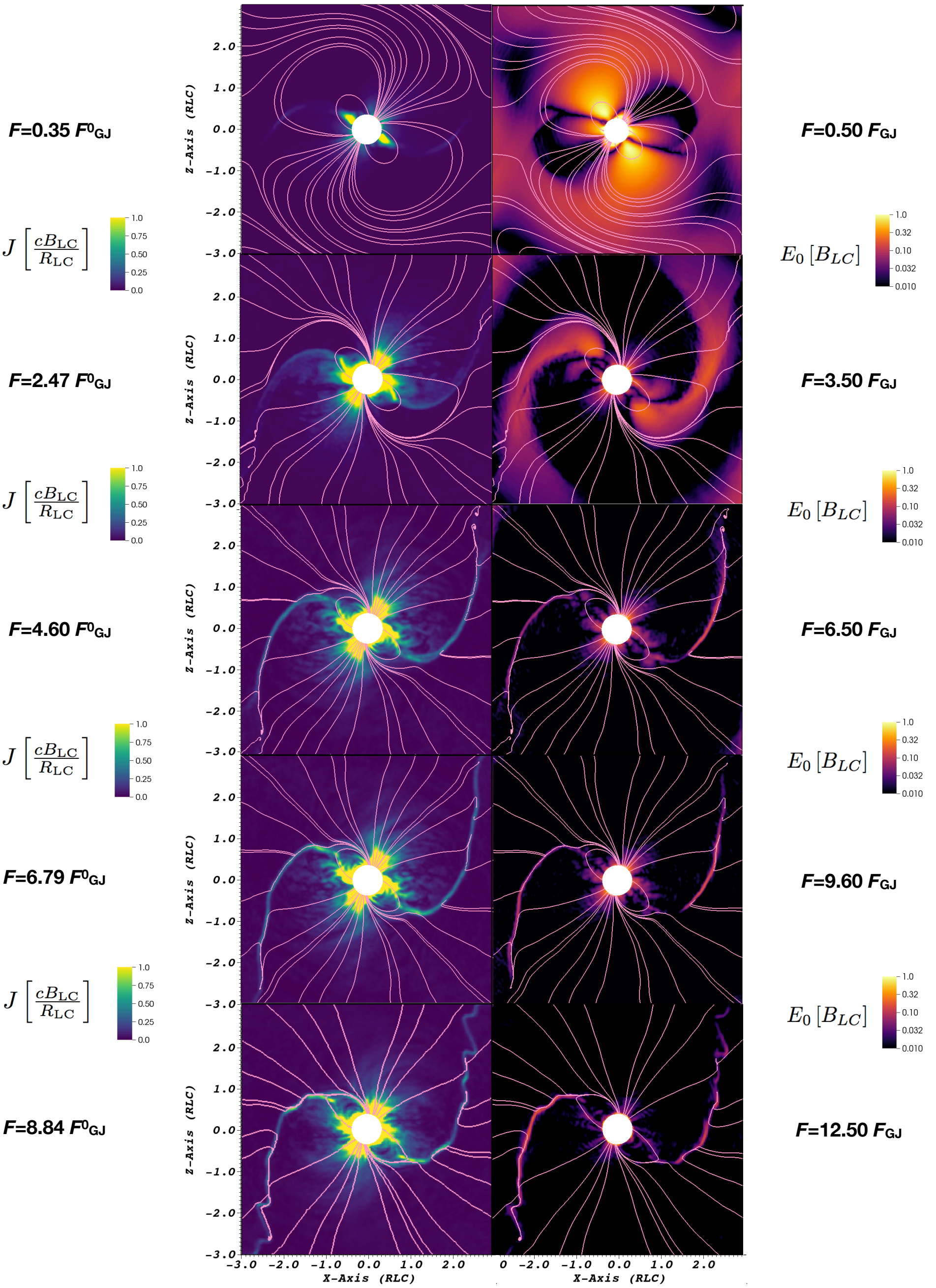

Figure 4.14: This Figure shows how J and E_0 (this last one defined in Equations 4.8 and 4.9) varies with the injection rate $\mathcal{F}$. The field lines in the background are the magnetic field lines. The gradual screening of E_0 and the formation of the force-free current structure are shown.

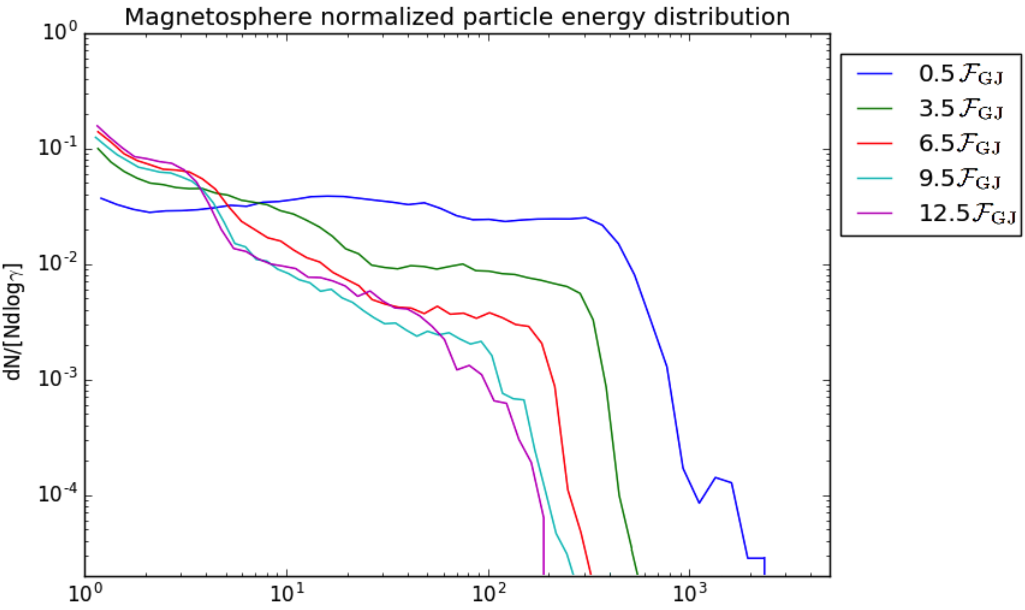

Figure 4.15: Total particle energy distribution for different $\mathcal{F}$. This plot is obtained for solutions with $\alpha = 45^{\circ}$.

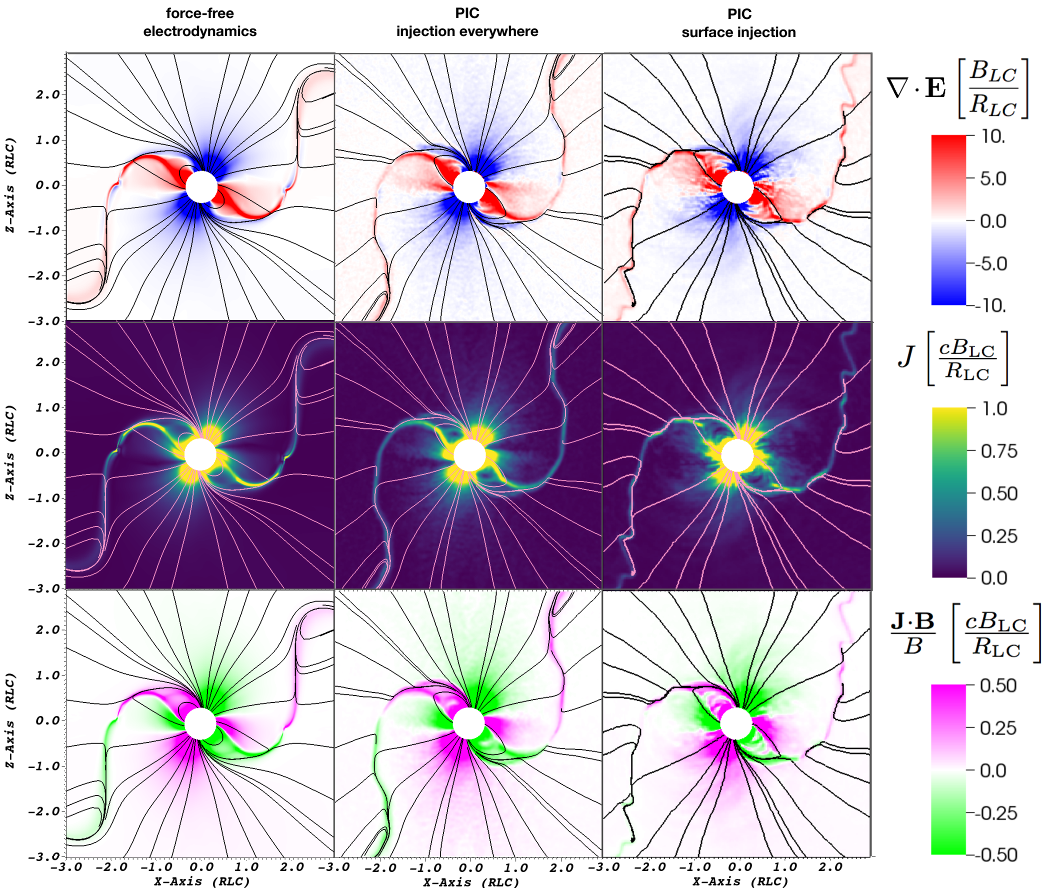

Figure 4.16: The divergence of the electric field, the absolute value of the current density and the projection of the current density on the magnetic field lines for magnetospheres close to the force-free limit obtained with three different kinds of techniques: force-free electrodynamics, PIC with particles injected everywhere in the domain, PIC with particles supplied only at the surface. As it can be seen, these plots are very similar.

4.3.3 Comparison between solutions approaching the force-free limit

As we said before, we are interested in comparing the magnetosphere structure obtained with the two different injection distributions. In Figure 4.16 we compare the solution obtained with force-free electrodynamics to two PIC simulations approaching the force-free limit: one injecting particles everywhere in the simulation domain and one injecting particles only close to the star surface. The $\nabla \cdot \mathbf{E}$ (which represents the charge density), the total current and its sign are very similar in all the solutions. The situation changes when we look in detail at how these structures are sustained.
For this comparison we define the multiplicity M as the number of particles present per charge at a given location.

$$M = \frac{N_{ele} + N_{pos}}{|N_{ele} - N_{pos}|} \tag{4.10}$$

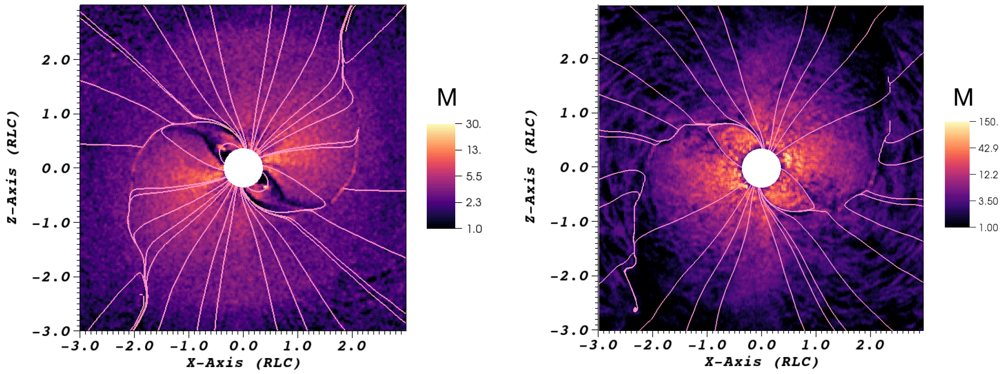

Figure 4.17: Multiplicity profile for PIC simulations close to the force-free limit: on the right particles are supplied only at the stellar surface, on the left particles are injected everywhere. When particles are injected only at the surface the multiplicity is higher out to a radius of $1R_{\rm LC}$, similar up to $2R_{\rm LC}$ and lower up to $3R_{\rm LC}$. The color scale is logarithmic.

The multiplicity reaches higher values when the particles are injected at the surface, as can be seen in Figure 4.17. But this is not the only consequence. We modified the code in order to save separately the contribution of the two particle species to the currents:

$$\mathbf{J} = \mathbf{J}_{\mathbf{pos}} + \mathbf{J}_{\mathbf{ele}} \tag{4.11}$$

where $\mathbf{J}_{\mathbf{pos}}$ and $\mathbf{J}_{\mathbf{ele}}$ represent the positron and electron currents, respectively. We plot their absolute value components in Figure 4.18. In the case when particles are injected everywhere, electron currents are present mostly in the negatively charged regions, while positron currents are present mostly in the positively charged regions (for the charge density plot see Figure 4.16). When we inject particles from the surface, we notice that the electrons (positrons) have an important current contribution even in positively (negatively) charged regions. As we saw in Figure 4.16, the total current densities are very similar, but the difference in electron and positron current densities indicates that when we inject particles only from the surface there are regions where electrons and positrons are streaming in the same direction with electron and positron currents almost cancelling each other, which result in a much lower value of the total current density. This is possible if these particles are injected in a zone where the accelerating electric field is screened enough to not reverse their initial velocities acquired by the numerical heating. The same qualitative behavior is present in the electron-positron pair cascades at the polar cap. In fact, in polar cap cascades most of the pairs are produced above the pair formation with some initial Lorentz factors (Harding & Muslimov 2001; Timokhin & Harding 2015). When particles are injected everywhere in the domain, they are supplied wherever they are needed. Instead when particles are injected only from the surface, they need to arrange themselves in a different way to satisfy the current and charge density requirements of the magnetosphere.
In Figure 4.19 where we plot $\mathbf{J} \cdot \mathbf{B}/B$ for the electron and positron components, this scenario becomes clear. For the simulation with injection from the surface, we can see that $\mathbf{J} \cdot \mathbf{B}/B$ indicates counter streaming flows (where the two components have the same color in the same region) only on the negative branch of the separatrix and in a thin layer just above the neutron star surface, where particles are injected. In the simulation

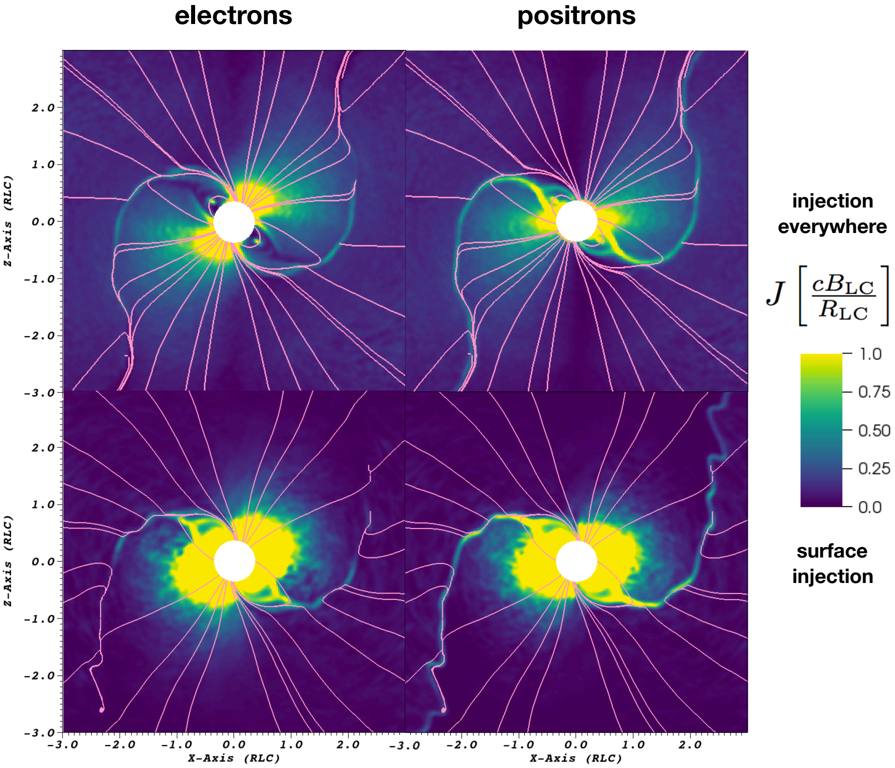

Figure 4.18: Electronic and positronic modulus of the current densities for PIC simulations close to the force-free limit: one is with particles supplied only at the star's surface, the other is with particles injected everywhere.

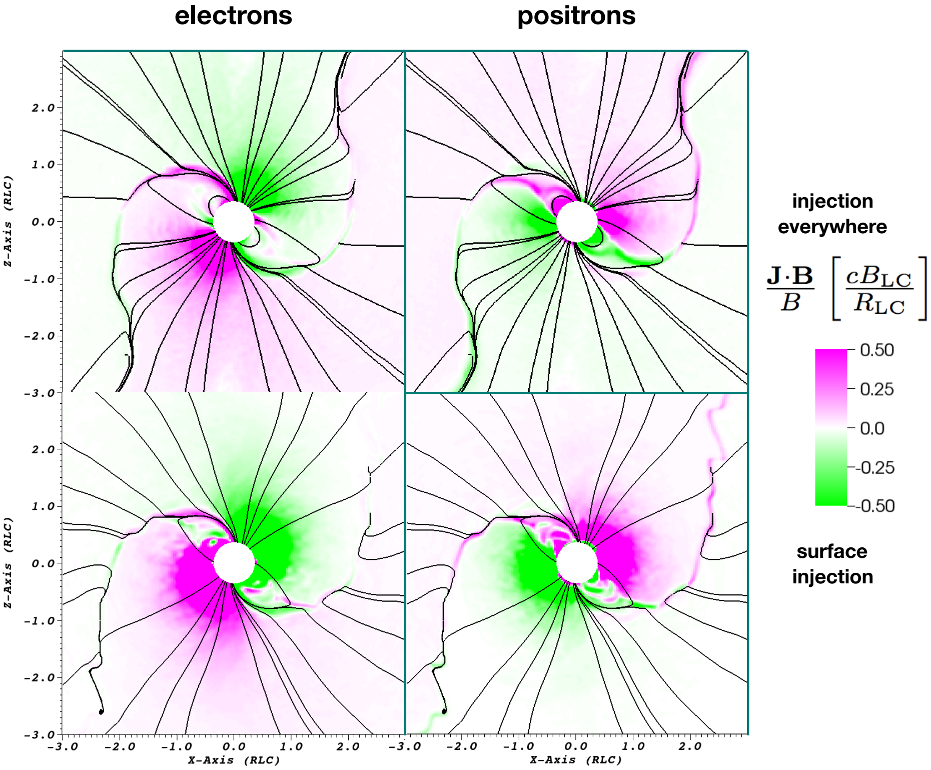

Figure 4.19: Electronic and positronic projection of the current density on the magnetic field lines for PIC simulations close to the force-free limit: one is with particles supplied only at the star's surface, the other is with particles injected everywhere.

with injection from the surface, there is a clear component of positrons flowing out from the polar cap together with the electrons; this component is very weak in the simulation with the particles injected everywhere. In the electron component the positive branch of the separatrix that connects the star surface to the Y-point changes sign: in the surface injection case, on this branch the electrons are flowing outward from the star, while in the injection everywhere case they are flowing in. Therefore, we see that the zones with availability of pairs (where the pair creation happens) greatly influence the underlying currents of the single species.

4.3.4 Particle trajectories

After we noticed the interesting current structure outlined in the previous Section, we look at the particle trajectories. We study the trajectories of the particles in our simulation approaching the force-free limit with injection from the surface ($\mathcal{F} = 12.5\mathcal{F}_{\rm GJ}$). First we describe trajectories followed by the majority of the particles. In general the most energetic particles (the ones that reach γ from ~ 50 up to ~ 180 in the 45° close to force-free simulation) are mainly positrons accelerated along the field lines that constitute the separatrix\Y-point\current sheet complex. The particles gain most of their energy in the proximity of the Y-point. At intermediate energies ($\gamma \sim 40$) we find the electrons flowing from the polar cap. Then at low energies ($\gamma < 30$) we find the bulk of the flow with electrons and positrons generally flowing out together. As expected, positrons are dominant in positively charged regions and electrons are dominant in negatively charged regions. In Figure 4.20, we see some examples of these trajectories. All the trajectories are shown in the corotating frame. Studying PIC simulations of the pulsar magnetosphere is interesting because it can provide solutions to problems that are present in the force-free electrodynamics limit. One of these problems, is how the current structure of the force-free configuration could be sustained by particles in real pulsars, outside the strict force-free limit. It is reasonable to assume that the field structure of a pulsar magnetosphere is stationary, therefore, the amount of charge in the magnetosphere should remain constant. Because of the charge conservation it follows that the current leaving the star should be balanced by a current entering the star. When Contopoulos et al. (1999) found the first force-free solution for a dipolar magnetic field, the currents were going from the star to infinity and coming from infinity to the star, one through the polar cap flow, the other mainly through the current sheet and separatrix, and a smaller part on a few open magnetic field lines close to the last open magnetic field lines. The surface charge density of the current sheet has some puzzling features. The charge of an aligned force-free magnetosphere at the Y-point should be negative inside the Y-point and positive outside of it (Lyubarskii 1990; Timokhin 2006). However, the current is continuous through the Y-point, but its composition should change to obtain a charge of a different sign. It is not clear how electrons can flow back to the star and positrons flow into the current sheet both from the Y-point, especially when particles are injected only at the surface. An outer gap (Cheng et al. 1976) was thought to provide electrons flowing backward and positrons flowing outward where the charge density changes sign. Studying the particle trajectories, we have found that the pulsar magnetosphere does not need pair production in an outer gap to fill the magnetosphere and maintain the charge density distribution of the separatrix/Y-point/current sheet complex. As we said above, there is an outward flow of electrons from the polar cap. Some of them have $\gamma \sim 1$ and flow very close to the region where the current changes sign. There, a low electric field drags part of the low energy electron distribution into the returning current and separatrix region, where the majority of them form the returning

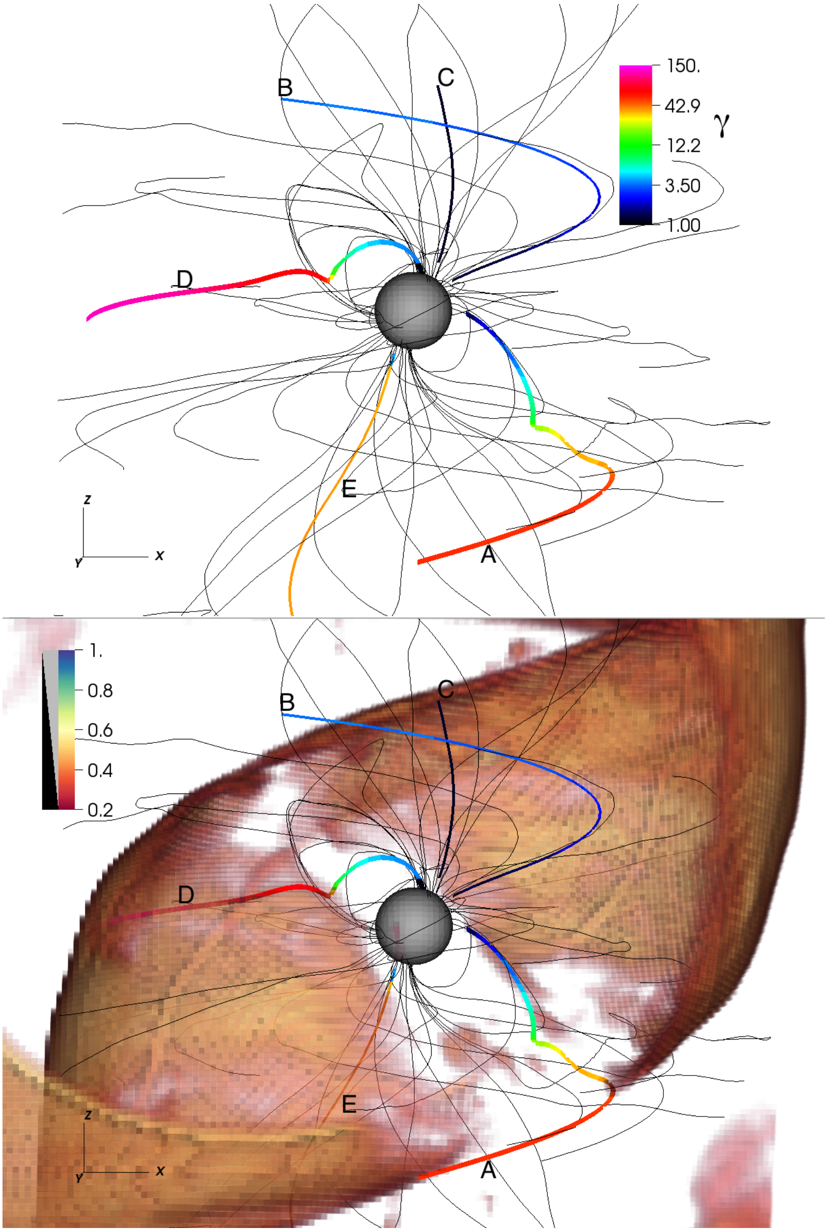

Figure 4.20: Most common particle trajectories in the simulation approaching force-free with particles supplied close to the surface. The color on the trajectories represents the Lorentz factor (γ). A) is a "not so highly" accelerated positron. B) is a positron flowing out from the polar cap flow at low energy. C) is an electron flowing out from the polar cap flow at low energy. D) is a "highly accelerated" positron. E) is an intermediate energy electron flowing out from the polar cap. In the picture on the bottom, we have a volume rendering of E_0 (Equation 4.8, 4.9) that identifies the current sheet: we can see that the difference in acceleration between A) and D) is due to the strength of E_0 on the trajectory. This non uniformity in E_0 is found only through PIC simulations and it can be useful to model the γ-ray emission. All the trajectories are in the corotating frame.

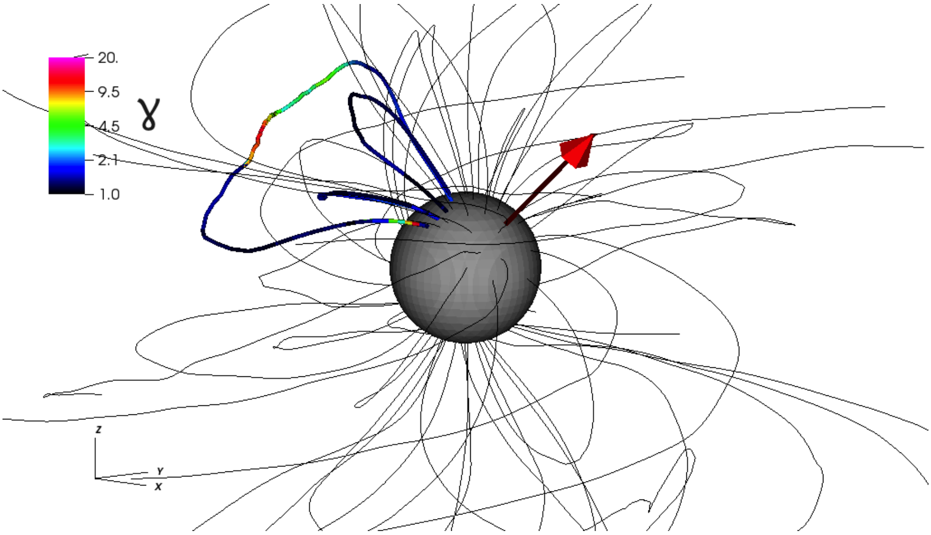

Figure 4.21: Electron trajectories falling back on the star from different heights. The Lorentz factor γ is the color on the trajectory. We added a red arrow representing the magnetic moment, because the zoomed region could be difficult to identify. Note that the color scale has a different range with respect to all the others shown in this paper for trajectories. This is because of the low energy of these particles. The trajectories are in the corotating frame.

current by the electric field that reverses their velocity (Figure 4.21). The particles with a higher energy are not affected by this because this accelerating electric field is too small. This phenomenon does not happen at a specific height, but it appears continuous up to the Y-point.

Another phenomenon concerns the outgoing electrons. Some electrons remain stuck at the Y-point and they circle all around the light cylinder, see Figure 4.22 (a similar behavior was shown also in Cerutti et al. (2016)). This happens because the solution tends toward the force-free one where the sign of the charge density is negative before the Y-point and positive after it. The resulting electric field accelerates positrons and deflects the electrons. In this motion the electrons get energized, $40 \lesssim \gamma \lesssim 90$. Once they are in this regime electrons have two possibilities: either falling back toward the star (and they mix with the electrons of Figure 4.21) or flying out following other field lines (they do not usually fly far out into the current sheet). When they fall back they lose their energy by radiation reaction (the accelerating fields in that region are not strong enough to sustain the Lorentz factor they had reached). Beyond $1.5R_{\mathrm{LC}}$ there are very few electrons that turn back and the number of these returning ones decrease drastically with distance.

To complete the picture, we must understand the origin of the positrons that support the charge density change of sign through the Y-point. Most of the positrons in the current sheet come along the separatrix; but extra positrons are needed in the current sheet to account for the current of the returning electrons inside the Y-point. They come from the polar cap flow (they are flying out with the electrons), close to the returning current region and the separatrix and they cross field lines outside the light cylinder to enter into the positively charged region and then the current sheet (Figure 4.23). We check that positrons indeed cross magnetic field lines (for the returning electrons it was obvious because of the shapes of their trajectories) looking at the cosine of the angle between the

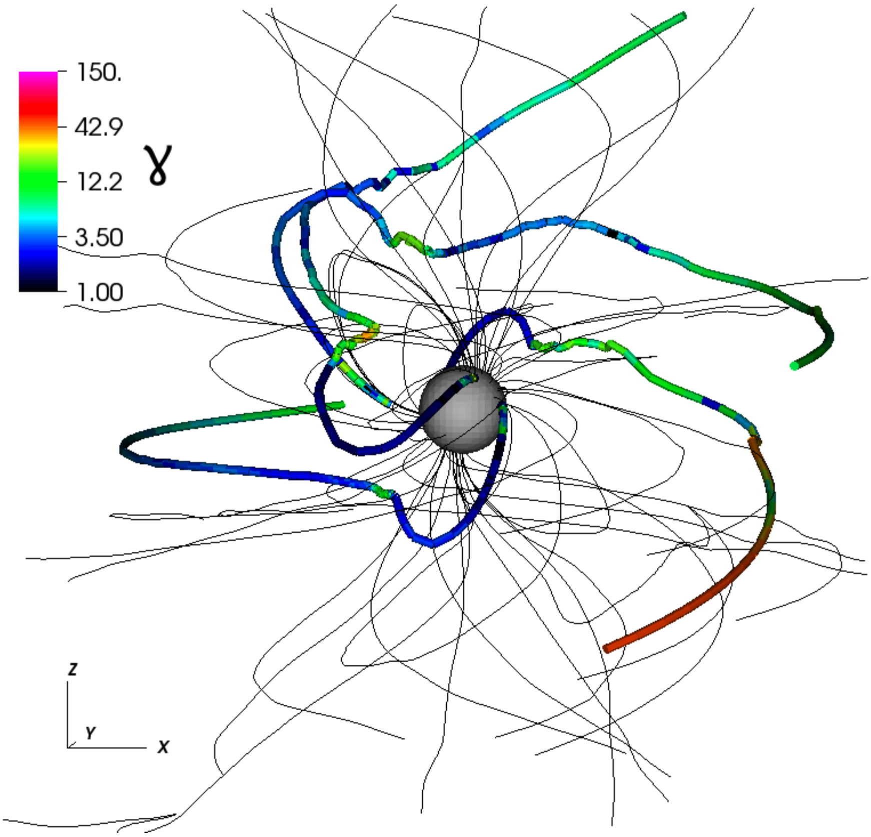

Figure 4.22: Electron trajectories circling around the Y-point and the light cylinder. Identifying the light cylinder might be difficult, however looking at where the last closed magnetic field lines are is a good approximation

. The Lorentz factor γ is the color on the trajectory. The trajectories are in the corotating frame.

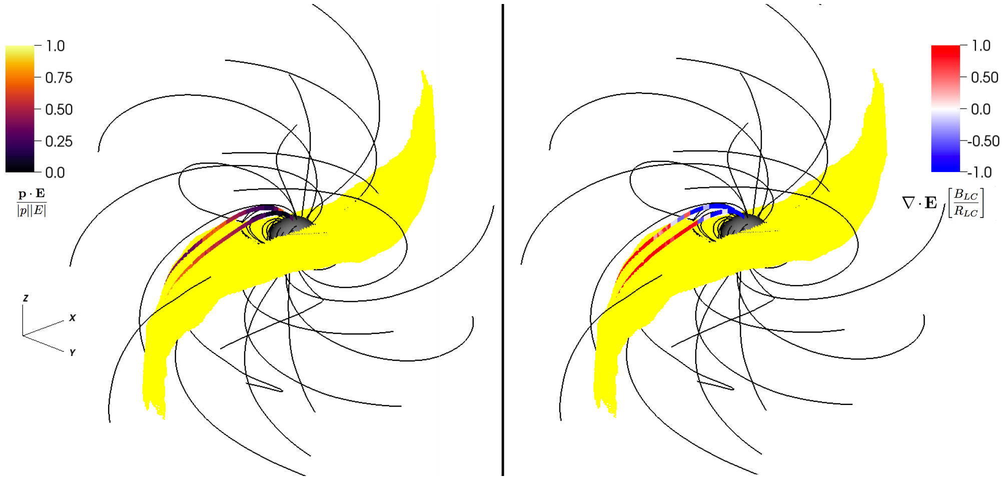
1.0
0.75
0.50
0.25
0.0
$\frac{\mathbf{p}\cdot\mathbf{E}}{|p||E|}$
z
x
Y
1.0
0.50
0.0
-0.50
-1.0
$\nabla\cdot\mathbf{E}\left[\frac{B_{LC}}{R_{LC}}\right]$

Figure 4.23: Positron trajectories flowing from the polar cap into the current sheet. The star with the magnetic field lines is plotted on the background. The yellow opaque surface is the pulsar current sheet. We use an opaque profile instead of a volume rendering profile (as in Figure 4.20) in order to facilitate seeing that the trajectories shown are initially outside the current sheet. We select the current sheet according to Equation 4.13. On the left panel the color on the trajectories is the normalized projection of $\mathbf{p}$ on $\mathbf{E}$, as defined in Equation 4.12. We can see that the value is larger than 0.5 in many parts of the trajectories. On the right panel the color is the divergence of the electric field along the trajectories. We can see that these positrons are transitioning from a negatively charged region, to a positively charged region. The trajectories are in the corotating frame.

particle momentum and the local electric field outside of the current sheet

$$\frac{\mathbf{p}\cdot\mathbf{E}}{pE} \tag{4.12}$$

with $\mathbf{p}$ particle momentum and $\mathbf{E}$ electric field. We use this criterion because in the force-free limit, where particles flow exactly along the magnetic field lines and $\mathbf{E}\perp\mathbf{B}$, $\mathbf{p}$ has components along $\mathbf{B}$ and $\mathbf{E}\times\mathbf{B}$. $\mathbf{E}\times\mathbf{B}$ keeps the particle on the rotating field line. In this limit, the Expression 4.12 is always 0. In Figure 4.23, we see that the expression 4.12 becomes singificantly > 0. This happens in regions where $\mathbf{E}\cdot\mathbf{B} \ll BE$ (where $\mathbf{E}$ is mostly perpendicular to $\mathbf{B}$). In fact, we identify in our PIC simulations the regions where $\mathbf{E}$ has significant components parallel to $\mathbf{B}$ (the yellow opaque volume in Figure 4.23) using

$$\frac{\mathbf{E}\cdot\mathbf{B}}{BE} > 0.15 \tag{4.13}$$

and the field line crossing happens outside of this region. The region defined by the Expression 4.13 traces quite well the regions of reconnecting $\mathbf{B}$.
So far, we showed trajectories for $\alpha = 45°$ case. However, the most well studied case is the aligned rotator and we look for the same trajectories in this case as well and we show them in Figure 4.24. In this case, the electrons circling around the Y-point form a cloud of negative charge that appears as an increase of the negative charge density where the separatrix touches the Y-point. This behavior was first noted in force-free electrodynamics simulations by Timokhin (2006). Therefore, we can safely say that this current structure

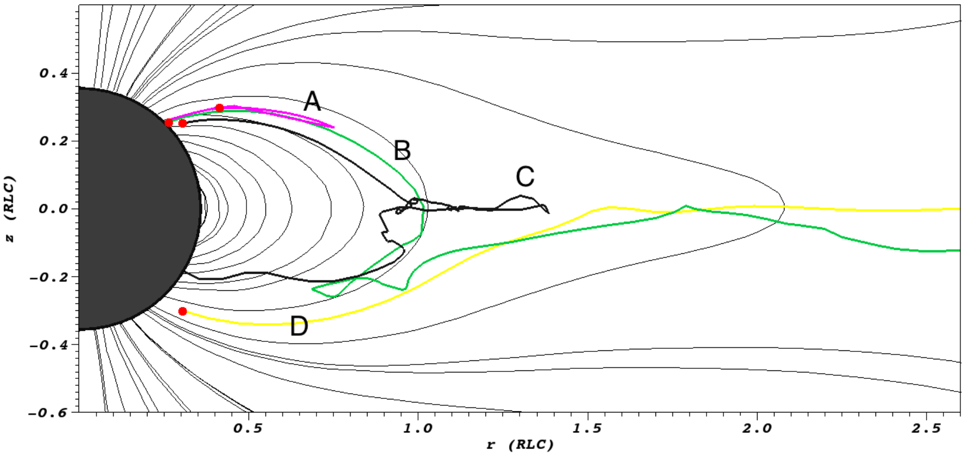

Figure 4.24: The particle trajectories that we presented above, but for the aligned rotator. For clarity, we remove the azimuthal component of their trajectory. The magnitude of the azimuthal components were similar to the trajectories shown in the Figures 4.21, 4.22, 4.23, for the 45° case. The red dot indicates where the particle is injected. All these trajectories have large azimuthal components. The color is a label to help distinguish their intricate trajectories. A) is one of the electrons that starts from the polar cap outflow and get turned back into the separatrix and the returning current. B) is one of the electrons that reaches the Y-point, circles for a while and then flies out following another field line. C) is one of the electrons that reaches the Y-point, circles with huge azimuthal components, and then falls back to the star losing energy. D) is one of the positrons that starts in the polar cap flow, close to the separatrix, crosses field lines and then enters the current sheet.

is sustained by particles crossing field lines mainly inside $1.0R_{\rm LC}$ and for certain inside $2.0R_{\rm LC}$. The main mechanisms are all driven by low electric fields operating on the low energy part of the particle distribution. For the almost perpendicular case, the structure of the current sheet is very different (Kalapotharakos et al. 2012), therefore we decide to reserve this study for the future. Summarizing, we can say that the pulsar magnetosphere structure approaching the force-free solution with particles injected from the surface has these features:

1. Electrons and positrons stream outward together in the polar cap outflow.
2. The electrons that flow back to the star cross field lines, either from the polar cap outflow into the returning current region or after circling around the Y-point.
3. Positrons flow out on the separatrix and get accelerated close to the Y-point into the current sheet. Some positrons enter in the current sheet beyond the Y-point crossing field lines.

4.4 Discussion

In this section we discuss the results we obtained in the context of pulsar magnetosphere theory. First of all, we should note again the limitations of PIC codes in capturing the physical quantities of the pulsar magnetosphere. The open field voltage from Equation 4.6 for a pulsar with $B_0 \sim 10^{12}G$ and $P \sim 0.1s$ would be $\gamma_{max} \sim 10^9$, while we and all the previous studies with PIC simulations (e.g Chen & Beloborodov 2014; Belyaev 2015a; Cerutti et al. 2016; Philippov & Spitkovsky 2017; Kalapotharakos et al. 2017a) use $100 \lesssim \gamma_{max} \lesssim 1000$. This is necessary because we need to resolve ω_p everywhere in our system, as we explained in Chapter 3. Therefore, the particle energy distribution is squeezed into a narrow range and it cannot be simply linearly stretched or shifted to higher energies.

Some of the previously referenced works on PIC pulsar magnetospheres do not show how their results depend on the number of particles injected. We show that many properties and accelerating gaps are connected to the number of particles injected into the magnetosphere, and for high injection rate the magnetosphere reaches the force-free limit for the whole range of inclination angles ($0°, 45°, 85°$). In our case, we are confident in claiming that the current composition we discuss is characteristic of a magnetosphere approaching the force-free limit with particles supplied only close to the surface. In Section 4.3.2, we show that a maximum in the dissipation occurs at an intermediate injection rate between the charge separated solutions and the force-free case (Figure 4.13). Using dissipative models, Kalapotharakos et al. (2012) also found a maximum in dissipation at an intermediate conductivity. We can qualitatively associate the increasing conductivity of these models with the increasing injection rate in our simulations. Gruzinov (2013); Contopoulos (2016) have recently proposed *weak pulsars*, that are magnetosphere configurations that present a larger dissipation than the force-free magnetosphere. These solutions are expected from a particle supply only at the neutron star surface, therefore they should be comparable to our simulations. In opposition for Gruzinov (2013); Contopoulos (2016) *strong pulsars* present little dissipation because pairs are produced in the outer magnetosphere. In our PIC simulations, we identify the solution with the highest dissipation at an intermediate $\mathcal{F}$. For higher $\mathcal{F}$, we get low dissipation solutions even when we inject particles only from the surface. Considering also the previous results, we suggest that a *weak pulsar* magnetosphere originates for these intermediate $\mathcal{F}$. A similar behavior is reported in Cerutti et al. (2015) for an aligned rotator and in

Kalapotharakos et al. (2017a) for simulations that inject particles over the entire computational domain. This is different from the hypothesis of Gruzinov (2013); Contopoulos (2016) that stressed the location of the pair production as decisive parameter. However, these two parameters could be connected, achieving a larger supply of particles when the pairs are produced in the outer magnetosphere. For this reason, it is important to explore the pair production mechanisms in such environments.

From the study of the macroscopic quantities and confirmed by the study of particle trajectories, we find that if particles are injected at the surface there are only a few regions of counter streaming particles. This is important because it was not clear if the currents in the magnetosphere were built of counter streaming species or not. For example, the photon-photon pair production in the current sheet (Lyubarskii 1996) would be inhibited if the electrons and positrons flow out in the same direction, as is the case in our simulation of plasma injection from the surface. Photon-photon pair production in the current sheet is implemented with simple prescriptions in other works (e.g Chen & Beloborodov 2014; Philippov & Spitkovsky 2017). We think that local simulations of this phenomenon in the pulsar current sheet and at the Y-point are needed to address this issue more carefully. However, there are also other mechanisms that could trigger the pair production, like considering other sources of photons, as was discussed for the outer gap (Chiang & Romani 1994). As we mentioned above these answers will help in understanding the difference between *weak* and *strong* pulsars. Another phenomenon impacted by this effect is the hypothesis of generation of the radio emission through the two stream instability (e.g. Usov 2002 for a review). The two stream instability could still occur in the returning current region on the polar cap rim (note that for 45° we found only one of the two branches to have counter streaming particles) and below the pair formation front (e.g. Harding & Muslimov 1998) that is not resolved by this simulation.

When we look at the energetics of the most common particle trajectories we see that the highest energy particles gain most of their energy close to the Y-point and they are outflowing positrons. This hint reinforces the hypothesis of pair production in the outer magnetosphere at the Y-point, but it has to overcome the deficiency of the small scattering angle of the emitted photons. The multiplicity of particles in this region in a real pulsar is another important unknown. Outflowing, energetic particles in the current sheet can produce light curves and spectra (Brambilla et al. 2015; Kalapotharakos et al. 2014, 2017b) that match well with those of the Fermi pulsars (Abdo et al. 2013b). In these works, the particle acceleration is allowed for outflowing particles only after the $R_{\rm LC}$ where the Y-point is located and the particles are injected only at the surface. In Figure 4.14, we see that for magnetospheres that are far from the force-free limit, there can be some acceleration below the Y-point along the separatrix and above the polar cap. This probably indicates that the young γ-ray pulsars we selected for Brambilla et al. (2015) have a magnetosphere close to the force-free limit. However, some millisecond γ-ray pulsars could have emission coming from these lower altitude gaps (Johnson et al. 2014), and their spectra would not suffer any magnetic pair attenuation because of the lower magnetic field. Other energetic particles are the electrons that are circling on the Y-point but they have lower energy than these outgoing positrons. These electrons, and the other particles that we show crossing field lines, naturally gain pitch angles, thus breaking the ideal force-free limit. This makes them natural candidates for the non-thermal synchrotron emission observed at MeV energies and in the hard X-rays (e.g. Kuiper & Hermsen 2015) and it would explain the misalignment with the GeV emission that is observed in certain cases (e.g. Marelli et al. 2014). Obviously the electrons that are circling around the Y-point are more promising candidates, but it is difficult to give final answers when nine orders of magnitude are squeezed into three. It would be extremely interesting to see at which energies this crossing of field lines happens for real pulsars with $\gamma_{max} \sim 10^9$, that would result in high energy particles with $\gamma \sim 10^7$ because of the radiation reaction. However, these kinds of works are helpful because they indicate a direction to follow and new hypotheses to be tested that did not emerge previously. Future missions looking at pulsars in the MeV band (e.g. De Angelis et al. 2017; Moiseev et al. 2015; Hunter et al. 2014) could help unveil the mystery and constrain the models. Looking at the particle trajectories shows also how a current structure close to the one of the force-free configuration can be sustained injecting particles only from the surface of the neutron star. Probably magnetospheres with pair production at the Y-point and/or in the current sheet or in other locations would settle on a different configuration, closer to the simulations where particles are injected everywhere. These scenarios will produce different signatures in the heating of the polar cap in addition to the heating generated by the pair production below the pair formation front (e.g. Harding & Muslimov 2001). These signatures could be potentially observed and discriminated with NICER (Gendreau et al. 2012; Özel et al. 2016).

Conclusions and outlooks

In this thesis I presented my work about modeling the global pulsar magnetosphere with PIC codes. With this work we were able to address previously open questions such as: how are the magnetosphere currents composed? Can a magnetosphere approaching the force-free limit be formed? What are the magnetosphere configurations between the Deutsch solution and the force-free limit? What are the most energetic particles? We also found some surprises on our way, such as the particles that crossed magnetic field lines. This study is less predictive than previous studies that came from our group (Kalapotharakos et al. 2014; Brambilla et al. 2015; Kalapotharakos et al. 2017b,a). Moreover, there are other studies about the pulsar magnetosphere conducted with PIC simulations that were published during my Ph.D. by other groups (Philippov & Spitkovsky 2014; Chen & Beloborodov 2014; Cerutti et al. 2015; Philippov et al. 2015b; Belyaev 2015b,a; Philippov et al. 2015a; Cerutti et al. 2016; Philippov & Spitkovsky 2017). However, this study showed some qualitative features of pulsar magnetospheres that were not previously known. We can summarize the main original contributions of this thesis as:

- We showed that when particles are supplied only at the surface they tend to stream together outward leaving the magnetosphere. This behavior changes if particles are supplied in the outer magnetosphere.
- We showed what happens to particles when the magnetosphere charge changes sign at the Y-point. None of these particle behaviors was previously predicted. These features are for magnetospheres with $\alpha \lesssim 70°$.
  - In the case of particle injection only from the NS surface, the return current is composed of outgoing positrons and returning electrons.
  - The electrons cross field lines into the region of return current.
  - Positrons cross field lines to enter the current sheet beyond the light cylinder.
  - Some electrons are trapped close to the light cylinder because they are scattered by the electric field that accelerates positrons to high energy.
- We investigated intermediate magnetosphere configurations between vacuum and the force-free limit, showing their gap structure and dissipative behavior.

This and the works referenced above are the first attempts to use explicit PIC codes to simulate a global astrophysical system (in opposition to either a local simulation or an MHD simulation). This progress has been made possible by the new computational resources available for scientific computing. Its origin can be traced to Spitkovsky & Arons

(2002) with PIC, and to the seminal work of Krause-Polstorff & Michel (1985) (that used an N-body simulation).

One of the most important things to pursue is a more realistic particle injection mechanisms. When we supplied particles only at the stellar surface, we ignored the specific mechanism of the polar cap pair production that is described in Timokhin & Arons (2013). Moreover, we did not model the photon photon pair production. Some works (Chen & Beloborodov 2014; Philippov et al. 2015b) tried to do this with some important approximations. However, the adequacy of these approximations should be tested with predictions and tests against observations. In order to have a better match with the observations and reproduce the full range of quantities for these systems one should explore implicit PIC codes on the short term (e.g. Markidis et al. 2010) and Vlasov codes on the long term (e.g. Wettervik et al. 2017). Coupling between magnetohydrodynamic simulations and PIC simulations can also be pursued (Daldorff et al. 2014; Tóth et al. 2016). However, there is still room for plenty of experiments with explicit PIC codes and global simulations in high energy astrophysics. Black hole magnetospheres, interactions between two neutron star magnetospheres, magnetars (e.g. Chen & Beloborodov 2017) and maybe pulsar wind nebulae can be explored.

Bibliography

Abdo, A. A., Ackermann, M., Atwood, W. B., et al. 2009, ApJ, 696, 1084

Abdo, A. A., Ajello, M., Allafort, A., et al. 2013a, ApJS, 208, 17

Abdo, A. A., Ajello, M., Allafort, A., et al. 2013b, ApJS, 208, 17

Aharonian, F. A., Akhperjanian, A. G., Aye, K.-M., et al. 2004, Nature, 432, 75

Antoniadis, J., Freire, P. C. C., Wex, N., et al. 2013, Science, 340, 448

Arber, T. D., Bennett, K., Brady, C. S., et al. 2015, Plasma Physics and Controlled Fusion, 57, 113001

Atwood, W. B., Abdo, A. A., Ackermann, M., et al. 2009a, ApJ, 697, 1071

Atwood, W. B., Abdo, A. A., Ackermann, M., et al. 2009b, ApJ, 697, 1071

Baade, W. & Zwicky, F. 1934, Physical Review, 46, 76

Backer, D. C. 1976, ApJ, 209, 895

Bai, X.-N. & Spitkovsky, A. 2010, ApJ, 715, 1282

Bell, S. J. & Hewish, A. 1967, Nature, 213, 1214

Bellan, P. M. 2006, Fundamentals of Plasma Physics (Cambridge University Press)

Beloborodov, A. M. 2008, ApJ, 683, L41

Belyaev, M. A. 2015a, MNRAS, 449, 2759

Belyaev, M. A. 2015b, New A, 36, 37

Berenger, J.-P. 1994, Journal of Computational Physics, 114, 185

Berenger, J.-P. 1996, Journal of Computational Physics, 127, 363

Birdsall, C. K. & Langdon, A. B. 1991, Plasma Physics via Computer Simulation (CRC Press)

Boris, J. P. 1970, Proceeding of Fourth Conference on Numerical Simulations of Plasmas

Boyd, T. J. M. & Sanderson, J. J. 2003, The Physics of Plasmas, 544

Brackbill, J. & Forslund, D. 1982, Journal of Computational Physics, 46, 271

Brambilla. Accessed: 20/10/2017, [Accessed: 20/10/2017]

Brambilla, G., Kalapotharakos, C., Harding, A. K., & Kazanas, D. 2015, ApJ, 804, 84

Brambilla, G., Kalapotharakos, C., Timokhin, A., Harding, A., & Kazanas, D. 2017, ArXiv e-prints

Caraveo, P. A. 2014, ARA&A, 52, 211

Cerutti, B., Philippov, A., Parfrey, K., & Spitkovsky, A. 2015, MNRAS, 448, 606

Cerutti, B., Philippov, A. A., & Spitkovsky, A. 2016, MNRAS, 457, 2401

Chamel, N. & Haensel, P. 2008, Living Reviews in Relativity, 11, 10

Chen, A. Y. & Beloborodov, A. M. 2014, ApJ, 795, L22

Chen, A. Y. & Beloborodov, A. M. 2017, ApJ, 844, 133

Cheng, A., Ruderman, M., & Sutherland, P. 1976, ApJ, 203, 209

Chiang, J. & Romani, R. W. 1994, ApJ, 436, 754

Childs, H., Brugger, E., Whitlock, B. J., et al. 2012, CRC Computational Science Series, Vol. 1, VisIt: An End-User Tool for Visualization and Analyzing Very Large Data, 1st edn., ed. E. W. Bethel, H. Childs, & C. Hansen (Boca Raton: Taylor and Francis), 520

Contopoulos, I. 2016, MNRAS, 463, L94

Contopoulos, I., Kazanas, D., & Fendt, C. 1999, ApJ, 511, 351

Cowling. 1957, Nucl. Phys. A, 3, 624

Daldorff, L. K. S., Tóth, G., Gombosi, T. I., et al. 2014, Journal of Computational Physics, 268, 236

Daugherty, J. K. & Harding, A. K. 1996, ApJ, 458, 278

De Angelis, A., Tatischeff, V., Tavani, M., et al. 2017, Experimental Astronomy, 44, 25

de Jager, O. C., Harding, A. K., Michelson, P. F., et al. 1996, ApJ, 457, 253

Demorest, P. B., Pennucci, T., Ransom, S. M., Roberts, M. S. E., & Hessels, J. W. T. 2010, Nature, 467, 1081

Deutsch, A. J. 1955, Annales d'Astrophysique, 18, 1

Dyks, J. & Rudak, B. 2003, ApJ, 598, 1201

Everett, J. E. & Weisberg, J. M. 2001, ApJ, 553, 341

Ferraro, V. C. A. 1937, MNRAS, 97, 458

Gendreau, K. C., Arzoumanian, Z., & Okajima, T. 2012, in Proc. SPIE, Vol. 8443, Space Telescopes and Instrumentation 2012: Ultraviolet to Gamma Ray, 844313

Gold, T. 1968, Nature, 218, 731

Goldreich, P. & Julian, W. H. 1969, ApJ, 157, 869

Gonthier, P. L., Van Guilder, R., & Harding, A. K. 2004, ApJ, 604, 775

Gruzinov, A. 2005, Physical Review Letters, 94, 021101

Gruzinov, A. 2006, ApJ, 647, L119

Gruzinov, A. 2008, ArXiv e-prints

Gruzinov, A. 2013, ArXiv e-prints

Harding, A. K. 2005, in 22nd Texas Symposium on Relativistic Astrophysics, ed. P. Chen, E. Bloom, G. Madejski, & V. Patrosian, 149–158

Harding, A. K. 2013, Frontiers of Physics, 8, 679

Harding, A. K. & Lai, D. 2006, Reports on Progress in Physics, 69, 2631

Harding, A. K. & Muslimov, A. G. 1998, ApJ, 508, 328

Harding, A. K. & Muslimov, A. G. 2001, ApJ, 556, 987

Harding, A. K. & Muslimov, A. G. 2002, ApJ, 568, 862

Hewish, A., Bell, S. J., Pilkington, J. D. H., Scott, P. F., & Collins, R. A. 1968, Nature, 217, 709

Hockney, R. W. & Eastwood, J. W. 1981, Computer Simulation Using Particles (McGraw-Hill)

https://wci.llnl.gov/simulation/computer codes/silo. Accessed: 20/10/2017, [Accessed: 20/10/2017]

https://www.mpich.org/static/docs/v3.1/www3/. Accessed: 10/10/2017, [Accessed: 10/10/2017]

https://www.vtk.org/. Accessed: 20/10/2017, [Accessed: 20/10/2017]

Hulse, R. A. & Taylor, J. H. 1975, ApJ, 195, L51

Hunter, S. D., Bloser, P. F., Depaola, G. O., et al. 2014, Astroparticle Physics, 59, 18

Jackson, J. D. 1998a, Classical Electrodynamics, 3rd Edition (Wiley-VCH), 832

Jackson, J. D. 1998b, Classical Electrodynamics, 3rd Edition

Johnson, S. G. checked on: 2017-05-01, Yee lattice

Johnson, T. J., Venter, C., Harding, A. K., et al. 2014, ApJS, 213, 6

Kagan, D., Sironi, L., Cerutti, B., & Giannios, D. 2015, Space Sci. Rev., 191, 545

Kalapotharakos, C., Brambilla, G., Timokhin, A., Harding, A. K., & Kazanas, D. 2017a, ArXiv e-prints

Kalapotharakos, C., Harding, A. K., & Kazanas, D. 2014, ApJ, 793, 97

Kalapotharakos, C., Harding, A. K., Kazanas, D., & Brambilla, G. 2017b, ApJ, 842, 80

Kalapotharakos, C., Kazanas, D., Harding, A., & Contopoulos, I. 2012, ApJ, 749, 2

Kargaltsev, O. & Pavlov, G. G. 2008, in American Institute of Physics Conference Series, Vol. 983, 40 Years of Pulsars: Millisecond Pulsars, Magnetars and More, ed. C. Bassa, Z. Wang, A. Cumming, & V. M. Kaspi, 171–185

Kaspi, V. M. & Beloborodov, A. M. 2017, ARA&A, 55, 261

Kennel, C. F. & Coroniti, F. V. 1984, ApJ, 283, 694

Kerr, M. 2011, ApJ, 732, 38

Krause-Polstorff, J. & Michel, F. C. 1985, MNRAS, 213, 43P

Kuiper, L. & Hermsen, W. 2015, MNRAS, 449, 3827

Landau, L. D. 1932, Phys. Zs. Sowjet., vol.1, p.285, 1932 (English and German), 1, 285

Landau, L. D. & Lifshitz, E. M. 1980, The Classical Theory of Fields, 4th edn. (Butterworth-Heinemann)

Lapenta, G. checked on: 2017-03-03, The Particle In Cell Method

Li, J., Spitkovsky, A., & Tchekhovskoy, A. 2012, ApJ, 746, 60

Lommen, A. N. 2012, in Journal of Physics Conference Series, Vol. 363, Journal of Physics Conference Series, 012029

Lyubarskii, Y. E. 1990, Soviet Astronomy Letters, 16, 16

Lyubarskii, Y. E. 1996, A&A, 311, 172

Lyutikov, M., Otte, N., & McCann, A. 2012, ApJ, 754, 33

Mahmoodifar, S. & Strohmayer, T. 2017, ApJ, 840, 94

Marelli, M., Harding, A., Pizzocaro, D., et al. 2014, ApJ, 795, 168

Markidis, S., Lapenta, G., & Rizwan-uddin. 2010, Mathematics and Computers in Simulation, 80, 1509 , multiscale modeling of moving interfaces in materials

Michel, F. C. 1982, Reviews of Modern Physics, 54, 1

Michel, F. C. 1991a, Theory of neutron star magnetospheres

Michel, F. C. 1991b, Theory of neutron star magnetospheres

Michel, F. C. & Li, H. 1999, Phys. Rep., 318, 227

Miller, M. C. & Lamb, F. K. 2015, ApJ, 808, 31

Miller, M. C. & Lamb, F. K. 2017, in AAS/High Energy Astrophysics Division, Vol. 16, AAS/High Energy Astrophysics Division, 104.03

Moiseev, A. A., Ajello, M., Buckley, J. H., et al. 2015, ArXiv e-prints

Özel, F., Psaltis, D., Güver, T., et al. 2016, ApJ, 820, 28

Pacini, F. 1967, Nature, 216, 567

Pacini, F. 1968, Nature, 219, 145

Papitto, A., Ferrigno, C., Bozzo, E., et al. 2013, Nature, 501, 517

Pétri, J. 2009, A&A, 503, 1

Philippov, A. A., Cerutti, B., Tchekhovskoy, A., & Spitkovsky, A. 2015a, ApJ, 815, L19

Philippov, A. A. & Spitkovsky, A. 2014, ApJ, 785, L33

Philippov, A. A. & Spitkovsky, A. 2017, ArXiv e-prints

Philippov, A. A., Spitkovsky, A., & Cerutti, B. 2015b, ApJ, 801, L19

Pittori, C. 2013, Nuclear Physics B Proceedings Supplements, 239, 104

Pizzochero, P. M., Antonelli, M., Haskell, B., & Seveso, S. 2017, Nature Astronomy, 1, 0134

Porth, O., Buehler, R., Olmi, B., et al. 2017, Space Sci. Rev., 207, 137

Radhakrishnan, V. & Cooke, D. J. 1969, Astrophys. Lett., 3, 225

Rankin, J. M. 1983, ApJ, 274, 333

Rankin, J. M. 1990, ApJ, 352, 247

Rees, M. J. & Gunn, J. E. 1974, MNRAS, 167, 1

Reisenegger, A. 2009, A&A, 499, 557

Ruderman, M. A. & Sutherland, P. G. 1975, ApJ, 196, 51

Rybicki, G. B. & Lightman, A. P. 1986, Radiative Processes in Astrophysics, 400

Shao, L., Stairs, I., Antoniadis, J., et al. 2015, Advancing Astrophysics with the Square Kilometre Array (AASKA14), 42

Shapiro, S. L. & Teukolsky, S. A. 1983, Black holes, white dwarfs, and neutron stars: The physics of compact objects

Showstack, R. 2013, Nick Sagan Reflects on Voyager 1 and the Golden Record, Vol. 94, 351–351

Somov, B. V., ed. 2012, Astrophysics and Space Science Library, Vol. 391, Plasma Astrophysics, Part I

Spitkovsky, A. 2006, ApJ, 648, L51

Spitkovsky, A. & Arons, J. 2002, in Astronomical Society of the Pacific Conference Series, Vol. 271, Neutron Stars in Supernova Remnants, ed. P. O. Slane & B. M. Gaensler, 81

Strohmayer, T. E., Zhang, W., Swank, J. H., et al. 1996, ApJ, 469, L9

Sturrock, P. A. 1971, ApJ, 164, 529

Taflove, A. & Hagness, S. C. 2005, Computational electrodynamics: the finite-difference time-domain method, 3rd edn. (Norwood: Artech House)

Tamburini, M., Pegoraro, F., Di Piazza, A., Keitel, C. H., & Macchi, A. 2010, New Journal of Physics, 12, 123005

Tchekhovskoy, A., Philippov, A., & Spitkovsky, A. 2016, MNRAS, 457, 3384

Thompson, C. & Duncan, R. C. 1995, MNRAS, 275, 255

Thompson, D. J. 2008, Reports on Progress in Physics, 71, 116901

Timokhin, A. N. 2006, MNRAS, 368, 1055

Timokhin, A. N. & Arons, J. 2013, MNRAS, 429, 20

Timokhin, A. N. & Harding, A. K. 2015, ApJ, 810, 144

Tóth, G., Jia, X., Markidis, S., et al. 2016, Journal of Geophysical Research (Space Physics), 121, 1273

Turolla, R. 2009, in Astrophysics and Space Science Library, Vol. 357, Astrophysics and Space Science Library, ed. W. Becker, 141

Turolla, R., Zane, S., & Watts, A. L. 2015, Reports on Progress in Physics, 78, 116901

`http://apod.nasa.gov/apod/archivepix.html`. Accessed: 08/10/2017, [Accessed: 08/10/2017]

`http://chandra.harvard.edu/`. Accessed: 08/10/2017, [Accessed: 08/10/2017]

`http://news.psu.edu/`. Accessed: 20/10/2017, [Accessed: 20/10/2017]

`https://confluence.slac.stanford.edu/display/GLAMCOG/Public+`

`List+of+LAT-Detected+Gamma-Ray+Pulsars`. Accessed: 10/10/2017, *Public List of LAT-Detected Gamma-Ray Pulsars*, [Accessed: 10/10/2017]

`http://svs.gsfc.nasa.gov/`. Accessed: 08/10/2017, [Accessed: 08/10/2017]

Usov, V. V. 2002, in Neutron Stars, Pulsars, and Supernova Remnants, ed. W. Becker, H. Lesch, & J. Trümper, 240

Vay, J.-L. 2008, Physics of Plasmas, 15, 056701

Vay, J.-L. & Godfrey, B. B. 2014, Comptes Rendus Mecanique, 342, 610

Villasenor, J. & Buneman, O. 1992, Computer Physics Communications, 69, 306

Vranic, M., Martins, J. L., Fonseca, R. A., & Silva, L. O. 2016, Computer Physics Communications, 204, 141

Wettervik, B. S., DuBois, T. C., Siminos, E., & Fülöp, T. 2017, European Physical Journal D, 71, 157

Wheeler, J. A. 1966, ARA&A, 4, 393

Yadigaroglu, I.-A. G. 1997, PhD thesis, STANFORD UNIVERSITY

Yakovlev, D. G., Haensel, P., Baym, G., & Pethick, C. 2013, Physics Uspekhi, 56, 289

Yee, K. 1966, IEEE Transactions on Antennas and Propagation, 14, 302

Zane, S., Rea, N., Turolla, R., & Nobili, L. 2009, MNRAS, 398, 1403

List of Publications

As of November 3^{rd} *2017*

Publications under review

- Brambilla G., Kalapotharakos C., Timokhin A. N., Harding A. K., Kazanas D. (2017) Electron Positron Pair Flow and Current Composition in the Global Pulsar Magnetosphere, *submitted - arXiv:1710.03536*, 16 pages.
- Kalapotharakos C., Brambilla G., Timokhin A. N., Harding A. K., Kazanas D. (2017) 3D Kinetic Pulsar Magnetosphere Models: Exploring Self Consistency, *submitted - arXiv:1710.03170*, 23 pages.